MSc thesis in Sustainable Energy Technology

SIMULATION AND VALIDATION OF WAKE DEFLECTION IN VERTICAL-AXIS WIND TURBINES

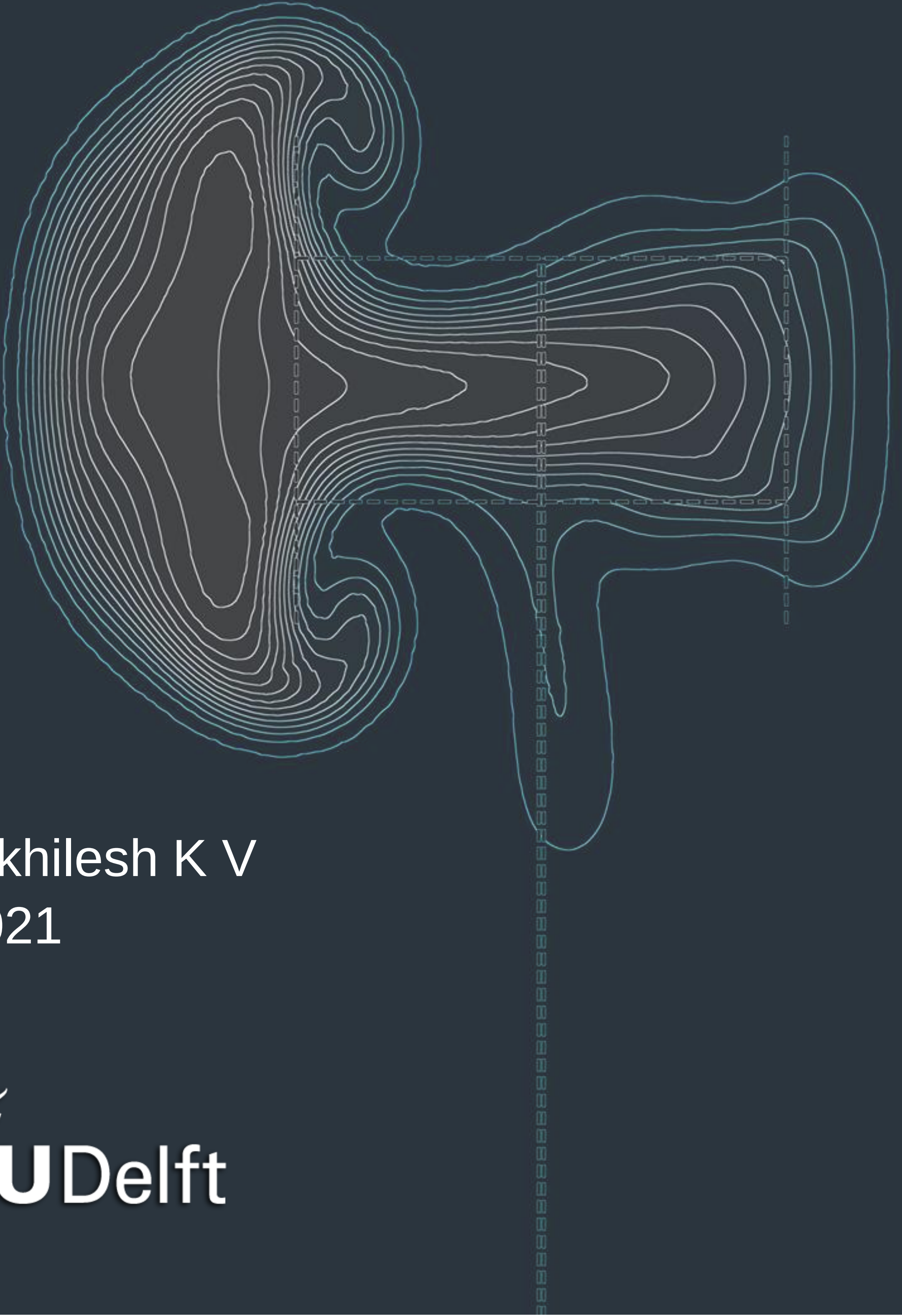

Nikhilesh K V

2021

SIMULATION AND VALIDATION OF WAKE DEFLECTION IN VERTICAL-AXIS WIND TURBINES

A thesis submitted to the Delft University of Technology in partial fulfillment
of the requirements for the degree of

Master of Science in Sustainable Energy Technology

by

Kodur Venkatesh Nikhilesh

5037964

November 2021

Kodur Venkatesh Nikhilesh: *Simulation and validation of wake deflection in Vertical-Axis Wind turbines* (2021)

ISBN 999–99–9999–999–9

The work in this thesis was made in:

Wind Energy Group
Sustainable Energy Technology
Faculty of Electrical Engineering, Mathematics and Computer Science
Delft University of Technology

Supervisors:	Dr. ir. Carlos Simaô Ferriera Dr. Delphine De Tavernier Mr. Ming Huang
Co-readers:	Dr. Delphine De Tavernier Mr. Ming Huang

ABSTRACT

The wake of a wind turbine is of paramount importance while designing a wind farm layout. While extensive research has been conducted in the past on the wakes of horizontal-axis wind turbines (HAWTs), the wake of a vertical-axis wind turbine (VAWT) is not well understood. There is a dearth of literature on wake deflection using VAWTs. Although several modelling techniques exist to model the wake of a VAWT, very few of them are validated with experimental data. In this study, the existing modelling techniques used to model VAWTs and their wakes are reviewed. Subsequently, computational fluid dynamics (CFD) simulations are carried out using Open-source Field Operation And Manipulation (OpenFOAM), an open-source CFD tool. The flow is modelled using unsteady Reynolds averaged Navier-Stokes (URANS) equations with the standard $k - \epsilon$ (KE) turbulence model. The rotor is modelled using the actuator line model (ALM) with corrections for flow curvature, dynamic stall, added mass and tip effects. The Beddoes-Leishman (B-L) dynamic stall models are implemented using the turbinesFoam library (Bachant et al., 2019). The simulation parameters (*i.e.* mesh topology, time steps and ensemble averaging period) are set up after an extensive study of the impact of spatial and temporal discretization on the accuracy of the results. The field values of the flow are averaged over 15 rotations of the turbine after convergence. To evaluate the effect of the turbulence and dynamic stall models on the wake, a sensitivity study is carried out. In addition to this, a study is carried out to evaluate the impact of three different dynamic stall models (*i.e.* standard B-L, B-L-3*G* and B-L-Sheng-Galbraith-Coton (SGC)) on the wake and blade loading. The results of this sensitivity study show that:

- The standard $k - \epsilon$ model (KE) is highly sensitive to inlet turbulence intensity and turbulent dissipation values. The wake recovery is significantly affected by turbulence and hence the turbulence model parameters.
- The B-L dynamic stall models are sensitive to the empirical constants and the parameters used in this study predict an early onset of dynamic stall compared to experiments.
- The instantaneous blade loading and hence, the dynamic stall, have a significant impact on the asymmetry, structure and recovery of a VAWT wake.

Wake and wake deflection is studied with three cases of blade pitch angles ($\beta = 0°, +10° \& -10°$). The obtained wake velocity field data from the simulations for downstream distances of $1D$ to $10D$ is validated with the experimental data obtained from experiments by Huang et al. (2020), under the same conditions. The conclusions from this validation include:

- The simulation results generally compare well with the experiments, with the largest absolute mean deviation of 10.7% for the case of $\beta = +10°$ at $x = 1D$, in the mid-span wake velocities, among the three cases.
- Larger blade loading creates larger near-wake velocity deficits but also show higher recovery rates.
- The prediction of the azimuthal location of the largest blade loading and the duration of the blade in stall, have a significant impact on the wake velocity deficits and hence, the wake asymmetry, structure, recovery and deflection.

ACKNOWLEDGEMENTS

DON'T PANIC, *in large, friendly letters*, written on the cover of *Hitchhiker's Guide to the Galaxy* - has been my mantra throughout this journey. While the journey has been thoroughly enjoyable and exciting, it has had its crests and troughs. This study introduced me to the complex aerodynamics of a vertical-axis wind turbine and has greatly enriched my understanding of the underlying physics of its operation and its wakes. It has been a wonderful learning experience and allowed me to explore a wide range of topics from tensor calculus to turbulence. This study has further given me a glimpse of how research is carried out and left me longing for more.

This project would have been difficult without support from several others, whom I would like to thank here.

In Indian tradition, the utmost priority is given to a *guru* - a teacher. In my case, the role of a *guru* was taken over by Delphine and Ming. The empathy they extended during the lows of my journey stands out. Our discussions have not only been instrumental in shaping my understanding of the concepts, but also provided novel ways to approach rather difficult questions. I am extremely thankful for their guidance and support.

Further, I would like to thank Carlos for providing me with this incredible opportunity to work on this project and for the invaluable counsel in managing my expectations and time.

Surviving the cold, dark winters and the isolation that came with a worldwide pandemic, would have been extremely difficult without a friend. I would like to thank Swami, Christal, and her family for the warmth they extended to me during my stay in the box.

Finally, this sojourn would not have been possible without the constant support and encouragement of my parents and my extended family, to whom I am ever so grateful.

Nikhilesh
November 2021

CONTENTS

LIST OF FIGURES

LIST OF TABLES

ACRONYMS

1D	1 dimensional	20
2D	2 dimensional	6
3D	3 dimensional	37
AC	actuator cylinder	19
AD	actuator disk	19
ALM	actuator line model	37
AOA	angle of attack	39
BEM	blade-element momentum	5
B-L	Beddoes-Leishman	39
CACTUS	the Code for Axial and Cross-flow TUrbine Simulation	27
CFL	Courant-Fredrichs-Lewy	43
CFD	computational fluid dynamics	38
DES	detached eddy simulation	28
DMST	double multiple stream tube	22
DNS	direct numerical simulation	28
DS	dynamic stall	62
DST	double stream tube	22
HAWC2	Horizontal Axis Wind turbine simulation Code 2nd generation	25
HAWT	horizontal-axis wind turbine	1
KE	$k - \epsilon$ model	40
KW	$k - \omega$ model	31
SST KW	shear stress transport $k - \omega$ model	30
LES	large eddy simulation	28
MST	multiple stream tube	22
N-S	Navier-Stokes	37
OJF	open jet facility	47
OpenFOAM	Open-source Field Operation And Manipulation	37
PIV	Particle Image Velocimetry	47
RANS	Reynolds averaged Navier-Stokes	64
RKE	realizable $k - \epsilon$ model	30
RNG	renormalization group theory $k - \epsilon$ model	30
SA	Spalart-Allmaras model	30
SGC	Sheng-Galbraith-Coton	39
SGS	sub-grid scale	31
SST	single stream tube	22
TSR	tip speed ratio	39
TSST	transition shear stress transport $k - \omega$ model	30
U2DiVA	the Unsteady Two-Dimensional Vorticity Aerodynamics	27
URANS	unsteady Reynolds averaged Navier-Stokes	37
VAWT	vertical-axis wind turbine	37

LIST OF SYMBOLS

α	Angle of attack
β	Blade pitch angle
β_s	Strut pitch angle
δ_{ij}	Kronecker delta
ϵ	Turbulent viscous dissipation
$\frac{D}{Dt}$	Material derivative
Γ	Circulation
γ	Intermittency
λ	Tip speed ratio
μ	Dynamic viscosity
ν	Kinematic viscosity
ν_T	Eddy viscosity
Ω	Magnitude of angular velocity of the rotor
ω	Specific turbulent kinetic energy dissipation rate
$\overline{X}$	Time averaged quantity X
ψ	Inflow angle
ρ	Air density
τ_{ij}	Stress tensor
$\vec{f}$	Force per unit volume
ζ	Non-dimensionalised span
a	Induction factor at the upwind actuator disk
a'	Induction factor at the downwind actuator disk
B	Number of blades
c	Chord length
C_d	Drag coefficient of the blade
c_d	Drag coefficient per unit span length
C_l	Lift coefficient of the blade
c_l	Lift coefficient per unit span length
C_p	Instantaneous power coefficient of the turbine
C_T	Instantaneous torque coefficient of the turbine
C_t	Instantaneous thrust coefficient of the turbine

C_n	Instantaneous blade normal force coefficient
$C_{p,avgn}$	Power coefficient averaged over n rotations of the rotor
$C_{p,max}$	Maximum power coefficient
$C_{T,avgn}$	Torque coefficient averaged over n rotations of the rotor
$C_{t,avgn}$	Thrust coefficient averaged over n rotations of the rotor
$C_{t,blade}$	Instantaneous thrust coefficient of the blade
C_{ta}	Instantaneous tangential force coefficient
Co	Courant number
D	Rotor diameter
D_{2D}	Drag force per unit span length
f_{bi}	Body forces per unit volume on the fluid
f_i	Force per unit volume exerted by the blades on the flow
Fr	Froude number
G	Sub-grid scale filtering kernel
g	Acceleration due to gravity
H	Height of the rotor and blade span
i, j, k	Indices representing the co-ordinate axes $(1, 2, 3)$
k	Turbulent kinetic energy
k_r	Reduced frequency
L_{2D}	Lift force per unit span length
M	Mach number
p	Static pressure
$p_{,i}$	Pressure gradient
P_{2D}	Instantaneous power generated per unit span length
q	Dynamic pressure
q_∞	Freestream dynamic pressure
R	Radius of the rotor
R_n	Normal component of the resultant force on the blade
R_t	Tangential component of the resultant force on the blade
Re	Reynolds number
$Re_{\theta t}$	Momentum thickness Reynolds number
S_{ij}	Strain rate tensor
St	Strouhal number
T	Time period
T_{2D}	Instantaneous thrust force per unit span length

u'_i	Fluctuating velocity components
u_i	Velocity components
u_x	Velocity perturbation component along X-axis
u_y	Velocity perturbation component along Y-axis
V_x	Velocity component along X-axis
V_y	Velocity component along Y-axis
V_∞	Undisturbed/freestream wind speed
V_{ind}	Magnitude of induced velocity at the rotor
V_n	Magnitude of relative velocity normal to blade path
V_{rel}	Magnitude of relative velocity of air with respect to moving blade
V_r	Blade speed
V_t	Magnitude of relative velocity tangential to blade path
x_i	Spatial co-ordinates

1 INTRODUCTION

The cascading effects of climate change can no longer be ignored. There is an urgent need to reduce our carbon emissions to tackle climate change and wind energy has a promising role in this fight. As the world accelerates to cleaner energy sources, IRENA (2019) predicts wind energy alone to meet 35% of the global electricity demand, with a total nominal power generation capacity of 6000 GW peak by 2050. A wind turbine extracts kinetic energy from the wind to generate electricity. An array of such wind turbines constitute a wind farm. The global cumulative onshore wind power generation capacity is expected to grow nine-fold, while the global cumulative offshore capacity is expected to expand to ten times its 2019 value by 2050.

The flow of air around the blades of the wind turbine generates lift and drag forces. A resultant of these forces, provide the necessary torque to turn a generator that produces electricity. Based on the alignment of the axis of rotation, wind turbines fall into two categories; horizontal-axis wind turbines (HAWTs), where the axis is aligned against the wind direction, and vertical-axis wind turbines (VAWTs), where the axis is perpendicular to the wind direction.

The extraction of kinetic energy from the wind creates a deficit in wind velocities and an increase in the turbulence of the wind downstream, referred to as the wake of the wind turbine. This wake, generated by the upstream wind turbines in a wind farm, significantly decreases the power output of the wind turbines downstream. To reduce this effect, the wind turbines in a wind farm are placed a distance from each other leading to the consumption of large swaths of area. Despite this distance, the wind velocities do not fully recover downstream. Wake deflection or wake steering is a method by which the wake of a wind turbine can be redirected to avoid the downstream turbines, thereby improving their power output. It has been seen that employing wake deflection in a HAWT wind farm can improve its power output by up to 13% (Howland et al., 2019).

1.1 MOTIVATION AND PROBLEM STATEMENT

The expression for the power generated by the wind turbine is given by Equation 1.1, where the electrical power output is given by P, the air density by ρ, the rotor swept area by A, and the undisturbed wind speed by V_∞. The term C_p is the power coefficient, that indicates the fraction of the kinetic energy of the wind that is converted into rotational energy of the turbine, thereby indicating its aerodynamic efficiency. This rotational energy of the rotor is then converted to electricity by the generator, with the torque transmitted through a gearbox and a shaft. While the efficiencies of all the energy conversions impact the power generation in a wind turbine, the aerodynamic efficiency of the rotor is the focus of this study. It has been shown that the maximum value of this power coefficient cannot exceed 59.3%, which is known as the Lanchester–Betz–Joukowsky limit (van Kuik, 2007).

$$P = \frac{1}{2} C_p \rho A V_\infty^3 \tag{1.1}$$

From Equation 1.1, it can be clearly seen that the mechanical power output of the wind turbine rotor has a cubic dependence on the inflow wind speed. Since the extraction of kinetic energy from the wind reduces the wind speed downstream, the wind speed recovery in a wind farm plays a significant role in its power output. Deflecting the wake can improve the inflow wind speeds for the downstream turbines improving the farm power outputs.

A large part of the research in the past has been dedicated to the study of wake deflection for HAWTs farms, whereas the literature on wake deflection for VAWT is limited in comparison. Hence there is a need to better understand the parameters affecting the wake deflection and the nature of the deflected wake in VAWTs. The availability of computational fluid dynamics (CFD) tools and high-performance computation clusters provide a good platform to numerically solve the Navier-Stokes equations and obtain high-fidelity solutions that describe the wake. However, these solutions need to be compared with experiments to ascertain their validity and evaluate their accuracy, highlighting the need for the current study.

1.2 OBJECTIVE AND RESEARCH QUESTIONS

The main objective of this thesis is to simulate wake deflection using a down-scaled, isolated VAWT using Open-source Field Operation And Manipulation (OpenFOAM), an open-source CFD tool, and to validate the simulation using experimental data. The experiment is conducted in open jet facility (OJF), at TU Delft by Huang et al..

The research questions being probed in this thesis are as follows:

1. How can wake deflection be simulated using OpenFOAM and what are the different modelling techniques available in the literature?
2. What are the important simulation parameters affecting the simulation of wake deflection in an isolated, down-scaled VAWTs in OpenFOAM?
3. What are the correction models required for the simulations and how do they affect the accuracy of the simulation results?
4. What is the effect of blade pitching on the turbine performance (blade loading, thrust and power coefficients) and the wake velocity field?
5. How do the simulation results compare with the experiments?
6. How can the accuracy of the simulation results be improved?

1.3 REPORT STRUCTURE

Chapter 1 of the report presents a brief introduction, the motivation, the problem statement and the research questions addressed in this study. Chapter 2 provides a detailed introduction to VAWTs, the underlying aerodynamics involved in the energy conversion process, the available literature on different modelling techniques used to model VAWTs and their wakes and a comparison of the models' performance. Chapter 3 discusses the approach to implementation of the actuator line model (ALM) in OpenFOAM, the turbine geometry, the numerical setup and the simulation parameters. Chapter 4 presents a discussion of the results obtained for the baseline simulation and presents the parameters for validation of the simulation. Chapter 5 presents the validation of the different simulation cases with the available experimental data. Chapter 6 provides a brief summary of the study and the conclusions drawn therein.

2 LITERATURE REVIEW

This chapter provides a discussion on the reviewed literature to address the research questions mentioned in Section 1.2. At the outset, a brief introduction to vertical-axis wind turbines (VAWTs) is provided in Section 2.1. The subsequent Section 2.2, provides a detailed discussion on the basic aerodynamic concepts involved in a VAWT operation. Section 2.3 provides a discussion of the various unsteady aerodynamic phenomena dominating the operation of VAWTs and an approach to their modelling. The wake aerodynamics and wake deflection are discussed in Section 2.4. Finally, the performance of the different rotor and wake modelling techniques are compared in Section 2.7.

2.1 INTRODUCTION TO VAWTS

A VAWT, also sometimes referred to as a cross-flow turbine, has the rotational axis of its rotor aligned perpendicular to the direction of the wind. While the earliest use of a VAWT in history dates back to 200 BC (Kaldellis and Zafirakis, 2011), their growth has been stunted mainly due to their complex aerodynamics and a perceived lack of advantages over HAWTs, as elaborated in Section 2.1.2. Several VAWT installations over the past years have been plagued by fatigue issues (Sutherland et al., 2012) due to the occurrence of deep dynamic stall (Keisar et al., 2020) and an inability to predict blade loads accurately due to dynamic effects. However, the recent years have seen a spur of research interest in VAWTs, owing to a better performance of VAWTs in wind farm settings (Dabiri, 2010), suitability to turbulent urban environments (Kumar et al., 2018) and offshore floating wind farm applications (Sutherland et al., 2012).

2.1.1 Types of VAWTs

A VAWT can be classified into two types based on the dominant driving force generating the torque; Savonius type, which is driven mainly by drag forces and Darrieus type, which is lift driven. The Savonius rotor (refer Figure 2.1), named after its inventor, has convex shaped blades that generate unbalanced drag forces in the windward and leeward sides of the rotor, resulting in its rotation. These drag driven turbines have lower maximum theoretical power coefficients ($C_{p,max} = 0.3$) (Hau, 2006) compared to their lift driven counterparts. The lift driven rotors can have maximum theoretical power coefficients that are marginally higher than the Lanchester–Betz–Joukowsky limit (Thönnißen et al., 2016). However, the drag driven turbines can self start at very low wind velocities popularizing their usage in cup anemometers.

The lift driven turbine, with the ϕ shaped rotor shown in Figure 2.1, was first introduced by Darrieus in 1931. Lift driven VAWTs can be further classified based on the surface swept by the blade as it rotates about the axis. Some of the commonly found swept surfaces are conical (V-shaped blades), ellipsoidal (ϕ-rotor) and cylindrical (H-rotor). This study, however, is focused only on the straight bladed H-rotor VAWT. The main component of a VAWT rotor that generates the aerodynamic forces are the blades. The component of the resultant force on the blades in their direction of motion provides the resulting torque to turn the rotor. The struts provide

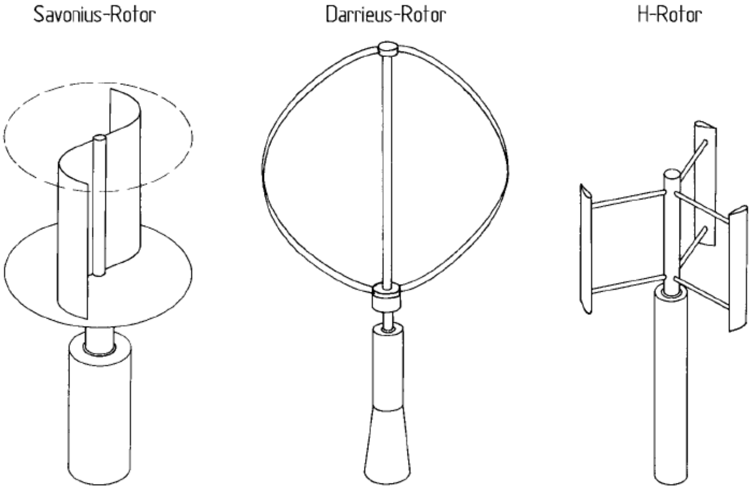

Figure 2.1: Commonly used rotor designs of VAWTs (Hau, 2006)

the structural support to hold the blades and transmit the torque generated by the blades, to the rotor shaft. The tower provides the vertical force required to balance the weight of the rotor and houses the rotor shaft that transmits the torque to the generator.

2.1.2 Advantages and disadvantages

The historical advantage of a VAWT has been that it can operate irrespective of the wind direction, unlike a HAWT which has to constantly align with the wind direction. VAWTs are observed to perform better under turbulent wind conditions (Carbó Molina et al., 2018). They operate at low tip speed ratios (TSRs) resulting in lower noise. Studies by Mertens et al. (2003) has shown that VAWTs, under a skewed flow perform better, making them ideal to be placed on the top of tall buildings. These factors make VAWTs better suited for urban environments as compared to HAWTs. Further, the low TSR of operation results in smaller pressure differences, causing less impact on bats that are severely affected by barotrauma (Baerwald et al., 2008). The height of a VAWT is much smaller causing less impact to migratory birds.

While the overall efficiency of an isolated VAWT is lower than that of an isolated HAWT with the same swept area (Fadil et al., 2017), recent studies by Hezaveh et al. (2018) show that the performance of adjacent, close-spaced, counter-rotating VAWTs is much better than that of an isolated VAWT, when they are aligned with the optimal wind direction. The wake recovery for a VAWT is also much faster than that for a HAWT (Kinzel et al., 2012), allowing close placement of VAWTs in a wind farm setting. Consequently a VAWT farm can have a significantly higher power density compared to a HAWT farm (Dabiri, 2010). The gearbox and generator of a VAWT are located at the ground level allowing greater ease of access and maintenance. This has found its advantage particularly in off-shore and floating applications, where costs of installation and maintenance significantly increase with height of placement of the heavier components (Sutherland et al., 2012; Griffith et al., 2016).

However, VAWTs do have several disadvantages. Although the working principles of a VAWT is similar to that of HAWT, the unsteady effects in VAWT make it difficult to predict the blade loading. The blade-wake interactions and a large variation in the angle of attack (AOA) with the azimuthal angle means that dynamic stall is a common occurrence. The operation of VAWTs at low TSR further increases the severity of the dynamic stall (Laneville and Vittecoq, 1986) causing increased magnitudes dynamic loading on the blades, resulting in higher blade fatigue. The constantly varying forces on the blades results in large variations in the torque, called the torque ripple, causing damage to the generator. This however, can be addressed by increasing the number of blades or by installing helical blades (Scheurich et al., 2012) or by employing pitch control (Erfort et al., 2020). Another historic issue with lift driven VAWTs, have been their inability to self start at low wind velocities, but it has been overcome with modifications to blade geometry and by implementing pitch control (Douak et al., 2018).

The magnitude of the wind velocity increases logarithmically with increasing altitudes within the boundary layer. Thus, the tower height of HAWTs has substantially increased over the years, allowing them to tap into higher wind velocities. Whereas the power output of VAWTs are significantly limited by their height, due to increased tower precession and larger blade fatigue with an increase in height (Paraschivoiu, 2002). Finally, the complex 3 dimensional (3D) aerodynamics of VAWTs, compared to rather simpler and well-understood HAWT aerodynamics, has been a major impediment to its growth.

2.2 BASIC AERODYNAMICS OF VAWTS

This section presents a review of the literature on basic aerodynamic principles of a lift driven, straight bladed, H-rotor VAWT. Section 2.2.1 presents a discussion on the dimensionless quantities used to describe flow and turbine parameters. In Section 2.2.2, the blade-element theory for VAWTs is discussed. Subsequently, Section 2.2.3 provides the basic approach to blade-element momentum (BEM) theory for HAWTs and VAWTs

2.2.1 Dimensionless quantities

In fluid dynamics, it is a common practice to use dimensionless quantities to characterize the behaviour of the flow. Several forces act on a fluid in motion such as inertial forces due to the mass of the fluid in motion, static pressure forces, viscous forces, surface tension, gravitational forces *etc*. The magnitudes of the dimensionless numbers associated with these forces determine the characteristics of the flow. Table 2.1 shows the various dimensionless numbers relevant to a wind turbine operation. The fluid properties are the static pressure (p), dynamic viscosity (μ), fluid density (ρ) and the fluid velocity (v).

vs.	**Inertial forces**	**Viscous forces**	**Gravitational forces**
Inertial forces	$\rho v l$	Re	Fr
Viscous forces	Re^{-1}	μ	
Gravitational forces	Fr^{-1}		g

Table 2.1: The dimensionless numbers characterizing the flow, for the operation of a wind turbine.

The Reynolds number (Re) is defined as the ratio of the inertial forces to the viscous forces, given by Equation 2.1, where l is the characteristic length; which in the case of the airfoil, is the chord length (c) and in case of the rotor, is the rotor diameter (D). The Froude number (Fr) is the ratio of the inertial forces to the gravitational forces given by Equation 2.2, where g is the acceleration due to gravity. The Mach number (M) is defined as the ratio of the velocity of the fluid (v) to the speed of sound (V_s), shown in Equation 2.3.

$$Re = \frac{\rho v l}{\mu} \tag{2.1}$$

$$Fr = \frac{v}{\sqrt{gl}} \tag{2.2}$$

$$M = \frac{v}{V_s} \tag{2.3}$$

Dynamic pressure (q), given by Equation 2.4, represents the pressure exerted by the fluid by the virtue of its motion. It is used to non-dimensionalize the aerodynamic lift and drag forces on the blade. The parameter reduced frequency (k_r), used to determine the degree of unsteadiness of the flow, is given by Equation 2.5, where f is the pitching frequency of the blade. For $k_r = 0$, the flow can be considered steady. Whereas for values of $k_r < 0.05$, the flow is considered as quasi-steady and for higher values of k_r the flow is considered as unsteady. The Courant number (Co) defined as shown in Equation 2.6, is a dimensionless quantity used to evaluate the accuracy of the CFD simulations with regard to the chosen time step settings. The term Δx_i (with the repeated index indicating summation) indicates the length interval of the discretized cell in the domain along X, Y and Z axes, the term v_i represents the respective components of flow velocity and Δt is the chosen time step. In CFD simulations, the Courant number should be less than or equal 1 for the results to be accurate. The Strouhal number (St) is a parameter used to describe the oscillating behaviour of the flow. This is given by Equation 2.7 where f is the frequency of vortex shedding and l is the characteristic length of the body causing the shed vortex. In the case of VAWT rotor, the characteristic length can be taken as turbine diameter (D).

$$q = \frac{1}{2}\rho v^2 \tag{2.4}$$

$$k_r = \frac{\pi f c}{v} \tag{2.5}$$

$$Co = v_i \frac{\Delta t}{\Delta x_i} \tag{2.6}$$

$$St = \frac{fl}{v} \tag{2.7}$$

The tip speed ratio (TSR) (λ) is defined as the ratio of the speed of the blade to the freestream wind speed (V_∞). This is shown in Equation 2.8, where R is the rotor radius and Ω is the rotational speed of the rotor. The solidity (σ) of the rotor, defined as the ratio of blade area to the planar swept area of the rotor, is given by Equation 2.9, where B is the number of blades. The aspect ratio(AR) of the rotor is defined as the ratio of the blade length(H) to the diameter of the rotor, shown in Equation 2.10.

$$\lambda = \frac{\Omega R}{V_\infty} \tag{2.8}$$

$$\sigma = \frac{Bc}{2R} \tag{2.9}$$

$$AR = \frac{H}{2R} \tag{2.10}$$

2.2.2 Blade-element theory for VAWTs

To analyse the basic aerodynamic principles, a 2 dimensional (2D) section of the rotor is taken and the forces generated by the airfoil are calculated. This approach to calculating the blade forces is commonly referred to as the blade-element theory. Figure 2.2 shows the relevant angles and velocities associated with the rotor.

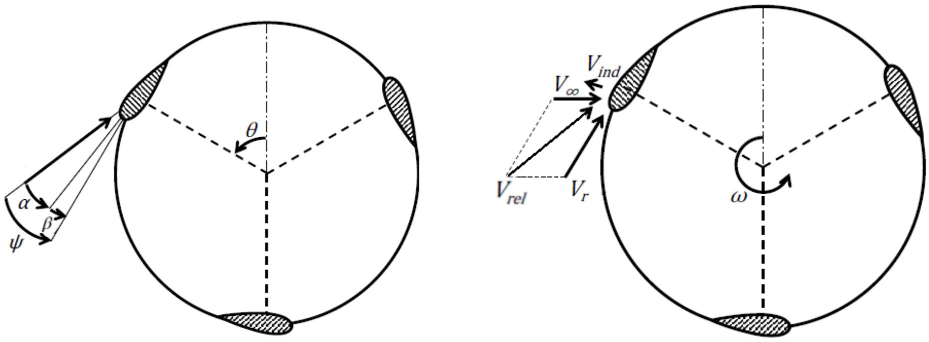

(a) Angles for aerodynamic analysis. **(b)** The velocity diagram for a VAWT rotor.

Figure 2.2: The angles and velocity diagram for a 2D section of VAWT.

A moving airfoil perceives the relative velocity of air rather than the freestream velocity ($\vec{V}_\infty$) due to the virtue of its motion. This relative velocity of the air is calculated as shown in Equation 2.11. The parameter $\vec{V}_{rel}$, is the relative velocity of the wind with respect to the moving blade and $\vec{V}_r$ is the blade velocity and $\vec{V}_{ind}$ is the induced velocity at the blade. The blade velocity can also be expressed in terms of the angular velocity of the rotor ($\vec{\Omega}$) as $\vec{V}_r = \vec{\Omega} \times \vec{R}$.

$$\vec{V}_{rel} = \vec{V}_r + \vec{V}_\infty + \vec{V}_{ind} \tag{2.11}$$

The inflow angle (ψ) is defined as the angle between the relative velocity vector ($\vec{V}_{rel}$) and the tangent to the blade path. The chord line is a straight line joining the leading and trailing edges of the airfoil. The AOA (α) is defined as the angle between the chord line and relative velocity vector ($\vec{V}_{rel}$). The blade pitch angle (β) is defined as the angle between the tangent to the blade path and the chord line. The azimuthal angle (θ) is defined as the angle between the reference axis (refer Figure 2.2b) and the location of the airfoil.

If the direction of the freestream wind velocity is taken along the X-direction and Y-axis is taken in a mutually perpendicular direction, then the relative velocity components along X (V_x) and Y (V_y) can be written as shown in Equation 2.12. The relative velocity components in the tangential and normal directions to the blade path are given by V_t and V_n respectively. The AOA(α) and inflow angle(ψ) is then given by Equation 2.13

$$\begin{aligned}
V_x &= V_\infty + \Omega R cos(\theta) + V_{ind,x} \\
V_y &= \Omega R sin(\theta) + V_{ind,y} \\
V_t &= V_x cos(\theta) + V_y sin(\theta) \\
V_n &= V_x sin(\theta) - V_y cos(\theta)
\end{aligned} \tag{2.12}$$

$$\begin{aligned}
&\alpha = tan^{-1}(\frac{V_n}{V_t}) - \beta \\
&\psi = \alpha + \beta
\end{aligned} \tag{2.13}$$

The airfoil in a flow field exerts pressure and shear forces on the flow, while the flow exerts an equal force on the airfoil. These forces exerted on the airfoil by the flow, can be resolved along and perpendicular to the relative velocity vector ($\vec{V}_{rel}$). The forces resolved perpendicular to $\vec{V}_{rel}$ is defined as lift while the forces parallel to $\vec{V}_{rel}$ is defined as drag. Equation 2.14 gives the expressions for lift (L_{2D}) and drag (D_{2D}) forces per unit span of the blade respectively. c_l and c_d are the lift and drag coefficients per unit span length respectively, which are functions of the Reynolds

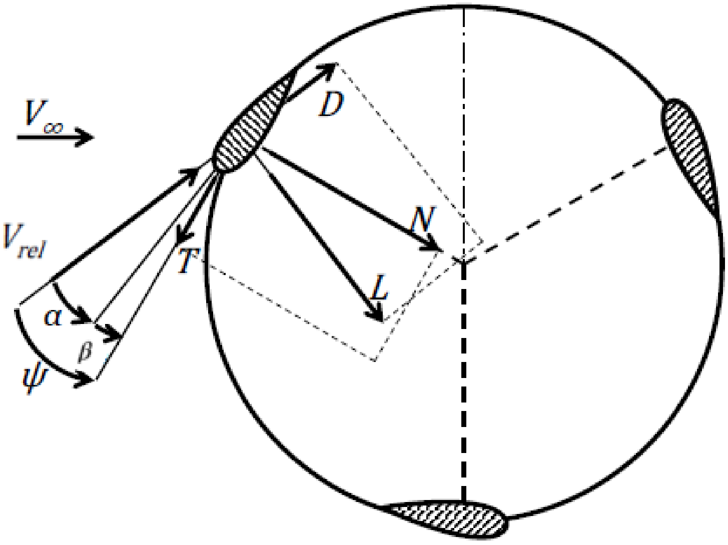

Figure 2.3: Aerodynamic forces on 2D section of the blade.

number (Re) and AOA (α). Figure 2.3 shows the force diagram for the 2D section of VAWT. The resultant of lift and drag forces is calculated by taking the vectorial sum of the forces. The components of this resultant force in the directions normal (R_n) and tangential (R_t) to the blade path is given by Equation 2.15. The tangential component (R_t) provides the torque to drive the turbine.

$$\begin{aligned} L_{2D} &= \frac{1}{2}\rho V_{rel}^2 c c_l(\alpha, Re) \\ D_{2D} &= \frac{1}{2}\rho V_{rel}^2 c c_d(\alpha, Re) \end{aligned} \tag{2.14}$$

$$\begin{aligned} R_n &= L_{2D} cos(\psi) + D_{2D} sin(\psi) \\ R_t &= L_{2D} sin(\psi) - D_{2D} cos(\psi) \end{aligned} \tag{2.15}$$

The equation for the average power (P_{2D}) for one rotation of the rotor, with the time period of rotation (T) can be written by integrating the product of the number of blades (B), the tangential component (R_t) of the resultant force and the velocity of the blade over the time period, as shown in Equation 2.16. The instantaneous thrust force (T_{2D}) on the rotor, is the component of the resultant force on the blade parallel to the inflow wind velocity. This thrust force is calculated as shown in Equation 2.17. The average thrust force (T_{2D}) is then calculated as shown in Equation 2.18.

$$P_{2D,avg} = \frac{1}{T}\int_0^T B \cdot R_t \cdot \Omega R dt \tag{2.16}$$

$$T_{2D} = R_n sin(\theta) - R_t cos(\theta) \tag{2.17}$$

$$T_{2D,avg} = \frac{1}{T}\int_0^T B \cdot T_{2D} dt \tag{2.18}$$

Finally the average power coefficient ($C_{p,avg1}$) of the turbine, per unit span of the blade, for one complete rotation, can be calculated by non-dimensionalizing the average power, with the product of dynamic pressure of the freestream wind (q_∞) and freestream wind velocity, as shown in Equation 2.19. Similarly the average

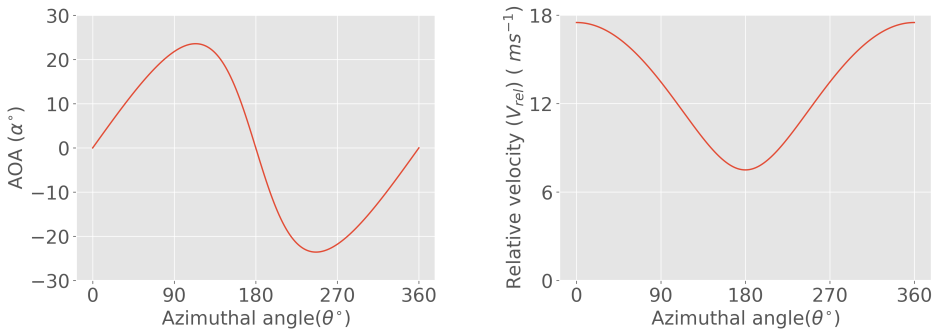

(a) Angle of attack(α).

(b) Relative velocity(V_{rel}).

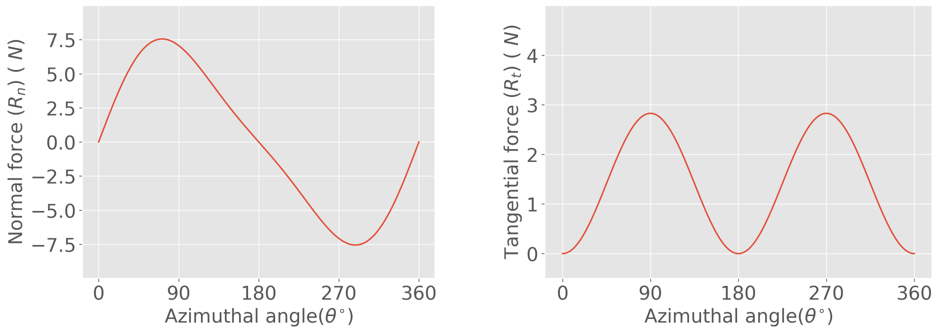

(c) Resultant normal force(R_n).

(d) Resultant tangential force(R_t).

Figure 2.4: The variation of various parameters of 2D VAWT with azimuthal angle. The parameters are defined with the chord length of $c = 0.03m$, TSR of $\lambda = 2.5$, number of blades as $B = 1$, freestream wind velocity of $V_\infty = 5ms^{-1}$, lift coefficient of $c_l = 2\pi sin(\alpha)$ and drag coefficient of $c_d = 0$. The induced velocities are ignored.

thrust coefficient ($C_{t,avg1}$) on the actuator surface can be expressed as shown in Equation 2.20

$$C_{p,avg1} = \frac{P_{2D,avg}}{q_\infty V_\infty} \tag{2.19}$$

$$C_{t,avg1} = \frac{T_{2D,avg}}{q_\infty} \tag{2.20}$$

For a constant blade pitch angle, Equation 2.13 predicts that the AOA and the relative velocity, change with the azimuthal position of the blade. This results in the change of lift and drag forces on the blade with the azimuthal position leading to a fluctuating torque. Figure 2.4 shows these varying parameters over one revolution of the blade for assuming a single-bladed rotor with no induced velocities. Further, the lift coefficient is calculated with flat plate assumptions and drag forces are neglected. The continuous change in the AOA, as seen in Figure 2.4a, causes several unsteady effects in VAWTs. Figure 2.4b shows the variation of the magnitude of the relative velocity with the azimuthal angle. Figure 2.4c and Figure 2.4d show the variation of normal and tangential forces on the rotor. The addition of more blades to the rotor at different azimuthal positions has a flattening effect on the force curves of the turbine. Further, as the blade pitch angle changes, these force curves also change. This is the basis for pitch control in VAWTs. It has been observed that the performance of VAWTs can be significantly improved by employing pitch control (Ferreira, 2009; Erfort et al., 2020).

2.2.3 Blade-element momentum (BEM) theory

The blade-element momentum (BEM) theory is a direct application of the momentum theory and blade-element theory. The momentum theory approximates the flow with several assumptions. The most basic case of the flow is assumed to be steady, inviscid, irrotational and incompressible with no skin drag at the airfoil surface. The control volume is approximated as a stream tube with uniform inflow and no mass or momentum transfer in the direction lateral to the flow. The induced velocity at the rotor is assumed to be uniform at all points of the stream tube. The stream tubes are assumed to be independent of each other and exert thrust on the rotor surface. Further, the flow is assumed to be axis-symmetric. However, several correction models are available to alleviate the inaccuracies arising from these assumptions.

BEM theory for HAWTs :
The momentum theory calculates the induced velocity at the rotor by solving the mass, momentum and energy balance equations in the direction of the flow within the control volume. The rotor is approximated as an actuator disk that exerts thrust force on the flow. The axial induction factor (a) is defined as shown in Equation 2.21, where V_∞ is the freestream wind speed and V_d is the magnitude of wind velocity at the rotor (Sørensen, 2012).

$$a = 1 - \frac{V_d}{V_\infty} \tag{2.21}$$

The loading on the blades in a HAWT is calculated using blade-element theory, similar to the approach shown in Section 2.2.2. The blade is split up into several unit span sections and the lift and drag forces at each of these sections are calculated by including the induced velocity calculated from momentum theory. The total loading on the blade is calculated by summing up the resultant forces on the different sections of the blade. The average torque on the rotor is ultimately calculated by averaging the instantaneous torque over one revolution. The combination of blade-element theory with the momentum theory is called BEM theory first introduced by Glauert (1935) for modelling HAWTs.

BEM theory for VAWTs :
While the BEM theory for VAWTs follows a similar approach, the techniques to model the actuator surfaces is different. Since the blades of the VAWT have a component of velocity along the wind direction, the single actuator disk approximation of the rotor is not entirely appropriate. The different approaches to model a VAWT rotor, are discussed in detail in Section 2.5. Based on the number of stream tubes and actuator surfaces, several momentum models exist for VAWTs. A detailed discussion on these different momentum models is presented in Section 2.6.1.

2.3 UNSTEADY AERODYNAMICS OF VAWTS

The operation of a VAWT is dominated by unsteady effects, predominantly due to the rotation of the blades. This rotation causes a sinusoidal change in the AOA (refer Figure 2.4a), that changes the lift force on the airfoil and hence the bound circulation around it. The cyclic change in AOA means that the occurrence of dynamic stall is imminent. The change in the bound circulation leads to the periodic shedding vortices on the suction side of the airfoil. These shed vortices, interact with the blades downstream as it traverses along the wind direction, commonly referred to as blade-wake interaction. The rotation of the blades also causes the airfoil to perceive a varying AOA at different chord-wise locations, commonly known as the

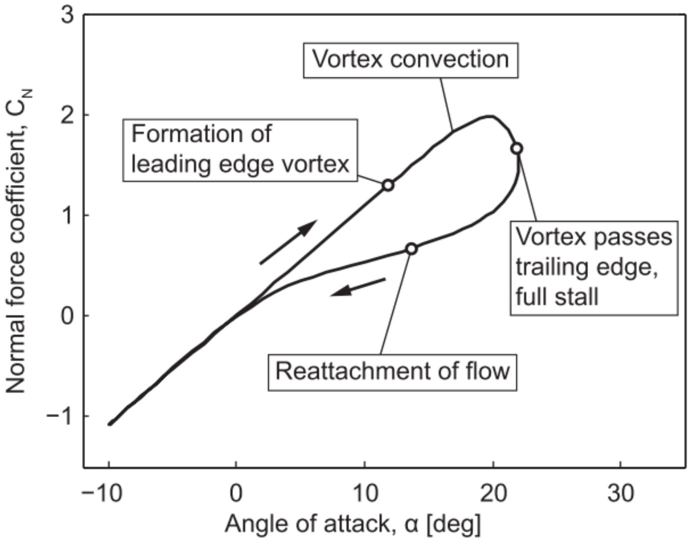

Figure 2.5: The variation of normal force coefficient (C_n) with AOA (α) for NACA 0015 blade profile with the following parameters : $\alpha = 6 + 16 sin(\omega t)$, reduced frequency $k = 0.1$, Mach number $M = 0.1$ and chord length $c = 0.5m$. (Dyachuk and Goude, 2015)

flow curvature effect. All these unsteady effects significantly affect the performance and consequently, the wake of a VAWT.

The phenomenon of the dynamic stall and the parameters affecting it are discussed in detail in Section 2.3.1. A brief discussion of the different models available to model dynamic stall is also included in this subsection. The phenomenon of blade-wake interaction is elaborated in Section 2.3.3. The flow curvature effect is discussed in Section 2.3.2.

2.3.1 Dynamic Stall

Dynamic stall is an unsteady effect that occurs when the airfoil undergoes rapid changes in AOA near the static stall AOA. Hence, it is noted that the value of the static stall angle is one of the determinant factors for the occurrence of the dynamic stall. The occurrence of dynamic stall delays the onset of the stall and causes lift forces to increase beyond their maximum value at static stall AOA. Figure 2.5 presents the variation of the normal force coefficient of the blade as a function of AOA. From the figure, it can be observed that a hysteresis loop occurs in the normal force (and hence lift force), which means, both the flow separation and flow reattachment is delayed as a result of dynamic stall. The occurrence of dynamic stall is generally categorized into four regimes (Wernert et al., 1996):

- Attached flow and generation of instability at the leading edge of the airfoil creating a leading-edge separation.
- Formation of the leading-edge vortex.
- Convection of the leading-edge vortex over the airfoil surface and formation of the trailing-edge vortex.
- Reattachment of the flow.

Dynamic stall occurring in a VAWT, is affected by several different parameters. These parameters are the chord Reynolds number (Re_c), Mach number (M), blade profile and geometry, TSR, reduced frequency (k_r) and turbulence intensity (I) (Peng et al., 2021). Simulations by Sangwan et al. (2017) show that the effect of dynamic stall becomes less pronounced with increasing Mach number (and consequently with increasing Re_c for a given airfoil and fluid). Wang et al. (2014); Rezaeiha et al. (2018) agree that the turbulence intensity has a significant impact the onset of dynamic stall and that stall can be delayed by higher turbulent intensities in low Re_c flows. Wang et al. (2014) notes that this is due to effect of turbulent reattachment of the flow in the boundary layer (shown in Figure 2.6). They further note that the increase in turbulence intensity bears resemblance to increase in the Re_c, with a few exceptions. In the experiments conducted by Laneville and Vittecoq using NACA0018 blade profile with the static stall AOA of ± 10.5 degrees, it was observed that the dynamic stall occurred below TSR of 5 and deep stall occurred below TSR of 3. From the velocity diagram shown in Figure 2.2b, it can be seen that low TSR of operation can cause blades to reach high values of AOA, significantly exceeding the static stall AOA. This is reiterated quantitatively in the Particle Image Velocimetry (PIV) measurements by Simao Ferreira et al. (2007) using NACA0015 blade geometry with parameters: $Re_c = 5 \times 10^4$ and 7×10^4, inflow velocities ranging $3.7ms^{-1} - 10.5ms^{-1}$ and TSRs ranging from 2 to 4 . However, it is noted that the static stall angle of the airfoil has a detrimental role in deciding the TSR at which dynamic stall occurs. Further, Hau et al. (2020) show that an increase in the reduced frequency (k_r) increases the stall onset angle, potentially delaying the onset of dynamic stall. Further, it can be inferred that any change to the blade pitch angle (β) acts to change the azimuthal position at which the onset of the dynamic stall occurs.

Dynamic Stall Modelling :
Several dynamic stall models (Gormont, 1973; Paraschivoiu and Allet, 1988; Proulx and Paraschivoiu, 1989) have been proposed for VAWTs by various authors (Strickland et al., 1979; Massé, 1981; Berg, 1983; Paraschivoiu et al., 1988; Masson et al., 1998) in the available literature. The dynamic stall models were initially developed to model the aerodynamic loading and flow around helicopter blades. This section presents a general approach to modelling the dynamic stall and provides a reasoning for the chosen dynamic stall models for further comparison.

All the available dynamic stall models are semi-empirical implying that, the empirical constants of the model are largely dependent on the experimental data and the airfoil used. However, Dyachuk et al. show that the results obtained by implementing a dynamic stall model are still better than those without the dynamic stall model. The Beddoes-Leishman (B-L) dynamic stall model has four sub-models as enumerated below:

- Unsteady attached flow model.
- Non-linear trailing-edge separation model.
- Dynamic stall onset model.
- Vortex induced loading model.

The comparison of B-L-original (Leishman and Beddoes, 1986), B-L-3G (Beddoes, 1993), B-L-Sheng-Galbraith-Coton (SGC) (Sheng et al., 2008) and Gormont models, by Dyachuk et al. (2014), shows that B-L-SGC model shows a better result in comparison to the experiments. However it is noted that the simulation was carried out using momentum models, although the author mentions that they work well with Navier-Stokes (N-S) flow models. B-L-original was developed by Leishman and Beddoes to model the flow around the helicopter rotors. A third generation version of this was later developed by Beddoes. Later, Sheng et al. identified that the prediction of unsteady aerodynamic blade loading by B-L models is worse at low Mach numbers than at higher Mach numbers. The deficiencies of the standard B-L models at low Mach numbers include early prediction of the stall, exclusion of the stalled flow convection over the upper surface of the airfoil and negative chordwise forces in separated flow. The B-L-SGC model proposed by Sheng et al. (2008), overcomes these

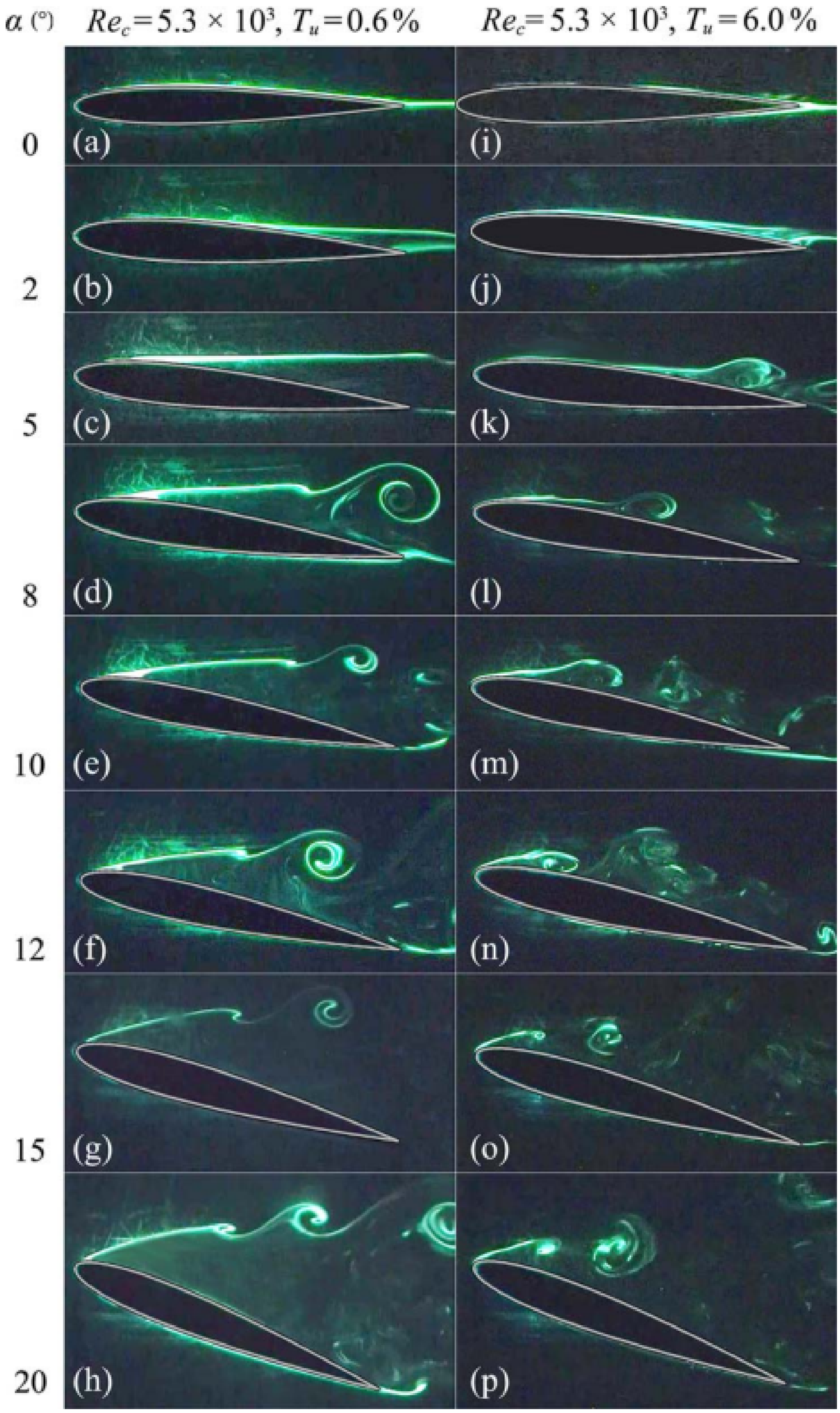

Figure 2.6: Effect of turbulence intensity ($I = T_u$) on stall at different AOA a low Re_c flow. (Wang et al., 2014)

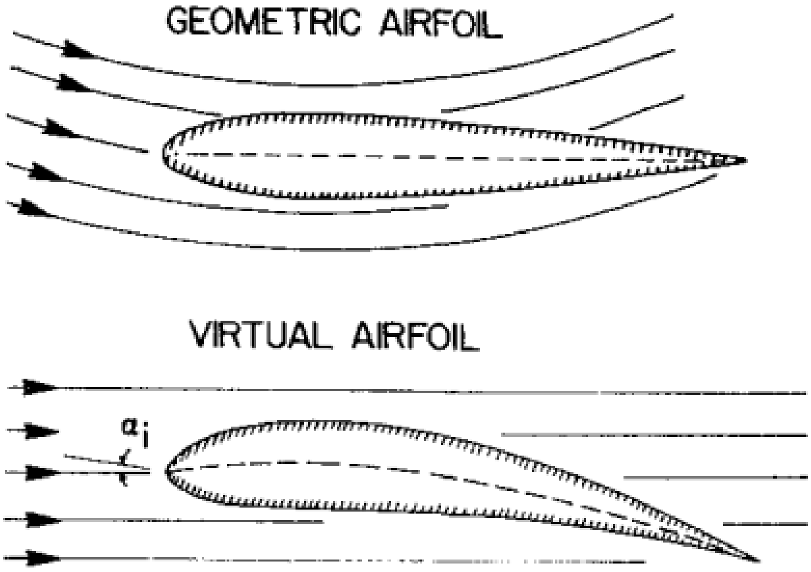

Figure 2.7: Virtual camber, a qualitative representation of the conformal transformation. (Migliore et al., 1980)

deficiencies and is chosen as an appropriate dynamic stall model for the baseline case. However, since the choice of dynamic stall model is crucial for the accuracy of the results in low Re_c, low TSR regimes (Masson et al., 1998), the effect of dynamic stall on the simulation results is investigated in Chapter 4.

2.3.2 Flow curvature

The curvilinear motion of the blades has the effect of altering the AOA perceived by the airfoil at different chord locations. This follows from the geometric observation that the radial distance from the axis of rotation to every point on the chord of the airfoil is unique. This makes the direction of relative velocity and hence the AOA unique to every point on the chord. This was highlighted in a study by Migliore et al. (1980), who noted that the effect of the rotating airfoil in the curvilinear flow field, behaved the same way as a cambered airfoil in a linear flow field. This is known as virtual camber and is shown in the figure Figure 2.7. This effect becomes important while modelling the VAWTs with higher solidities ($\frac{c}{R} > 0.1$) (Migliore et al., 1980).

2.3.3 Blade-wake interaction

The sinusoidal change in the AOA continually changes the lift forces and hence the bound circulation around the blades, as governed by the Kutta-Joukowski theorem (refer Equation 2.36). A consequence of this is that the vortices are shed from the trailing edge periodically with the change in bound circulation as per Kelvin's circulation theorem (Paraschivoiu, 2002). It is to be noted that this is different from the leading-edge vortex that is shed with the occurrence of dynamic stall. When these vortices convect downstream with the wake they encounter the rotating blades in the downwind half. A study conducted by Scheurich et al. (2011) shows that these interactions significantly modify the induction field around the blades in the downwind half, causing impulsive changes in the aerodynamic blade loads. While the blade force curves are smooth in the upwind half, the blade-wake interactions create sudden surges in blades loading in the downwind half. The change in induction field around the blade in the wake can modify the AOA much beyond the stall angle causing a localized dynamic stall. The study also states that at higher TSRs this effect is amplified as the blade encounters its own wake in the downwind half and hence, the frequency of blade-wake interaction is increased.

2.4 WIND TURBINE WAKES

The wake of a wind turbine is a consequence of its extraction of kinetic energy from the wind. The obstruction or the blockage to the wind created by the presence of a wind turbine generates eddies or vortices. The largest of these vortices are of the length scales of the turbine diameter. The core of the vortex has the same translational velocity as the convection velocity of the vortex, which is significantly low compared to the inflow velocity. This causes the large velocity deficit in the region behind the turbine, called as the wind turbine wake. These eddies in the wake, interact with each other and stretch, as they convect with the wind. The largest eddies extract kinetic energy from the mean flow, dissipating into smaller eddies through vortex stretching further downstream. The dissipation of these eddies leads to a recovery of the wake far downstream. The wake of a VAWT, its properties and the governing parameters are discussed in Section 2.4.1. The wake deflection in VAWTs is discussed in Section 2.4.2.

2.4.1 Wake of a VAWT

The wake of a VAWT is similar to that of a HAWT in the general structure, *i.e.* with high velocity deficits and turbulence intensities. However, they are intrinsically different. The VAWT wake is characterized by strong asymmetry, counter-rotating vortices (Peng et al., 2021), and with the shed and trailing vorticity as the wake's main components. Whereas the HAWT wake's main component is the trailing vorticity with strong tip vortices (Ferreira et al., 2010). The blade-wake interactions in VAWTs cause higher turbulence intensities in the wake, leading to almost 95% of the velocity recovery in the wake at downstream distances of $6D$, whereas the HAWTs needs a downstream distance of $14D$ for the same percentage of recovery (Kinzel et al., 2012).

The wake in this study, is classified into three regions, namely; near-wake (downstream distances $x \leq 3D$), a transition zone ($4D \leq x \leq 7D$) and far-wake (downstream distances $x \geq 8D$). While there is no general consensus on the above-mentioned classification of the regions, it provides a comprehensible approach for the following discussions. The main components of the VAWT wake are the shed vorticity and trailing vorticity, whose largest component is the tip vortex. The near-wake velocity contours obtained from stereoscopic PIV measurements for VAWT are shown in Figure 2.8. These measurements by Tescione et al. (2014) show that the vorticity field in the near-wake ($\frac{x}{R} < 3$) of the turbine is highly affected by the blade wakes. However, Tescione et al. note that, for larger downstream distances the cycloidal shape of the blade wakes are no longer detectable. The asymmetry associated with the VAWT wake (seen in Figure 2.8a) is explained by the blade rotation, blade-wake interaction and enhanced by the velocity deficit in the windward region (Ferreira et al., 2007; Tescione et al., 2014). The wake of the tower also has a slight asymmetry towards the windward side, owing to the Magnus effect caused by the rotation of the tower. Tescione et al. further note this could also add to the asymmetry of the turbine wake itself. The far wake of the VAWT is dominated by oscillating bluff-body aerodynamics. Araya et al. (2017) note that the dynamics of the far-wake resembles that of the solid cylinder. The study further states that the far-wake of a VAWT has similar properties as that of the HAWT, with wake meandering that oscillates with a Strouhal number of $St = 0.23$, irrespective of the operating conditions. The transition zone of the wake is the region where the transition occurs from the blade vortex dominated near-wake to the bluff-body aerodynamics of far wake. The latter resembles the wake generated by a solid cylinder in the flow with oscillations determined by the resultant Strouhal number.

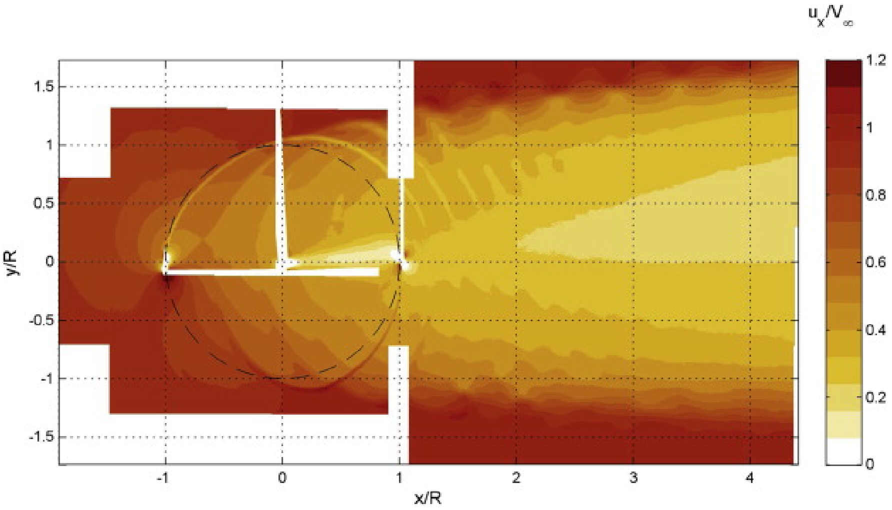

(a) Normalized stream-wise velocity (u_x) contour in the near-wake of VAWT

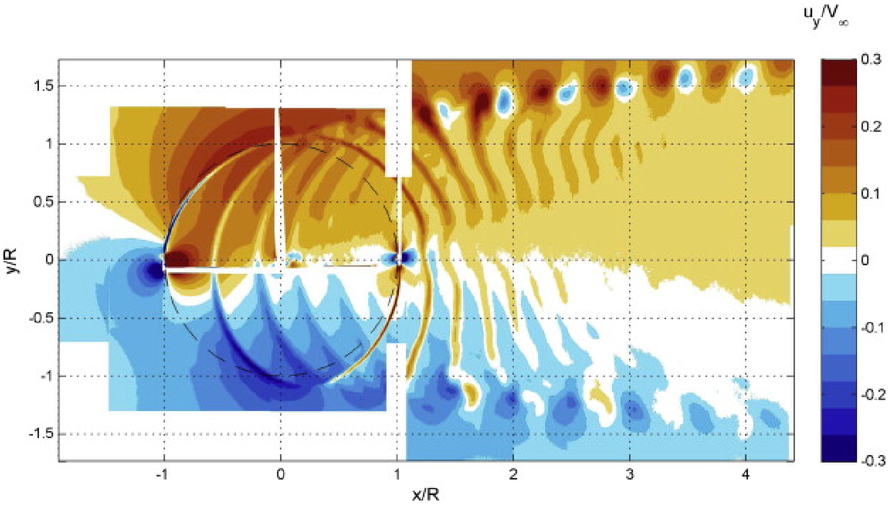

(b) Normalized cross-stream velocity (u_y) contour in the near-wake of VAWT

Figure 2.8: Near-wake velocity contour of VAWT measured using stereoscopic PIV measurements (Tescione et al., 2014).

The geometric and operational parameters of a VAWT, like the solidity, aspect ratio and TSR, affect its wake structure and wake aerodynamics. With the increase in the solidity of the VAWT, the velocity deficit in the near wake increases (Zou et al., 2020). The study further shows that the increase in solidity by increasing the chord length and by increasing the number of blades have different effects on the power coefficient and hence the wake deficit. The increase in solidity due to the increase in chord length, marginally increases the optimal power coefficient up to a certain chord Reynolds number (Re_c), beyond which enhanced blade-wake interactions are observed. The increase in solidity due to the increase in the number of blades has a negative impact on the power coefficient due to increased blade-wake interactions. Zou et al. also note that the asymmetry of the wake increases with the increase in solidity and the wake transforms from a V-shape to U-shape, with enhanced wake recovery. Hezaveh et al. (2017) and Zou et al. (2020) both observe re-circulation

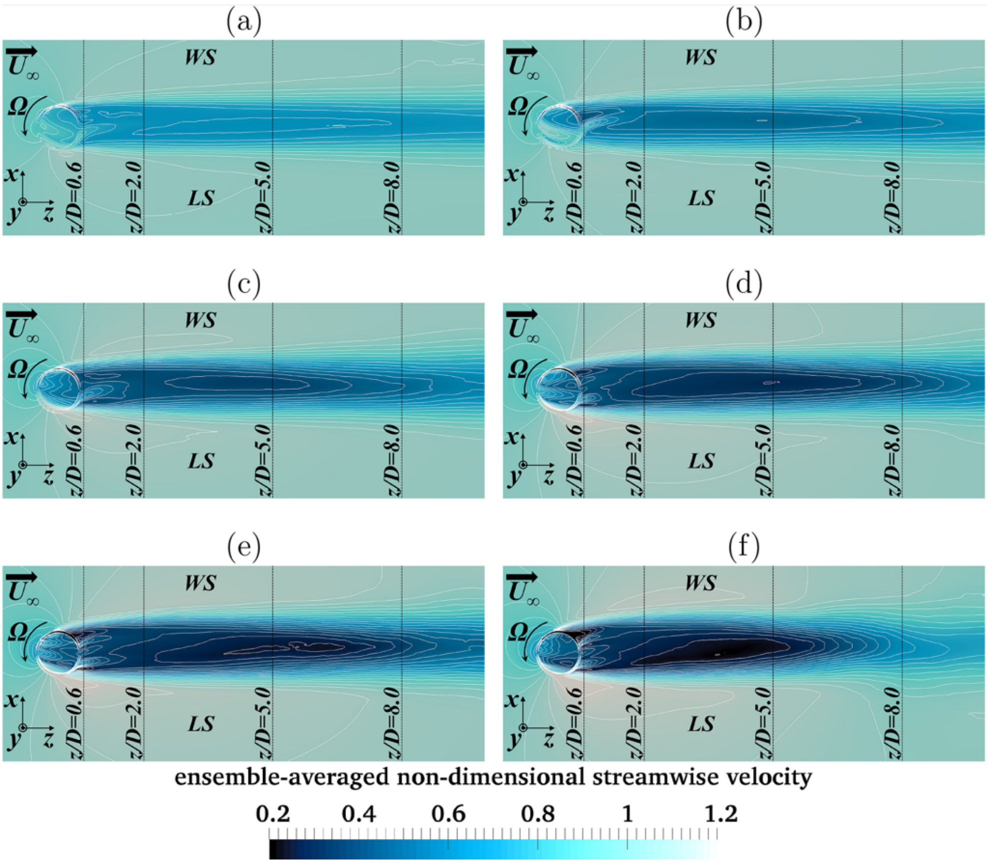

Figure 2.9: The effect of TSR on the wake of a VAWT with the cases showing increasing TSR (a): $\lambda = 1$, (b): $\lambda = 1.35$, (c): $\lambda = 1.8$, (d): $\lambda = 2.21$, (e): $\lambda = 2.6$ and (f): $\lambda = 3$. WS representing windward side and LS representing leeward side (Posa, 2020).

in the near-wake downstream locations for higher solidities, leading to a higher turbulent diffusion of the wake and enhanced recovery far downstream.

However effects of solidity, aspect ratio and the TSR work in combination with each other to determine the structure and nature of the wake. Simulations by Hezaveh et al., show the flow reversal in the immediate downstream of the turbines with medium solidity but not for the higher solidity. This is due to the lower operational TSR of the high solidity turbine in their study. The increase in TSR increases the wake velocity deficit (refer Figure 2.9) and also enhances the wake recovery due to the collapse of shear layers of the wake into the wake core in the transition zone of the wake (Posa, 2020; Hezaveh et al., 2017). The cross-stream velocity component of the wake is also enhanced by increasing TSRs. Posa notes that at lower TSRs, where the dynamic stall effect is severe, the results show larger velocity deficits at the shed vortex core. However, this effect varies non-monotonically with the variation in TSR. The turbines with a higher aspect ratio ($AR = H/D$ defined differently from Hezaveh et al. (2017)), have shorter wakes and larger asymmetry owing to the larger momentum transport into the wake from the sides, whereas the lower aspect ratios lead to longer and wider wakes (Hezaveh et al., 2017). However, it is noted that the author, in their study, does not consider the tip effects, which has a significant impact on the wake for smaller aspect ratios. The tip vortices have a significant role in the replenishment of the stream-wise momentum of the wake by inducing crosswind velocities (Rolin and Porté-Agel, 2018).

2.4.2 Wake Deflection in VAWTs

The necessity of wake deflection arises from the need to optimize the power production of the downwind turbines in a wind farm setting. At the outset, the inherent asymmetry of the wake of an isolated VAWT leads to a slight deflection of the wake towards the windward side of the turbine. Hence the direction of rotation has a large influence on the direction of the deflected wake. Unlike the HAWT wake steering mechanism, which employs yawing of the wind turbine's axis of rotation, the wake of a VAWT can be deflected by changing the blade pitch angle (β) or the strut pitch angle (β_s). The effect of changing the blade pitch angle deflects the wake in the windward or leeward direction, whereas pitching the struts deflect the wake upwards or downwards. Owing to the effect of increased power production of two counter-rotating VAWTs in close vicinity (Hezaveh et al., 2018), several studies (Rolin and Porté-Agel, 2018; Vergaerde et al., 2020a,b; Yuan et al., 2021) have been carried out to understand the nature the deflected wake in VAWTs. Vergaerde et al. (2020a) note that the wake of two counter-rotating VAWTs with adjacent downwind moving blades, have the same wake length and widths of an isolated VAWT. Whereas the adjacent upwind motion of the blades significantly improves the wake recovery and decreases the wake widths. Since the wake asymmetry causes a deflection of the deficits in the windward direction, the adjacent downwind moving blades deflect the wakes away from each other leading to weaker wake interactions. On the other hand, higher wake interactions in the upwind adjacent moving blades result in unsteadiness leading to dissipation through vortex suppression (Vergaerde et al., 2020a). Figure 2.10 shows the comparison of the wake of two counter-rotating VAWTs cases with that of an isolated VAWT.

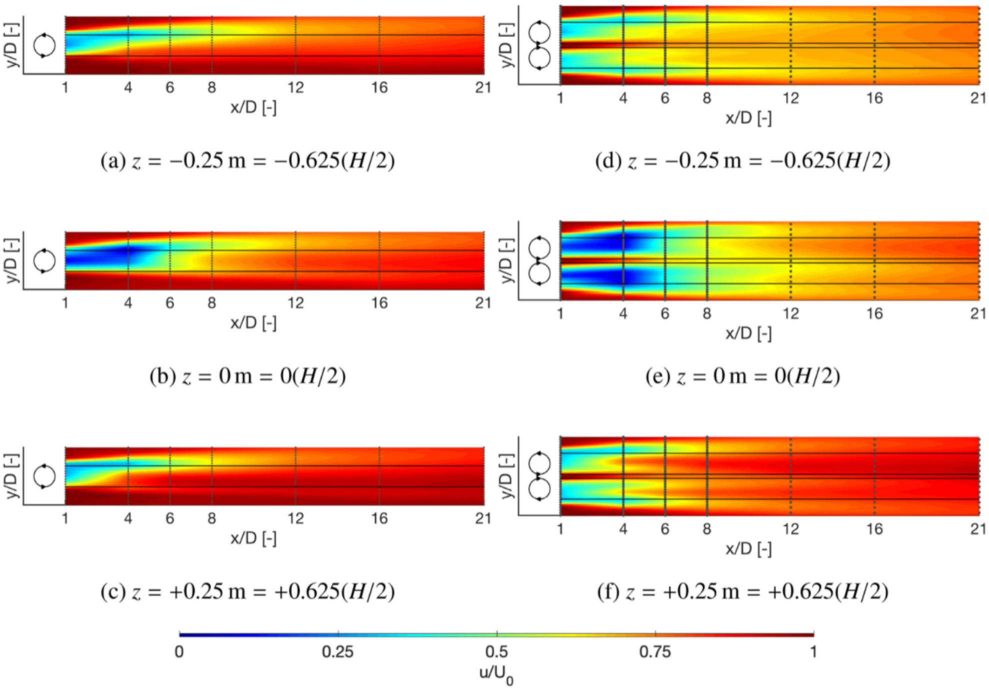

(a) $z = -0.25\,\mathrm{m} = -0.625(H/2)$

(d) $z = -0.25\,\mathrm{m} = -0.625(H/2)$

(b) $z = 0\,\mathrm{m} = 0(H/2)$

(e) $z = 0\,\mathrm{m} = 0(H/2)$

(c) $z = +0.25\,\mathrm{m} = +0.625(H/2)$

(f) $z = +0.25\,\mathrm{m} = +0.625(H/2)$

Figure 2.10: The wake of an isolated turbine as compared with the wake of a counter-rotating turbine cluster with downwind moving adjacent blades at three different vertical cross-sections. (Vergaerde et al., 2020a)

Mendoza and Goude (2019), in their study, employ strut pitching as a method to deflect the wake upwards or downwards. They use strut pitching, instead of blade pitching, since pitching the blade, while maintaining the optimal TSR would require an active pitching system and an azimuthal awareness of induction fields. Figure 2.11 shows the effect of strut pitching in deflecting the wake.

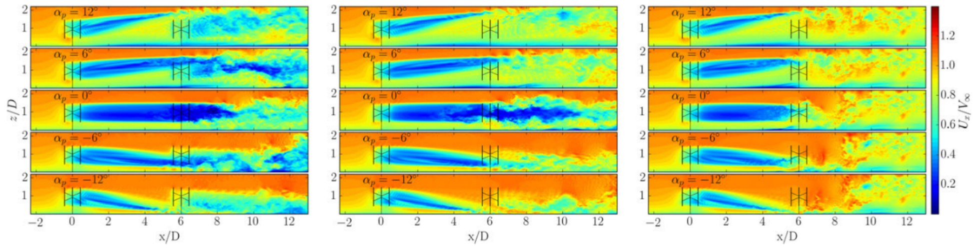

Figure 2.11: The deflection of wake as a result of different strut pitch angles (α_p), simulated using the ALM CFD. (Mendoza and Goude, 2019)

2.5 MODELLING THE VAWT ROTOR

In this section, the different rotor modelling techniques for H-VAWT with straight blades, are discussed. The main components of aerodynamic significance are the blades, the struts and the tower. Different levels of simplification exist to represent these actuator surfaces. These methods predict the blade loading and turbine performance, with varying accuracy, requiring different levels of computational expenditure. The aim of the modelling is to predict the turbine performance, blade loading, the induced velocities at the rotor and the effect of this loading on the wake. The modelling of VAWTs closely follows the techniques developed to model HAWTs.

Figure 2.12 shows various approximations of the rotor commonly available in the literature. These rotor simplifications are combined with different flow modelling techniques to effectively analyse VAWT aerodynamics. Figure 2.12a shows the 3D rotor, where the rotor has a finite span and a finite number of blades. A cross-section of the 3D rotor gives the 2D assumption of the rotor shown in Figure 2.12b. The 2D assumption inherently implies that the blade span is considered to be infinitely long in the direction of the rotor axis and hence the tip effects of the blade are neglected.

2.5.1 Actuator disk model

In the actuator disk (AD) model, the rotor is approximated with an infinitely thin, permeable disk, of an equivalent thrust coefficient, with its axis aligned perpendicular to the direction of the flow. The disk exerts a thrust force on the flow in the direction opposite to the flow and can be further split into smaller rings at different radial locations for greater accuracy. The 3D and 2D AD approximations of the rotor are shown in Figure 2.12c and Figure 2.12d respectively. This approximation of the rotor was initially developed to model HAWT rotors. It is the simplest and one of the most frequently used models for VAWT rotors. Replacing a cylindrical swept surface with an AD means, that the effects of the tower and the struts on the flow are neglected and the near-wake of the rotor is not captured well.

2.5.2 Actuator cylinder model

In this model, the rotor is replaced by the actuator surface swept by the blades over one revolution, exerting thrust force on the flow. This approximation implies an infinite number of blades along the actuator surface. In 3D, this takes the form of a thin, permeable actuator cylinder (AC) as shown in Figure 2.12e whereas, in 2D, it is a circle as shown in Figure 2.12f. The 2D cross-section implies that the span length is infinite and the tip effects are neglected. The AC approximation, first introduced by Madsen (1982), is a more appropriate approximation for a VAWT rotor compared to the AD approximation.

2.5.3 Actuator line model

This method was first introduced by Sørensen and Shen (2002) for HAWT rotors, Here, the rotor blades, struts and the tower is replaced by lines exerting an external force on the flow. The magnitude and the direction force field exerted by the lines representing the actuators can be determined by the blade-element theory or lifting line theory, along with corrections for tip and dynamic effects. Different flow modelling techniques can be combined for analysis of the wake structure (Bachant et al., 2018; Mendoza et al., 2019). A more detailed discussion on this is provided in Chapter 3.

2.6 MODELLING THE VAWT WAKE

This section presents a discussion on various flow modelling techniques available to model the VAWT wake. The aim of these models is to predict the induction at the turbine, the wake velocities and the wake structure. While the momentum models do not predict the wake structures, the vortex and CFD models do provide a better description of the wake flow field. The momentum models are elaborated in Section 2.6.1, while the vortex modelling techniques are discussed in Section 2.6.2. Finally, the high-fidelity CFD models are discussed in Section 2.6.3.

2.6.1 Momentum models

The momentum theory in combination with the blade-element theory forms the basis for these models. Depending on the number of stream tubes and the number of actuator surfaces used the 1 dimensional (1D) momentum models can be classified into 4 different categories of increasing complexity and accuracy as shown in Figure 2.13. These 1D momentum models along with the 2D AC model are briefly discussed in the subsequent sub-sections.

2.6.1.1 Single stream tube model

This model, first introduced by Templin (1974), is the simplest model available in the literature for VAWT modelling. The model approximates the VAWT rotor with the AD of equivalent thrust coefficient and the control volume of the flow with a single stream tube as shown in Figure 2.13a. The momentum theory is used to calculate the uniform induced velocity in the stream tube at the rotor. This implies that the induction at the upwind and downwind parts is assumed to be the same.

2.6.1.2 Multiple stream tube model

Following the improvements in SST model for HAWT modelling, MST model was introduced by Wilson and Lissaman (1974) and subsequently by Strickland (1975). The MST model considers the flow to be split up into several independent stream tubes to calculate the induction at the rotor as shown in Figure 2.13b. While the induction is assumed constant within the stream tubes, they can now vary from one stream tube to another. These induced velocities are calculated by solving the linear mass, momentum and energy balance equations for each independent stream tube. However, the rotor is still approximated with a single AD which means that the induction in the downwind and upwind halves of the rotor is assumed to be the same.

2.6.1.3 Double stream tube model

To address the different induction values in the upwind and downwind halves of the VAWT rotor, with 2 separate ADs can approximate the upwind and as shown in

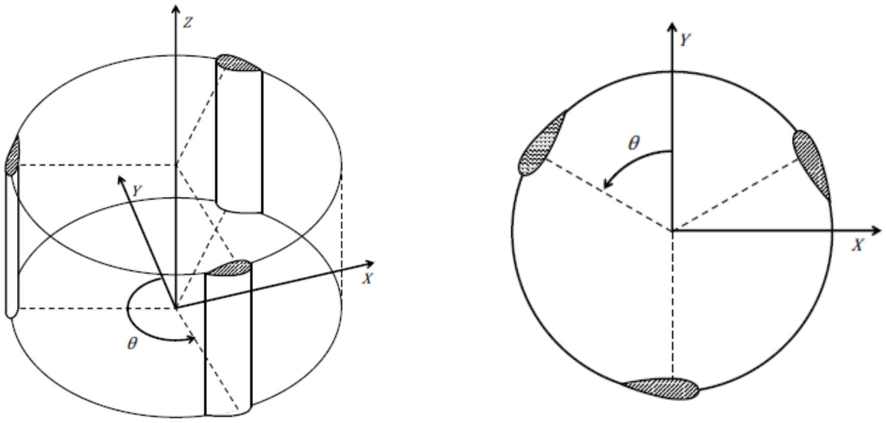

(a) 3D rotor. **(b)** 2D VAWT rotor.

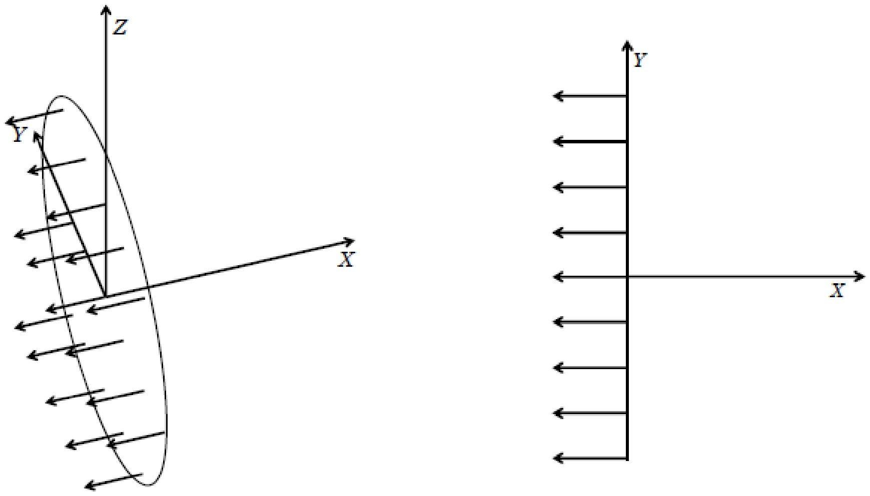

(c) 3D actuator disk (AD). **(d)** 2D actuator disk (AD).

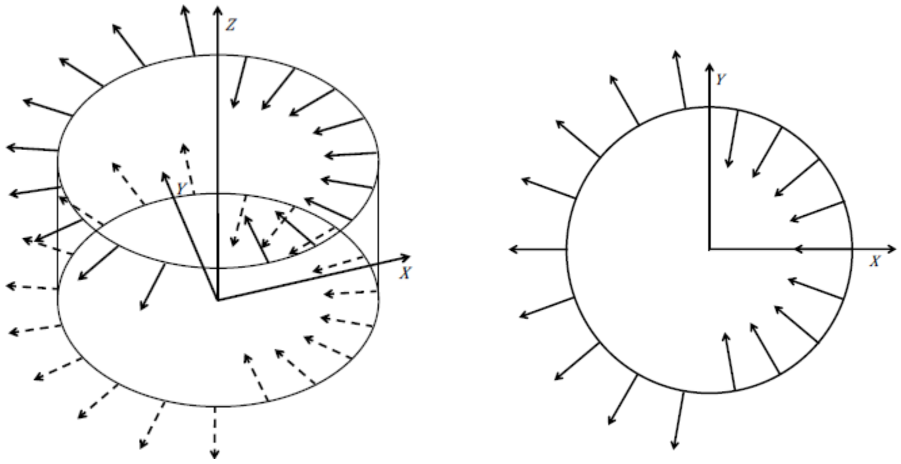

(e) 3D actuator cylinder (AC). **(f)** 2D actuator cylinder (AC).

Figure 2.12: Different levels of rotor simplifications for VAWTs (De Tavernier, 2021).

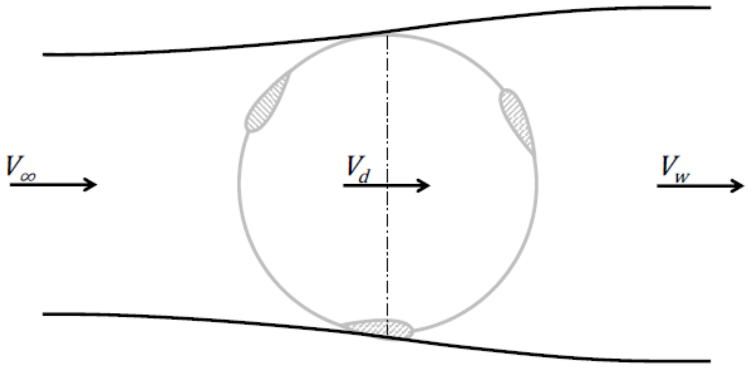

(a) Single stream tube (SST).

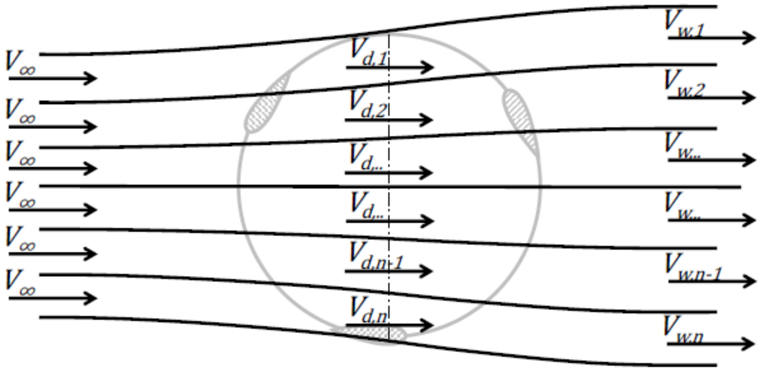

(b) Multiple stream tube (MST).

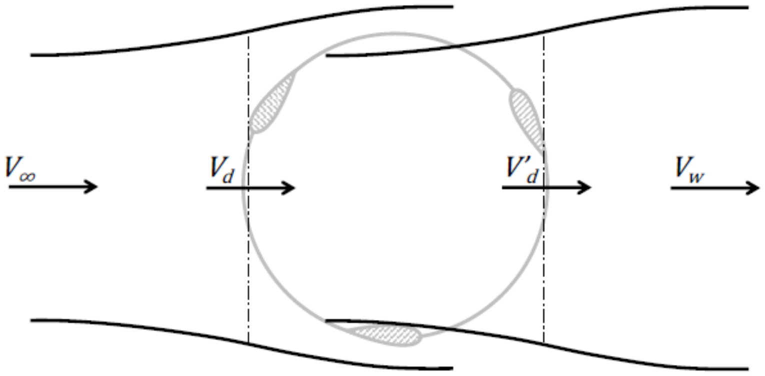

(c) Double stream tube (DST).

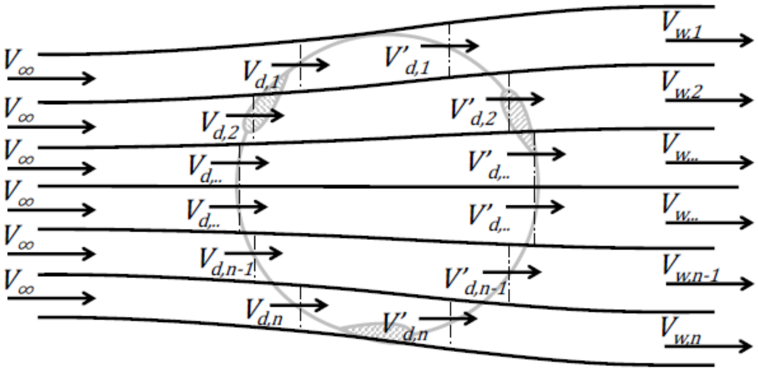

(d) Double multiple stream tube (DMST).

Figure 2.13: The different momentum models available in the literature (De Tavernier, 2021).

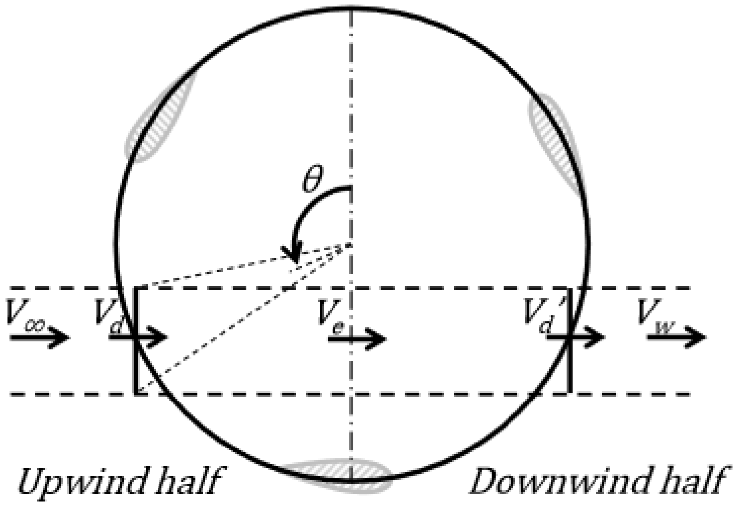

Figure 2.14: DMST model for VAWTs. (De Tavernier, 2021)

Figure 2.13c. This allows different induction values at the upwind and downwind ADs. The fully developed, far-wake velocity of the upwind AD is assumed to be the inflow velocity for the downwind AD.

2.6.1.4 *Double multiple stream tube model*

This momentum model with the AD approximation of the rotor was first introduced by Paraschivoiu (1988). Here the MST assumptions for the flow are combined with the DST approximation of the rotor, as shown in Figure 2.13d.

The working of the DMST model is briefly explained in the below section by analyzing a single stream tube located at an azimuthal angle θ. Figure 2.14 shows the upwind and downwind ADs and the corresponding stream tube under consideration. The inflow velocity (V_∞) for the upwind AD is assumed to be unidirectional along X-axis. The induced velocities at the upwind and downwind ADs are given by V_d and V_d' respectively. The fully developed far-wake velocity of the upwind AD (V_e) is taken as the inflow velocity for the downwind AD. The far-wake velocity of the downwind AD is given by V_w. The induction factors for the upwind AD (a) and downwind AD (a') are defined as given in Equation 2.22. (Paraschivoiu, 2002)

$$\begin{aligned} a &= 1 - \frac{V_d}{V_\infty} \\ a' &= 1 - \frac{V_d'}{V_e} \end{aligned} \tag{2.22}$$

From the linear mass and momentum balance equations the relation between the velocity at the inlet, at the upwind AD (V_d) and in its far wake (V_e) is given by Equation 2.23. For the downwind AD, the inflow velocity is the far wake velocity of the upwind AD (V_e). The relation between the inlet, far wake (V_w) and wind velocity at the downwind rotor (V_d') is given by Equation 2.24.

The induced velocity at the upwind and downwind ADs in terms of their respective induction factors is given in Equation 2.24. The thrust coefficient for the upwind ($C_{t,MOM}$) and downwind ($C_{t,MOM}'$) ADs are then calculated as shown in Equation 2.26.

$$V_d = \frac{V_\infty + V_e}{2} \tag{2.23}$$

$$V_d' = \frac{V_e + V_w}{2} \tag{2.24}$$

$$\begin{aligned} V_d &= (1-2a)V_\infty \\ V_d' &= (1-a')(1-2a)V_\infty \end{aligned} \tag{2.25}$$

$$\begin{aligned} C_{t,MOM} &= a(1-a) \\ C_{t,MOM}' &= a'(1-a') \end{aligned} \tag{2.26}$$

The lift and drag forces generated by the airfoil are calculated from the blade-element theory. The thrust coefficient ($C_{t,BEM}$) on the flow within the stream tube, with a surface area (A_{st}), can be calculated as shown in Equation 2.27. The instantaneous thrust force (T) is calculated by calculating the force coefficients in tangential (C_{ta}) and normal (C_n) directions. The average thrust force (T_{avg}), on the actuator surface, is calculated by multiplying the instantaneous thrust force with the number of blades (B) and the width of the stream tube. The term $\Delta\theta$ represents the azimuthal width of the stream tube and H is the length of the blade.

$$\begin{aligned} C_{t,BEM} &= \frac{T_{avg}}{0.5\rho V_\infty^2 A_{st}} \\ where: & \\ T_{avg} &= \frac{B\Delta\theta}{2\pi}T \\ T &= 0.5\rho V_{rel}^2 c(C_{ta}\cos\theta - C_n\sin\theta) \\ C_{ta} &= C_l\sin\psi - C_d\cos\psi \\ C_n &= C_l\cos\psi + C_d\sin\psi \\ A_{st} &= R\Delta\theta\sin\theta H \end{aligned} \tag{2.27}$$

From the above equations, the thrust coefficient for the upwind and downwind ADs can be calculated as shown in Equation 2.28. Equating the corresponding thrust coefficients calculated from momentum theory ($C_{t,MOM}$) with the thrust coefficients calculated from BEM theory ($C_{t,BEM}$), the corresponding upwind and downwind induction factors are calculated. This is an iterative process where the initial value of the induction factor is assumed and the above process is reiterated until the convergence is reached.

$$\begin{aligned} C_{t,BEM} &= \frac{Bc}{R}\frac{1}{2\pi}(\frac{V_{rel}}{V_\infty})^2(-C_{ta}\frac{\cos\theta}{\sin\theta} + C_n) \\ C_{t,BEM}' &= \frac{Bc}{R}\frac{1}{2\pi}(\frac{V_{rel}'}{V_e})^2(-C_{ta}\frac{\cos\theta}{\sin\theta} + C_n) \end{aligned} \tag{2.28}$$

2.6.1.5 *Actuator cylinder (AC) model*

The AC model is essentially a combination of the AC approximation of the rotor with the momentum model of the flow. The approach followed to calculate thrust on the AC is the blade-element theory, which calculates the blade forces using the velocity values from the flow field. However, the flow field can be modelled with unsteady components making this an unsteady model. The methodology employed in the 2D AC model is briefly discussed in the following part.

The induced velocities in X (along the flow direction) and Y (lateral to the flow direction) are obtained by assuming unsteady components (as shown in Equation 2.29

and solving the 2D, steady, incompressible continuity and Euler equations. The terms u_x and u_y are the velocity perturbation terms.

$$\begin{aligned} V_x &= (1+u_x)V_\infty \\ V_y &= u_y V_\infty \end{aligned} \tag{2.29}$$

The Euler equations are based on mass, momentum and energy balance in the flow. The mass continuity equations for an incompressible fluid is given by Equation 2.30. The momentum balance equations are given by Equation 2.31. The volume force exerted by the actuator surface on the flow is represented by $\vec{f}$, the pressure is given by p and the term $\frac{D}{Dt}$ represents the material derivative.

$$\nabla \cdot \vec{V} = 0 \tag{2.30}$$

$$\frac{D\vec{V}}{Dt} = \nabla(\frac{p}{\rho}) + \frac{\vec{f}}{\rho} \tag{2.31}$$

Substituting the velocity in X and Y directions in the above equations gives Equation 2.32. It can be noted that this substitution gives non-linear terms that are replaced by second-order force terms g_x and g_y respectively. Further differentiating the continuity equation with respect to x, and the X and Y - direction Euler equations with x and y respectively we get Equation 2.33

$$\begin{aligned} &\frac{du_x}{dx} + \frac{du_y}{dy} = 0 \\ &\frac{du_x}{dx} = -\frac{dp}{dx}\frac{1}{\rho V_\infty^2} + \frac{f_x}{\rho V_\infty^2} - u_x\frac{du_x}{dx} - u_y\frac{du_x}{dy} \\ &\frac{du_y}{dy} = -\frac{dp}{dy}\frac{1}{\rho V_\infty^2} + \frac{f_y}{\rho V_\infty^2} - u_x\frac{du_y}{dx} - u_y\frac{du_y}{dy} \end{aligned} \tag{2.32}$$

$$\frac{d^2p}{dx^2} + \frac{d^2p}{dy^2} = (\frac{df_x}{dx} + \frac{df_y}{dy}) + (\frac{dg_x}{dx} + \frac{dg_y}{dy}) \tag{2.33}$$

Equation 2.33 can be simplified to the Laplacian equation by ignoring the non-linear terms g_x and g_y. Since solving the non-linear equation can be computationally expensive, codes like the Horizontal Axis Wind turbine simulation Code 2nd generation (HAWC2) model for VAWT uses the linear solution of the AC model and corrects the error occurring from this assumption of linearity. This is generally referred to as a modified linear (Mod-Lin) solution Madsen et al. (2013).

The volume force ($\vec{f}$) is specified by the tangential (F_t) and normal (F_n) forces on the rotor as shown in Figure 2.15. The expressions for these averaged, non-dimensionalized blade loadings are given by Equation 2.34 and Equation 2.35.

$$Q_n(\theta) = -\frac{BF_n(\theta)}{2\pi R\rho V_\infty^2} \tag{2.34}$$

$$Q_t(\theta) = -\frac{BF_t(\theta)}{2\pi R\rho V_\infty^2} \tag{2.35}$$

The solution to the Laplacian equation obtained by ignoring the non-linear terms is given by the Greens function. The corrections in the HAWC2 model also give different expressions for analysis inside the AC and for the wake behind the AC.

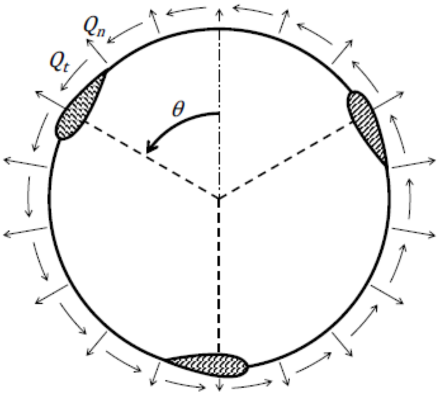

Figure 2.15: Actuator cylinder (AC) model.(De Tavernier, 2021)

2.6.2 Vortex models

The vortex models are kinematic models that use a vorticity-velocity Lagrangian approach to model the flow field. They are extensively used in the industry as an intermediate method between the momentum and CFD models. Potential flow conditions are assumed for the flow field implying incompressible, irrotational, inviscid fluid with no friction with the airfoil surface. As a result, the velocity can be expressed as the gradient of a potential field. The rotor can be modelled in 3D in its original form, discretized into several panels along the span and chord (panel method or lifting surface method), or as an actuator line (lifting line theory). Usage of a 2D model of the rotor is also found in the literature, in which case, the vortex filament is infinitely long and is represented by a point vortex in the 2D plane. Further, the vortex model takes into account the vortices convected in the wake, indicating that the model needs to be solved in time. This makes it an unsteady model.

The basis of this model takes root in the Kutta-Joukowski theorem, which states that an airfoil generating lift has a bound circulation (Γ), attached to the airfoil, generating the lift forces. Mathematically this can be expressed as shown in Equation 2.36. According to Helmholtz's vortex laws (Paraschivoiu, 2002) for potential flow, a vortex filament cannot begin or end in a fluid, implying that any occurrence of the vortex always takes the form of a closed loop. A consequence of this is the start-up and tip vortices as shown in Figure 2.16.

Additionally, Kelvin's circulation theorem states that the total circulation along a closed loop, in potential flow conditions does not vary with time. This is mathematically expressed in Equation 2.37 implying that every instantaneous change in the lift of the airfoil, sheds a vortex of equivalent strength corresponding to the change, that convects with the local wake velocity.

$$L = \rho V_\infty \Gamma \tag{2.36}$$

$$\frac{D\Gamma}{Dt} = 0 \tag{2.37}$$

The vortex, physically, is a swirling mass of air generated by a sudden difference in pressure that is created as the air flows past the airfoil. This vortex induces a velocity in the flow field as it convects with the wake. The velocity $d\vec{V}$, induced by a vortex filament of length $\vec{dl}$ and strength Γ, at a radial distance of $\vec{r}$ from the vortex filament is given by Biot-Savart's law as shown in Figure 2.17. This can be expressed mathematically as shown in Equation 2.38. Physically it means that every vortex filament creates induced velocities at every other point in the flow field. This can be a large computational expense when modelling the flow. Based on

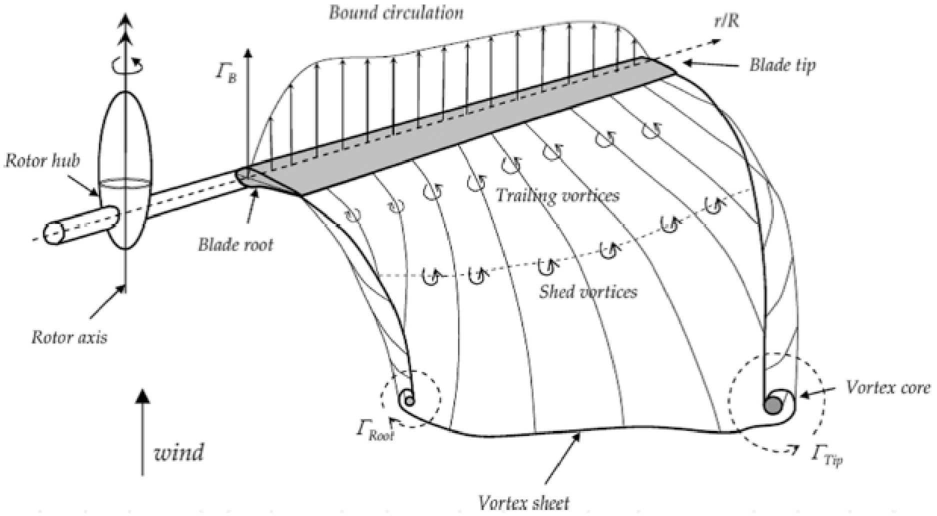

Figure 2.16: The vortex sheet formed by a rotation wind turbine blade (Micallef and Sant, 2016).

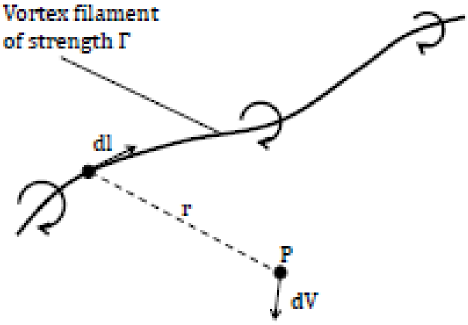

Figure 2.17: The induced velocity by a vortex filament (De Tavernier, 2021).

whether the vortices interact with each other on not, the vortex modelling method can be divided into two types; the free-wake method and the fixed-wake method. In the free-wake method, all the vortices contribute to each others' velocity fields as they convect with the wake. Whereas in the fixed-wake method, all the vortices contribute to the flow velocity only at the airfoil surface, meaning that the mutual interactions between the vortices are ignored (Katz and Plotkin, 2001).

$$d\vec{V} = \frac{\Gamma}{4\pi} \frac{\vec{dl} \times \vec{r}}{|\vec{r}^3|} \tag{2.38}$$

Vortex models were first introduced to VAWT modelling by Strickland et al. (1979). From their inception, the vortex models have advanced well to provide corrections to include the dynamic and viscous effects. An example for the vortex model is the Unsteady Two-Dimensional Vorticity Aerodynamics (U2DiVA), first introduced by Ferreira (2009). Another commonly used vortex model is The Code for Axial and Cross-flow TUrbine Simulation (CACTUS), introduced by Murray and Barone (2011).

2.6.3 Computational fluid dynamics (CFD) models

The computationally expensive, high-fidelity modelling of the flow and rotor is done by the CFD models. These models numerically solve the equations for mass continuity, momentum and energy balance in time and space. These models are Eulerian models, meaning that the analysis is made on a fixed reference frame that does not move with the fluid. While the fluid can be modelled as viscous, compressible and rotational, it is computationally expensive, as the equations are non-linear and cannot be analytically solved. For the operations of VAWT, where flow velocities are well below Mach 0.3, fluid can be considered as incompressible (Batchelor, 2000). The rotor can be modelled in its original form or can be approximated by either AD, ALM or AC models.

The 3D N-S equations for mass continuity and momentum balance, for a rotational, incompressible, viscous fluid are given by Equation 2.39 and Equation 2.40 respectively. Where $i, j = 1, 2, 3$ are the indices (with repeated indices indicating summation), p is the pressure, f_{b_i} is the body force term(Coriolis, centrifugal and gravitational forces), ν is the kinematic viscosity and x_i, u_i are spatial coordinates and fluid velocities in X, Y and Z directions. When modelling the rotor with ALM, forces exerted by the blades on the flow can be included by adding the force term $-f_i/\rho$ to Equation 2.40. These blade forces can be modelled to include dynamic effects (Bachant et al., 2018).

$$\frac{\partial u_i}{\partial x_i} = 0 \tag{2.39}$$

$$\frac{\partial^2 u_i}{\partial t^2} + u_j \frac{\partial u_i}{\partial x_j} = -\frac{1}{\rho}\frac{\partial p}{\partial x_i} + \nu \frac{\partial^2 u_i}{\partial x_j \partial x_j} - \frac{f_{b_i}}{\rho} \tag{2.40}$$

Solving the differential equations require inputs in the form of boundary conditions, which are of two forms; a Dirichlet boundary condition that sets values of different variables at the boundaries, or a Neumann boundary condition that determines the flux of the mass, momentum and energy at the boundaries. A numerical solution for the N-S equations is carried out by a finite volume approach. In the finite volume method, the Eulerian space is discretized into several small volume elements within which the mass, momentum and energy are conserved. Equation 2.41 gives a general equation for this approach, where Q is the conserved quantity, V is the volume, $\vec{F}$ is the flux of the conserved quantity through the surface area of the volume element $\vec{A}$.

$$\frac{\partial}{\partial t} \iiint_V Q dV + \iint_S \vec{F} \cdot d\vec{A} = 0 \tag{2.41}$$

Broadly, the computational expense of the model depends on the number of discrete volume elements, the type of model used, the Re number and the total volume of the 3D space. The discretization of the 3D space, also known as meshing is a crucial element in CFD modelling. Smaller mesh sizes give more accurate results while increasing the total number of cells and hence the computational expenditure. So the cell size and consequently the number of cells is determined regionally based on the accuracy requirement for the area under study.

A direct numerical simulation (DNS) solves the 3D N-S equations for all spatial and temporal scales of turbulence down to the smallest Kolmogorov microscale. While this method gives the highest accuracy, the computational power required is proportional to the order of Re^3 (Pope, 2000), which is significantly high when modelling large fields. Several alternative methods are developed to reduce the computational expenditure and model the non-linear turbulence, such as Reynolds averaged Navier-Stokes (RANS), Unsteady Reynolds averaged Navier-Stokes (URANS), Large eddy simulation (LES) and Detached eddy simulation (DES). These models and the equations governing them are briefly discussed in the subsequent sub-sections.

2.6.3.1 Reynolds averaged Navier-Stokes (RANS)

In this method, introduced by Reynolds (1895), the total velocity (u_i) and pressure gradient ($p_{,i}$) components along X, Y and Z directions, are split into mean components ($\overline{u}_i, \overline{p}_{,i}$) and fluctuating components ($u'_i, p'_{,i}$) as shown in Equation 2.42. This method, commonly known as Reynolds decomposition, allows the elimination of the time or space variables when the N-S equation are averaged temporally or spatially. The averaging can be also done across repeated experimental data sets (ensemble averaging). The computational effort required for RANS model is approximately of the order $\propto Re$ (Wilcox, 2006).

$$\begin{aligned} u_i(\mathbf{x},t) &= \overline{u_i}(\mathbf{x},t) + u'_i(\mathbf{x},t) \\ \frac{\partial p(\mathbf{x},t)}{\partial x_i} &= \frac{\partial}{\partial x_i}(\overline{p}(\mathbf{x},t) + p'(\mathbf{x},t)) \end{aligned} \tag{2.42}$$

$$\begin{aligned} \overline{u}_i &= \lim_{T\to\infty} \frac{1}{T}\int_t^{t+T} u_i(\mathbf{x},t)dt \\ \overline{\frac{\partial p(\mathbf{x},t)}{\partial x_i}} &= \lim_{T\to\infty} \frac{1}{T}\int_t^{t+T} \frac{\partial p(\mathbf{x},t)}{\partial x_i}dt \end{aligned} \tag{2.43}$$

The time-averaged velocity is obtained by averaging the total velocity and pressure in time as shown in Equation 2.43. This essentially means that the time average of the fluctuating components $\overline{u'}_i, \overline{p'}_{,i} \approx 0$.

The RANS equation for the incompressible flow is obtained by substituting the velocity and pressure terms with their Reynolds decomposition components and averaging over time. Equation 2.44 gives the equation for mass conservation and Equation 2.45 gives the momentum conservation in index notation, together known as the RANS equations.

$$\frac{\partial \overline{u_i}}{\partial x_i} = 0 \tag{2.44}$$

$$\frac{\partial \overline{u_i}}{\partial t} + \overline{u_j}\frac{\partial \overline{u_i}}{\partial x_j} = -\frac{1}{\rho}\frac{\partial \overline{p}}{\partial x_i} + \frac{\partial}{\partial x_j}\left[\frac{2\mu}{\rho}\overline{S_{ij}} - \overline{u'_i u'_j}\right] + \frac{f_{bi}}{\rho} \tag{2.45}$$

The term $\overline{S_{ij}} = \frac{1}{2}(\overline{u}_{j,i} + \overline{u}_{i,j})$, represents the strain rate tensor of the fluid for in-compressible flow, which is a skew-symmetric matrix for a 3D flow. The term $-\overline{u'_i u'_j}$, representing the momentum transfer due to turbulent velocity fluctuations in Equation 2.45, is the Reynolds stress tensor. This occurs due to the non-linear nature of the governing N-S equation and highlights the closure problem of turbulence. The Boussinesq hypothesis is widely used to approximate the Reynolds stress term (Sanderse et al., 2011). In this, the Reynolds stress tensor is modelled as a viscous diffusion term by introducing turbulent eddy viscosity (ν_T), as shown in Equation 2.46 for incompressible flow. The term δ_{ij} is the Kronecker delta defined as shown in Equation 2.47 and the term k represents the turbulent kinetic energy given by $k = \overline{u'_i u'_i}/2$. It is noted that the Boussinesq hypothesis is a mere approximation and does not have a rigorous physical explanation, as the turbulent eddy dissipation is fundamentally different from the molecular viscosity (Wilcox, 2006). The Reynolds stress diffusion is significantly larger than the molecular viscous forces in the wake unless close to a solid boundary. Thus this approximation does not perform well when there is a large, sudden change in the strain rate of the flow (*e.g.* within the boundary layers of an airfoil), when the flow is anisotropic and 3D flows (Wilcox, 2006; Schmitt, 2007).

$$-\overline{u'_i u'_j} = \nu_T(\frac{\partial \overline{u}_i}{\partial x_j} + \frac{\partial \overline{u}_j}{\partial x_i}) - \frac{2}{3}k\delta_{ij} \tag{2.46}$$

$$\delta_{ij} = \begin{cases} 1, & \text{if } i = j, \\ 0, & \text{if } i \neq j. \end{cases} \tag{2.47}$$

Several closure methods are available in the literature to calculate the eddy viscosity (ν_T) in the above equation. These methods, their relevance and their accuracy are discussed in detail in Section 2.6.3.3.

2.6.3.2 *Unsteady Reynolds averaged Navier-Stokes (URANS)*

A URANS model is used when the mean flow parameters vary periodically. The time-averaging, in this case, is done over a time period that corresponds to the unsteadiness. This is especially applicable in the case of VAWTs where there is a periodic shedding of vortices from the airfoil. Alternatively the averaging can be done over a phase angle corresponding to the unsteadiness. The accuracy of this model depends largely on the computational settings; in particular, the chosen domain discretization, time step and convergence criteria (Chowdhury et al., 2016; Rezaeiha et al., 2019; He et al., 2020).

2.6.3.3 *Turbulence models for RANS and URANS*

This section presents a discussion on the models used to calculate the eddy viscosity (ν_T) and hence provide closure to the turbulence problem. Further, the turbulence model plays a pivotal role in the prediction of laminar to turbulent transition, the vortex dissipation, the wake structure and the performance prediction of VAWT. Several models are available in the literature, however, only the commonly used models are presented here. A lack of universality of the models means that a model must be carefully chosen to suit the experimental conditions. The commonly compared turbulence models in the literature for modelling VAWTs and their wakes are Spalart-Allmaras model (SA), $k-\epsilon$ model (KE), renormalization group theory $k-\epsilon$ model (RNG), realizable $k-\epsilon$ model (RKE), shear stress transport $k-\omega$ model (SST KW) and transition shear stress transport $k-\omega$ model (TSST) (Bachant and Wosnik, 2016; Lam and Peng, 2016; Chowdhury et al., 2016; Rezaeiha et al., 2019).

Spalart-Allmaras model (SA) :
The SA model is a single equation model that solves a transport equation for turbulent eddy viscosity (ν_T) and turbulent kinetic energy(k). It was first introduced by Spalart and Allmaras (1992) for wall-bounded flows. It has been noted that the model is essentially a low Re number model and does not work well for high strain rate changes. Rezaeiha et al. (2019), in their comparison, use a modified model introduced by Dacles-Mariani et al. (1995), which reduces the eddy viscosity for cells where the vorticity exceeds the strain rate. Bachant and Wosnik (2016) mentions that 3D SA with RANS performs better than SST KW with RANS in predicting turbine performance (C_p and C_t), while wake velocity profile is predicted better by SST KW when compared with the experimental results. Rezaeiha et al. (2019) and Chowdhury et al. (2016) note that SA largely deviates from experimental results even in predicting the turbine performance. The comparison made by the latter spans data sets over 3 different rotor parameters and several TSRs but the former presents a comparison for only one set of rotor parameters. The wake predicting ability of the RANS or URANS with SA model is agreed to be poor (Ferreira et al., 2007; Bachant and Wosnik, 2016; Rezaeiha et al., 2019; Peng et al., 2021)

$k-\epsilon$ models (KEs) :
The $k-\epsilon$ model (KE) (also referred to as standard KE) is a two-equation model first introduced by Launder and Sharma (1974). It uses two transport equations for turbulent kinetic energy (k) and turbulent viscous dissipation (ϵ) respectively.

Realizable $k-\epsilon$ model (RKE) (Shih et al., 1995) and Renormalization group theory $k-\epsilon$ model (RNG) (Yakhot and Orszag, 1986) were developed as improvements to the standard KE. The RKE has improvements from standard KE in modelling high streamline curvature, rotational and high vorticity flows while RNG is a statistically derived method with enhancements for high strain rates and swirling flows. Rezaeiha et al. (2019) use a wall-correction for adverse pressure gradients for both RNG and RKE methods but Balduzzi et al. (2016) use KE and RNG without wall-correction. The conclusion from the discussion mentioned in the above mentioned literature is that, the standard KE performs worse than RNG with respect to rotor performance but among RNG and RKE, neither holds superiority either in the prediction of wake structure or the rotor performance. The main error with the standard KE model seems to arise from the Boussinesq approximation that under predicts the dissipation near-wall regions at the airfoil boundary layers (Wilcox, 2006). However, the KE models are robust in freestream conditions (Balduzzi et al., 2016) making it a good choice for wake modelling.

Shear stress transport $k-\omega$ models (SST KWs) :
It was introduced by Menter (1994) and is an extension of the standard $k-\omega$ model (KW) model (Wilcox, 2006). The standard KW model is a two-equation model using the transport equations for turbulent kinetic energy (k) and specific turbulent kinetic energy dissipation rate (ω), which indicates the rate at which k dissipates into thermal energy. While the standard KW model works well for low Re flows and at the boundaries, it does not perform well in freestream conditions. In the SST KW, the wall-boundaries are handled by the Wilcox $k-\omega$ model (Wilcox, 2006) and the KE model in the freestream thus being robust and insensitive in the respective regions. Several authors (Balduzzi et al., 2016; Chowdhury et al., 2016; Bachant et al., 2018; Rezaeiha et al., 2019) agree that SST KW model has a better rotor performance prediction and wake structure prediction in comparison to KE, RKE and RNG models. An even better model (Barnes et al., 2021), improving upon Menter (1994) is the 4 equation TSST model (referred to as $\gamma - Re_{\theta t}$ model) introduced by Menter et al. (2004). This model is also a low Re number model, where intermittency equation predicts the onset and length of transition from laminar to turbulent reattachment in the separation bubble at the airfoil or wall-boundaries (Menter et al., 2002). Two additional transport equations one for momentum thickness Reynolds number ($Re_{\theta t}$) and another transport equation for intermittency (γ). This model is computationally more expensive but agrees well with the experimental results for the wake, rotor performance, prediction of the dynamic stall and the periodic vortex shedding observed in VAWTs (Rezaeiha et al., 2019). However, from the comparison shown in Figure 2.18 it can be observed that the wake profile prediction on the leeward side deviates significantly for all the models in comparison with the experimental data from Tescione et al. (2014). Rezaeiha et al. (2019) further notes that the wake expansion is underestimated by all the compared turbulence models.

2.6.3.4 Large eddy simulation (LES)

The LES model, commonly used to model turbulence, uses a filtering kernel (G) to separate the resolved velocity fields from the sub-grid scale (SGS) velocity fields. Only the largest eddies are resolved and the effect of the velocities on the large-scale resolved flow fields is done by the SGS model. The filter itself is a convoluted integral as shown in Equation 2.48, which can be a volume-averaged box filter or a Gaussian filter. The term $\overline{u}$ is the resolvable-scale filtered velocity, u is the SGS velocity and $\boldsymbol{\Delta}$ is the filtering width. Equation 2.49 gives the SGS velocity u_i'. While Equation 2.49 resembles Equation 2.42, the main difference is that $\overline{\overline{u}}_i \neq \overline{u}_i$ implying that $\overline{u'}_i \neq 0$ (Wilcox, 2006).

$$\overline{u}_i(\mathbf{x},t) = \iiint u_i(\boldsymbol{\xi},t)G(\mathbf{x}-\boldsymbol{\xi},\boldsymbol{\Delta})d^3\boldsymbol{\xi} \tag{2.48}$$

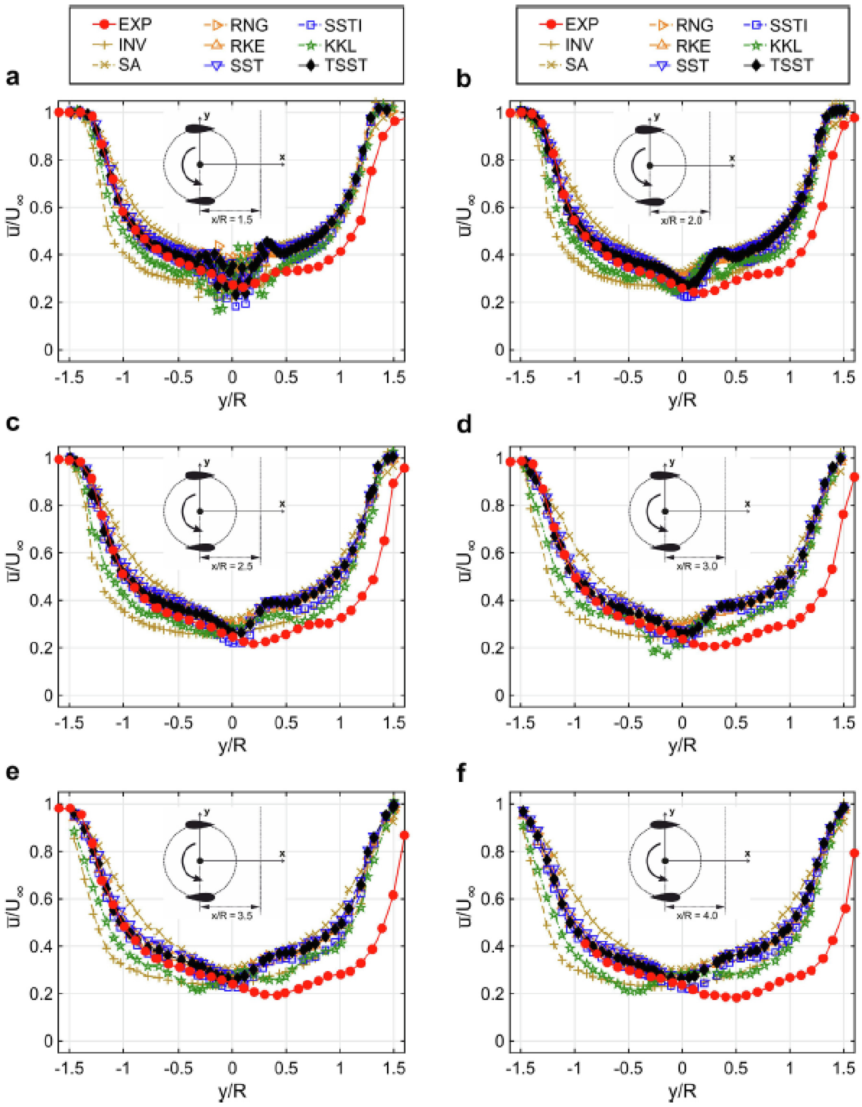

Figure 2.18: Comparison of performance of different turbulence models (Spalart-Allmaras model (SA), renormalization group theory $k-\epsilon$ model (RNG), realizable $k-\epsilon$ model (RKE), shear stress transport $k-\omega$ model (SST KW) and transition shear stress transport $k-\omega$ model (TSST)) in capturing the near-wake profile (Rezaeiha et al., 2019)

$$u_i'(\mathbf{x},t) = u_i(\mathbf{x},t) - \overline{u_i}(\mathbf{x},t) \tag{2.49}$$

The implementation of this filtering in the RANS or URANS equations gives the LES N-S equation shown in Equation 2.50, where $\overline{\tau}_{ij} = \overline{u}_i\overline{u}_j - \overline{u_i'u_j'}$ represents the SGS stress tensor. This equation when implemented along with the Boussinesq hypothesis gives Equation 2.51. This was first introduced by Smagorinsky (1963) to model large scale atmospheric eddies. The use of the Boussinesq hypothesis, however, gives similar limitations as that of RANS model.

$$\frac{\partial^2\overline{u_i}}{\partial t^2} + \overline{u_j}\frac{\partial\overline{u_i}}{\partial x_j} = -\frac{1}{\rho}\frac{\partial\overline{p}}{\partial x_i} + \frac{\partial}{\partial x_j}\frac{2\mu}{\rho}\overline{S_{ij}} + \frac{\partial\overline{\tau}_{ij}}{\partial x_j} \tag{2.50}$$

$$\frac{\partial^2\overline{u_i}}{\partial t^2} + \overline{u_j}\frac{\partial\overline{u_i}}{\partial x_j} = -\frac{1}{\rho}\frac{\partial\overline{p}}{\partial x_i} + \frac{\partial}{\partial x_j}\left([\nu+\nu_T]\frac{\partial\overline{u_i}}{\partial x_j}\right) \tag{2.51}$$

The computational expenditure of the LES model, which is, approximately $\propto Re^2$, although less than that of DNS method, is still computationally expensive at locations within the surface boundary layer. To reduce this a hybrid RANS/LES model, commonly referred to as detached eddy simulation (DES) model, is used, where the less expensive RANS is used within the boundary layers (Sanderse et al., 2011).

2.7 MODEL COMPARISON STUDY

This section presents a detailed comparison of different models discussed in the previous sections. The literature available for the performance of VAWT models in comparison with the experimental data is reviewed. A comparison of these different models is made based on the following parameters:

- Computational expenditure
- Accuracy in rotor performance (C_p and C_t) and blade loading prediction.
- Accuracy in wake structure prediction (u_i)
- Accuracy in the prediction of dynamic effects (instantaneous blade loading, vortex shedding and blade-vortex interactions)

At the outset, a broad comparison between the 2D and 3D models is presented. Further comparison is made separately for each of the three major categories of VAWT modelling which are :

- Rotor modelling
- Flow modelling
- Turbulence modelling

While turbulence modelling is a part of the CFD flow modelling technique, it plays an important role in predicting the wake structure and performance of the turbine (Chowdhury et al., 2016; Rezaeiha et al., 2019). For this reason, a comparison is included separately. The models that perform best in each modelling category given the constraint of the computational expenditure are selected in combination, to carry out the simulations.

2.7.1 2D and 3D model comparisons

All the rotor and flow modelling methods can be implemented either in 2D or in 3D. While 2D models have an edge over 3D models in computational expenditure, they do not capture the effect of tip vortices that are significant in VAWTs. Ferreira et al. (2010) shows that the tip vortex is the largest component of trailing vorticity. With regards to predicting the turbine performance, it has been noted that 2D models over-predict the blade loading and do not account for vertical momentum transport (Bachant and Wosnik, 2016). However, the 2D models are useful to obtain accurate results for the mid-span section of blades with large span lengths (Ferreira et al., 2007). A study by Tavernier et al. (2020) shows that, only for aspect ratios above 5, the power loss due to tip vorticity can remain below 1%. For lower aspect ratios, the power loss can be as high as 15%. Since the experiment is conducted for a small VAWT with an aspect ratio of 1 (Huang et al., 2020) and the wake profile generated by the simulation needs to co-relate with experimental results, the 3D model is chosen for further comparison.

2.7.2 Rotor model comparisons

In this section, the simplified rotor models, *i.e.* actuator disk (AD), actuator cylinder (AC) and actuator line model (ALM), are compared with each other and with the rotor modelled in its original dimensions. While the actual rotor model gives the most accurate results, resolving the boundary layer formations around the rotor is computationally expensive.

The AD model, which is the most simplified model, is inappropriate for a VAWT rotor that sweeps a cylindrical surface. However, it has been extensively used with several corrections as its computational expenditure is the least among others. The DMST model approximated with two ADs, which incorporates different induction factors and thrust coefficients for the upwind and downwind halves, predicts the blade loading and rotor performance better than single AD models. However, it is noted that the iterative solution fails to converge for heavily loaded rotors, with higher TSRs and solidity (McIntosh et al., 2009). Beri et al. show that for lower TSRs the AD model in DMST flow assumptions predicts a negative power coefficient which contradicts the CFD simulation results. Further AD model also fails to predict the wake structure as the solution is essentially steady in nature and formed by an AD (Bachant and Wosnik, 2015). While dynamic stall has been implemented using adaptations of Gormont model, the MIT model (Paraschivoiu and Allet, 1988) and Indicial model (Proulx and Paraschivoiu, 1989) with the AD rotor approximation by several authors in the past (Strickland et al., 1979; Massé, 1981; Berg, 1983; Paraschivoiu et al., 1988; Masson et al., 1998), the unsteady effects such as vortex shedding and blade-vortex interactions, which are dominant phenomena leading to deep dynamic-stall, are not captured with this rotor model.

The AC model, on the other hand, is better equipped to handle the varying induction at different azimuthal angles but suffers the limitations created by the assumption of an infinite number of blades and steady flow. Computationally, this rotor model is inexpensive even when combined with the CFD flow models. The AC model predicts the averaged blade loading well in comparison with ALM (De Tavernier et al., 2020; Ferreira et al., 2014), but cannot capture the instantaneous blade loading well (Hand et al., 2015). While the unsteady effects still cannot be accurately modelled with this rotor model, Tavernier et al. shows that the tip-effects can be captured with the 3D AC rothe tor model when combined with CFD flow model. Hand et al. notes that there is a dearth in the literature comparing the accuracy of the AC model with the experimental results. A study by Shamsoddin and Porté-Agel shows that, with the LES CFD flow model, the ALM fares much better than the AC model in comparison with experimental results.

The ALM is the closest rotor model, to the actual rotor. Since modelling the actual rotor and numerically resolving the flow around the boundary layers is computationally expensive, the ALM uses the blade-element theory or lifting line theory, in combination with a dynamic stall model to calculate the blade forces, giving a higher accuracy in the prediction of instantaneous blade loading. This model has been validated against the experimental results to study the wake and has shown a good agreement when the flow is modelled using high-fidelity, CFD flow models (Sørensen et al., 2015; Bachant and Wosnik, 2016; Mendoza et al., 2019). The ALM model, however, predicts increased blade loading at the tips for which end corrections need to be applied. De Tavernier et al. notes that this correction is physically difficult to justify. Given the available computational resources and the required level of accuracy of the wake structure, this rotor model is chosen for further evaluation. Table 2.2 gives an overview of the above discussion.

Rotor Model	Computational expenditure	Rotor performance	Wake structure	Dynamic effects
AD model	Low	Medium	Low	Low
AC model	Low	Medium	Medium	Low
ALM	Medium	High	High	High
Actual rotor	High	High	High	High

Table 2.2: Evaluation of the rotor models against the performance parameters.

2.7.3 Flow model comparisons

Generally in the available literature, the flow models are often evaluated in tandem with the rotor models. In this study, however, a distinction is made to understand the advantages and disadvantages of all possible combinations of rotor and flow models with relevance to the study of the wake.

Although the momentum models are computationally inexpensive and predict the averaged blade loading well for lightly loaded rotors (Paraschivoiu, 2002; McIntosh et al., 2009), they do not predict the instantaneous blade loading well (Hand et al., 2015). Although these models are fundamentally steady-state models, they have been extended to include effects of wake expansion (Read and Sharpe, 1980) and flow curvature effects (Muraca et al., 1975). The assumption of streamwise independence of stream tubes in the MST and DMST models leads to erroneous results, as there is always mass and momentum transfer from one stream tube to another. The assumption of a fully developed wake leads to overestimating the power generated in the downwind half (Ferreira, 2009). Further, these models cannot predict wake structures and wake velocities very well. Since the DMST is the most advanced of the stream tube models it is chosen for further comparison.

The vortex models provide better turbine performance predictions than the momentum models as they take into account the effect of the wake on the blade loading (Strickland et al., 1979). Computationally the free-wake method is more expensive and has a better performance than the fixed-wake method. The effects of flow curvature and dynamic stall can also be incorporated, leading to better prediction of instantaneous blade loading, power coefficient and near-wake velocities (Borg et al., 2014). However, it is noted that the power generated and the instantaneous blade loading are decoupled (Ferreira and Scheurich, 2011), implying that, validation using averaged power coefficient curves does not necessarily mean a validation of the instantaneous blade loading. A comparison of performance of different models by De Tavernier et al. show that, the near-wake correction for the CACTUS leads to the erroneous blade loads at the tips, which is in line with the observations of Ferreira et al.. With regard to the wake structure prediction, the free-wake method performs better than the fixed-wake method. However, the potential flow assumptions limit the accurate prediction of wake velocities despite the implementation of empirically derived viscous models.

Among the CFD flow models, the DNS model is clearly superior to others at the expense of incredibly high computational resources (Pope, 2000). The CFD models in the decreasing order of computational expense and accuracy would be LES, DES, URANS and RANS. However, the accuracy of URANS depends on simulation settings as noted in Section 2.6.3.2, hence a separate study is carried out to evaluate the effects of simulation settings. Several authors (Bachant and Wosnik, 2016; Lam and Peng, 2016; Rezaeiha et al., 2019; Mendoza et al., 2019) have validated the performance of CFD flow models in predicting the wake structure and state that the results compare with the experiments with acceptable levels of accuracy. Further, for TSRs below 4, Laneville and Vittecoq have shown the occurrence of deep dynamic stall

Flow Model	**Computational expenditure**	**Rotor performance**	**Wake structure**	**Dynamic effects**
DMST model	Low	Medium	Low	Low
Fixed-wake vortex model	Low	Medium	Medium	Medium
Free-wake vortex model	Medium	High	Medium	High
URANS model	Medium	High	High	High
RANS model	Medium	High	High	High
DES model	High	High	High	High
LES model	High	High	Very high	Very high
DNS model	Very high	Very high	Very high	Very high

Table 2.3: Evaluation of the flow models against the performance parameters.

which makes the CFD flow model appropriate for the current case, where the operating TSR is 2.5. Considering the emphasis on the wake structure prediction, the unsteady nature of VAWT wakes and available computational resources, the CFD URANS model is chosen for the study. Table 2.3 gives a complete overview of the compared models.

2.7.3.1 Turbulence model comparisons

In this subsection, a brief comparison of the different turbulence models (SA, KE, KW, RNG, RKE, SST KW and TSST) is provided based on the literature study presented in Section 2.6.3.3. Table 2.4 gives an overview of the performance of the turbulence models against the evaluating parameters.

While several authors agree that the best performing turbulence model, in the prediction of wake and the rotor performance parameters, is the TSST model with URANS (Barnes et al., 2021; Rezaeiha et al., 2019; Chowdhury et al., 2016), the KE model is used as the baseline turbulence model for this study. The reason for this is threefold; firstly, the URANS ALM model used in this study, does not require the resolution of the boundary layer at the airfoil surface, as the blade forces are determined separately by a combination of blade-element theory and a dynamic stall model. Secondly, it has been shown that the standard KE model has a good performance in freestream regions which makes it appropriate for wake study (Balduzzi et al., 2016). Finally, the simplicity of implementation of this turbulence model makes it a good fit for its use as the baseline model for further comparison. However, a brief study is carried out in Chapter 3 to assess the impact of the turbulence model and its parameters on the wake.

Turbulence Model	**Computational expenditure**	**Rotor performance**	**Wake structure**	**Dynamic effects**
SA model	Low	Low	Low	Low
KE model	Low	Medium	High	High
KW model	Low	High	Medium	High
RNG model	Medium	High	High	High
RKE model	Medium	High	High	High
SST KW model	High	High	Very high	Very high
TSST model	High	High	Very high	Very high

Table 2.4: Evaluation of the turbulence models against the performance parameters.

3 METHODOLOGY AND APPROACH

This chapter elaborates on the methodology and approach followed in the implementation of an actuator line model (ALM) in Open-source Field Operation And Manipulation (OpenFOAM) using the turbinesFoam library. At the outset, the general working of OpenFOAM and turbinesFoam is studied. Then the case of ALM with the unsteady Reynolds averaged Navier-Stokes (URANS) flow model is set up. Subsequently, the turbine geometry and the operational parameters are defined using the same conditions as that of the experiment carried out. In the next step, the domain, mesh topology and the time step settings is defined. For the case of a vertical-axis wind turbine (VAWT), the corrections for flow curvature, dynamic loading, added mass and tip effects need to be included. These corrections are implemented in the simulations using the turbinesFoam module. The wake of the VAWT, at the start of the simulation, is not fully developed. To evaluate the time taken by the wake to reach a steady-state, a convergence study is conducted by observing the turbine power coefficient, wake velocity at a fixed point in the domain and the residuals of the simulation. From this evaluation, the averaging period for the URANS case is determined. Since the accuracy of the results in URANS flow model, depends on the simulation parameters (*i.e.* spatial and temporal discretization), a study is carried out to evaluate the sensitivity of the simulation results to these parameters. The results of this study provide the basis for the choice of mesh topology and the time marching interval selected. Ultimately, the data is sampled at different locations for further study.

In Section 3.1, the OpenFOAM library, turbinesFoam library and the options/settings it presents are briefly discussed. Section 3.2 presents a discussion on these various correction models that are selected in line with the literature study. The geometry of the turbine and its components along with the operational parameters are presented in Section 3.3. The simulation parameters are then presented in Section 3.4. The study carried out to evaluate the convergence of the simulation is discussed in Section 3.5. Further, the sensitivity of the simulation results to the spatial and temporal discretization is presented in Section 3.6. Finally, Section 3.7 provides the details of the experimental setup, whose results are used for the validation of this model.

3.1 OPENFOAM AND TURBINESFOAM LIBRARY

OpenFOAM is an open-source C++ library used to solve problems pertaining to continuum mechanics and create utilities for field data sampling (Puig and Gamez, 2014). In the current case, this library is utilised to numerically solve the 3 dimensional (3D) Navier-Stokes (N-S) equation governing fluid flow. Figure 3.1 provides the operational structure of OpenFOAM. The pre-processing environment provides options and tools for generating the mesh and the domain. The pimpleFoam solver used in the simulations employs a finite volume approach to temporally and spatially solve the N-S equation numerically. The turbinesFoam library is an addendum to the solver which allows the user to set and define the turbine components (*i.e.* blades, tower, struts and shaft) and their associated parameters (*e.g.* rotor diameter, chord length, blade and strut pitch angles *etc.*). It also provides options to include the unsteady effects like the dynamic stall, flow curvature, added mass models and

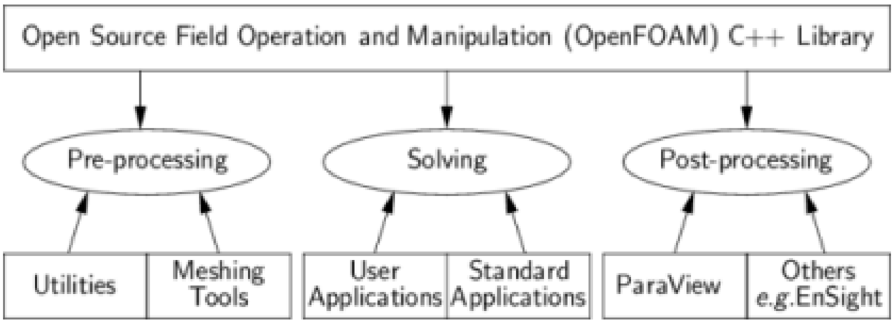

Figure 3.1: Overview of OpenFOAM structure. (Puig and Gamez, 2014)

define their respective parameters. Created by Bachant et al. (2019) to bridge the gap between low and high fidelity computational fluid dynamics (CFD) modelling, the turbinesFoam is relevant to the current study, since it has been extensively used to model VAWTs. This is included under the fvOptions file in OpenFOAM and used by turbineALSource files to set the general turbine parameters. The crossFlowTurbineALSource creates the actuator line elements and their corresponding rotation matrices. The post-processing environment provides options to obtain required data and visualize the solutions.

3.2 ALM AND CORRECTION MODELS

This section presents the working of the ALM in OpenFOAM and various additions to model the unsteady effects with corrections. The ALM combines the blade-element theory with the N-S representation of the flow (whose momentum equation is given by Equation 3.2 with the additional equation for mass continuity). The blades, tower, shaft and struts are replaced by lines or actuator line elements at the quarter-chord locations. The inflow velocity is given by the linearly weighted interpolation provided by OpenFOAM's interpolationCellPoint class. The forces on the blades and struts are calculated using the standard lift and drag equations shown in Equation 3.1. The relative velocity is calculated by taking the vectorial sum of inflow velocity and blade velocity. The static lift and drag coefficients for the blades and struts are taken from the database provided by Sheldahl and Klimas (1981) and interpolated for the operating Re_c. The tower is further modelled as a cylinder with a lift coefficient of $C_l = 0$ and a drag coefficient of $C_d = 1.1$. The tower does not rotate, implying that the Magnus effect caused due to the rotation of the tower is neglected.

$$\begin{aligned} L &= \frac{1}{2}\rho A_{elem} C_l V_{rel}^2 \\ D &= \frac{1}{2}\rho A_{elem} C_d V_{rel}^2 \end{aligned} \tag{3.1}$$

$$\frac{\partial^2 u_i}{\partial t^2} + u_j \frac{\partial u_i}{\partial x_j} = -\frac{1}{\rho}\frac{\partial p}{\partial x_i} + \nu \frac{\partial^2 u_i}{\partial x_j \partial x_j} - \frac{f_{bi}}{\rho} \tag{3.2}$$

The calculated lift and drag forces from each of the above-mentioned actuator line elements are then used in the flow description as source terms. However, these forces need to be smeared across the element locations to prevent the occurrence of instability arising from steep force gradients. This is done with the use of a spherical Gaussian function (η) as shown in Equation 3.3, where ϵ controls the width and $|\vec{r}|$ is the distance from the actuator element to the cell on which the force is smeared. The smoothing width parameter ϵ is chosen as the maximum value among quarter chord length ($c/4$), momentum thickness of drag forces ($cC_d/2$) and the mesh size ($4V_{cell}^{1/3}$). V_{cell} represents the cell volume of the chosen cell (Bachant et al., 2016; Mendoza et al., 2019). A consequence of the force smearing is that the vortex core at the tips may be lost, necessitating a need for tip corrections.

$$\eta = \frac{1}{\epsilon^3 \pi^{3/2}} exp\left[- \left(\frac{|\vec{r}|}{\epsilon} \right)^2 \right] \tag{3.3}$$

3.2.1 Dynamic stall model

The tip speed ratio (TSR) of operation in the current study is 2.5. Following the discussion in Section 2.3.1, the dynamic stall effects are severe at low TSRs. The Beddoes-Leishman (B-L)-Sheng-Galbraith-Coton (SGC) model of dynamic stall is implemented with the help of the turbinesFoam library. The SGC model is a modified B-L dynamic stall model with corrections for low Mach numbers proposed by Sheng et al. (2008). Prior to the execution of dynamic stall in OpenFOAM the static polar data for the calculated operating Re_c is interpolated. After this, the static stall angle, separation point curve fit parameters and the zero-lift drag coefficients are computed for every time step to include the effect of operating Re_c number. A further study is carried out to analyse the effect of the dynamic stall model on the wake and the results of this study are presented in Chapter 4.

3.2.2 Tip correction

The blade, experiencing lift force has a bound circulation around it which ends at the tip of the blade. Helmholtz's second vortex theorem which states that the vorticity exists only in closed loops mandates the existence of tip vortices. This is normally predicted by the solver when the blade is modelled in its original form. However, since the blade is being modelled as an actuator line with the smeared blade forces, a tip correction needs to be implemented to correct the tip loading. The correction used in this model follows the implementation by Bachant et al. (2016), which uses Prandtl's lifting line theory. The geometric angle of attack (AOA) is expressed as a function of non-dimensionalized span (ζ) given by Equation 3.4, where, H is the span length, N is the number of chord elements and A_n are the Fourier coefficients to be calculated.

$$\alpha(\zeta) = \frac{2H}{\pi c(\zeta)} \sum_{1}^{N} A_n sin(\zeta) + \sum_{1}^{N} n A_n \frac{sin(n\zeta)}{sin(\zeta)} + \alpha_{L=0}(\zeta) \tag{3.4}$$

The circulation distribution is then calculated using Equation 3.5 and the spanwise lift coefficient ($C_l(\zeta)$) is found using the Kutta-Joukowski theorem. The final correction function (f) is then calculated using Equation 3.6.

$$\Gamma(\zeta) = 2HU_\infty \sum_{1}^{N} A_n sin(n\zeta) \tag{3.5}$$

$$f = \frac{C_l(\zeta)}{C_{lmax}(\zeta)} \tag{3.6}$$

3.2.3 Added mass

The effect of added mass occurs from the step changes in AOA during the implementation of dynamic stall. The model implemented in this study is provided by Strickland et al. (1979). The force required to accelerate the fluid around the airfoil is provided by the normal force exerted by the airfoil, thus leading to the increased loading on the airfoil. The normal ($C_{n_{AM}}$) and chordwise ($C_{c_{AM}}$) force coefficients as a result of added mass are calculated as per Equation 3.7. The moment coefficient ($C_{m_{AM}}$) about the aerodynamic centre is calculated as shown in Equation 3.8. The sign convention followed here takes the trailing edge to the leading edge as the positive direction for the forces and the nose-up moment as positive. The translation of normal and chordwise force coefficients to lift ($C_{l_{AM}}$) and drag ($C_{d_{AM}}$) coefficients is given by Equation 3.9. The $\dot{x}$ represents the time derivative of the quantity x, the V_n and V_c are the normal and the chordwise components of relative velocity (V_{rel}).

$$\begin{aligned} C_{n_{AM}} &= -\frac{\pi c \dot{V}_n}{8V_{rel}^2} \\ C_{c_{AM}} &= \frac{\pi c \dot{\alpha} V_n}{8V_{rel}^2} \end{aligned} \tag{3.7}$$

$$C_{m_{AM}} = -\frac{C_{n_{AM}}}{4} - \frac{V_n V_c}{8V_{rel}^2} \tag{3.8}$$

$$\begin{aligned} C_{l_{AM}} &= C_{n_{AM}} cos(\psi) + C_{c_{AM}} sin(\psi) \\ C_{d_{AM}} &= C_{n_{AM}} sin(\psi) - C_{c_{AM}} cos(\psi) \end{aligned} \tag{3.9}$$

3.2.4 Flow curvature

The effect of flow curvature caused by the rotation (as discussed in Section 2.3.2) is modelled using the technique developed by Goude (2012). In this model, a flat plate rotating in potential flow assumptions are considered to determine the AOA as a function of chord length (c). The expression is given by Equation 3.10; where V_{abs} is the absolute velocity obtained from the gradient of the complex conjugate of the complex velocity potential, V_{ref} is the reference velocity obtained from the reference case of the static wing, x_{0r} is the fractional distance of the point of calculation to the quarter chord, β is the blade pitch angle, θ is the azimuthal angle of the blade, ψ is the inflow angle and Ω the magnitude of angular velocity.

$$\alpha = \beta + tan^{-1}\left[\frac{V_{abs} cos(\theta - \psi)}{V_{abs} sin(\theta - \psi) + \Omega R}\right] - \frac{\Omega x_{0r} c}{V_{ref}} - \frac{\Omega c}{4V_{ref}} \tag{3.10}$$

The ALM, as Bachant et al. notes, calculates the first two terms automatically. The last two scalar terms are added separately in the code. This is again implemented as an option present in the fvOptions whilst using the turbinesFoam library.

3.2.5 Turbulence model

The implementation of the turbulence model is provided by an object called RASproperties in the dictionary. Following the discussion on the turbulence models in Section 2.6.3.3 and the subsequent comparison in Section 2.7.3.1, the standard $k - \epsilon$ model (KE) model is used as the baseline turbulence model. The equation to calculate the turbulent kinetic energy (k) at the inlet is given by Equation 3.11 and subsequently, Equation 3.12 gives the equation to calculate the value of turbulent dissipation (ϵ). The term l is the length scale of the turbulent eddies and $C_\mu = 0.09$ (Launder and Spalding, 1974). The largest eddies at the inlet are of the length scales of the mesh rod/bar sizes at the inlet of the wind tunnel (Roach, 1987) and the turbulent dissipation is mainly affected by the largest eddies (Katopodes, 2019). Hence the length scale of the turbulent eddies is selected after a sensitivity study. The sensitivity of the standard KE turbulence model to different inlet turbulence intensity and turbulent dissipation values is evaluated in Chapter 4.

$$k = \frac{3}{2}\left(IV_\infty\right)^2 \tag{3.11}$$

$$\epsilon = \frac{C_\mu k^{1.5}}{l} \tag{3.12}$$

3.3 TURBINE GEOMETRY AND OPERATIONAL PARAMETERS

In this section, the turbine geometry and the operational parameters used in the simulations are presented. To begin with, it is important to present the sign convention used here on. The general sign convention followed for the spatial coordinate system is freestream wind direction taken as positive X direction positive Y along the leeward side and vertically upwards as the positive Z direction. The turbine rotates clockwise with its centre located at the origin $[0, 0, 0]$ and azimuth angle (θ) is measured from the windward direction ($-Y$ direction) with the clockwise direction as positive. The zones are defined as windward side for $\theta \in (-45°, +45°)$, upwind side for $\theta \in (45°, 135°)$, leeward side for $\theta \in (135°, 225°)$ and downwind side for $\theta \in (225°, 315°)$. This is represented pictorially in Figure 3.2a. The direction of thrust force on the turbine is along positive X direction and the normal force is positive when it is facing inwards as shown in Figure 2.3. It is to be noted that this sign convention for θ is opposite to the sign convention presented in the literature review mainly because the simulation uses a clockwise rotating turbine. It is also to be noted that the axis of rotation is pointing along $-Z$.

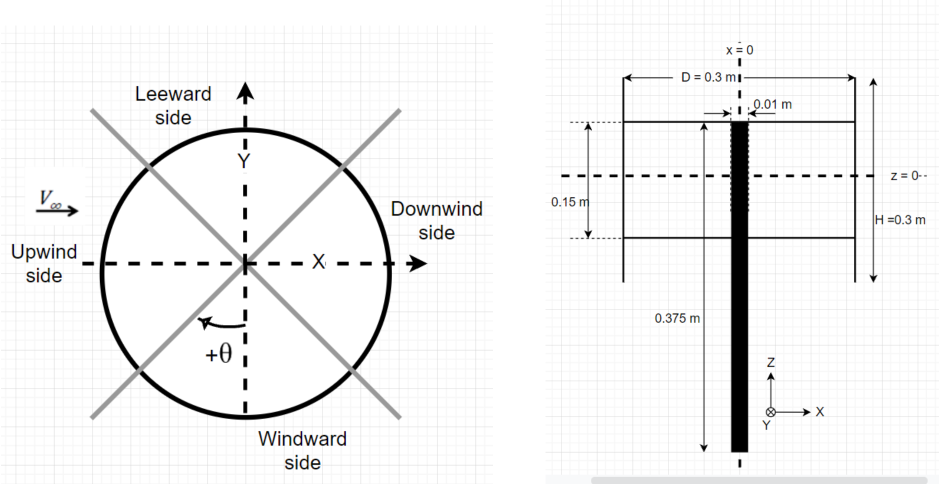

(a) Sign conventions.

(b) Turbine dimensions.

Figure 3.2: A pictorial description of the sign conventions, the turbine zones and parameters.

Operational Parameter	Value
Inflow velocity (V_∞)	$5ms^{-1}$
Tip speed ratio (TSR)	2.5
Turbulence intensity (I)	0.5%
Chord Reynolds number (Re_c)	1.5×10^5
Rotor Reynolds number (Re_r)	1.5×10^6

Table 3.1: The operational parameters for the simulation.

A straight-bladed H-rotor, with 2 blades and 4 struts of NACA0012 profile along with a tower is modelled for the simulations. Figure 3.2b shows a pictorial representation of the turbine. Table 3.2 gives the geometric parameters of the turbine and Table 3.1, its operational parameters for the baseline simulation case. The static lift and drag coefficient for NACA0012 airfoil at $Re_c = 2 \times 10^4$ is taken from the database provided by Sheldahl and Klimas (1981). The tower is modelled as a cylinder with zero lift coefficient and a drag coefficient of 1.1. The time period of rotation of the turbine is $0.07539s$.

Turbine geometry	Dimensions
Rotor diameter (D)	0.3 m
Blade/strut chord length (c)	0.03 m
Strut span (s_s)	0.145 m
Rotor height/blade span (H)	0.3 m
Tower diameter (d)	0.01 m
Tower height (h)	0.375 m
Blade/strut profile	NACA0012
Aspect ratio (AR)	1
Solidity (σ)	0.2

Table 3.2: The turbine geometry along with their respective dimensions.

3.4 NUMERICAL SET-UP

This section contains the details of the simulation settings, mainly the spatial and temporal discretization. The mesh topology and domain descriptions are discussed in Section 3.4.1. The time steps and the relevant parameters are presented in Section 3.4.2.

3.4.1 Mesh and domain

The domain in terms of rotor diameter (D) is taken as $15D \times 8D \times 7D$, with the center of the turbine located at the origin $(0, 0, 0)$, where X is in the range of $[-5D, 10D]$, Y in $[-4D, 4D]$ and Z in $[-3.5D, 3.5D]$. This domain is discretized into smaller cells of various sizes for studying the sensitivity to spatial discretization. This is carried out by using the blockMesh command and defined using the blockMeshDict utility. The results from the spatial sensitivity study presented in Section 3.6.1, provide the basis for the choice of the coarse and fine mesh size.

The coarse mesh is obtained by dividing the $[X, Y, Z]$ into $[75, 40, 35]$ parts respectively. This generates $105,000$ cubical cells of size $[0.06m, 0.06m, 0.06m]$. This forms the coarse grid. Further refinements of this coarse grid give the fine mesh.

The fine mesh is generated by adding refinements to the coarse grid using snappyHexMeshDict and defined using the snappyHexMesh command. The snappyHexMeshDict utility provides options to specify the domain for which refinements can be separately defined. The final mesh includes 2 such domains; the outer zone defined from $(-3D, -3D, -3D)$ to $(10D, 3D, 3D)$ with a refinement level of 1 and inner zone from $(-2D, -2D, -2D)$ to $(10D, 2D, 3D)$ with a refinement level of 3. The snappyHexMesh utility divides every coarse grid cell into smaller sub-cells using the option of levels. Each level of refinement corresponds to splitting each dimension of the cell corresponding to the number associated with the level *e.g.*, refinement of a cell up to level 1 divides the cell into 8 sub-cells (splitting the cell length in X, Y and Z by half). Different refinement options were studied and the above-mentioned refinement was chosen for the simulation. The pictorial representation (top view) of the overall mesh is shown in Figure 3.3

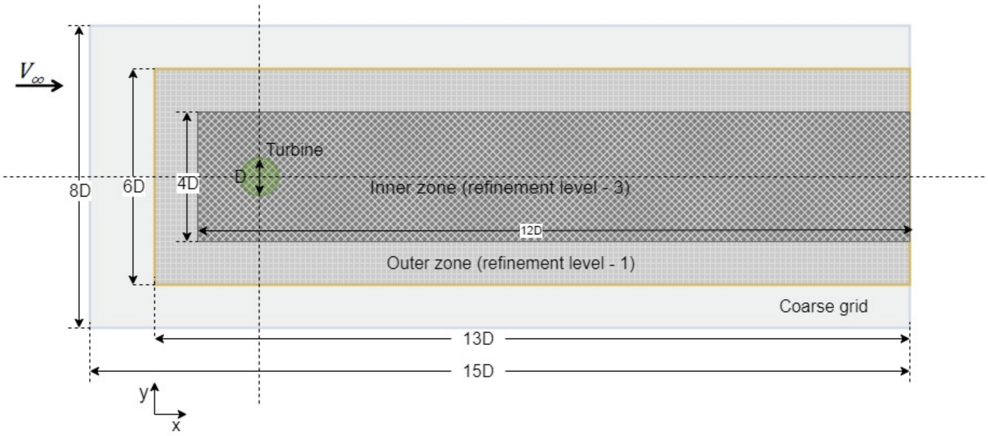

Figure 3.3: The top view (XY-plane) of the domain and the refinement zones.

3.4.2 Time steps

The magnitude of angular velocity (Ω) of the rotor, at the TSR of 2.5, is $\Omega = 83.34 rad/s$. An Euler implicit, first-order time marching scheme is employed in the simulation for time marching. A limit on the Courant number (Co) is imposed to regulate the width of the time step. The equation for Courant number is given by Equation 2.6. The Courant number is linked to Courant-Fredrichs-Lewy (CFL) condition required to solve partial differential equations with numerical approximations (Courant et al., 1967). A CFL of greater than 1 means that the information (in the current case the flow velocity V_i) propagates through more than one grid cell at each time step, leading to erroneous results. The effect of different Courant numbers on the accuracy of the simulation results was evaluated and a maximum Courant number of $Co_{max} < 0.6$ was chosen for the simulation to regulate the time steps. The cases and results of the temporal sensitivity analysis are presented in Section 3.6.2.

3.5 CONVERGENCE STUDY

At the start of a CFD simulation, at the time instant $t = 0s$ flow field velocity and the rotor velocity would be zero. When the simulation begins, at time instant $t = \Delta ts$ (where Δt is the simulation time step), the flow velocity and rotor velocity change to the value specified by the simulation settings. This sudden jump in the values within a small time step causes the blade loads to jump to abnormal values. Furthermore, the wake of the VAWT is not fully developed at the start of the simulation and takes time to attain a steady value.

Hence, a convergence study of the rotor power coefficient and far wake velocities is required to ensure that the sampled data is taken only after the convergence has reached. Section 3.5.1 presents the study conducted to evaluate the convergence of blade loading and wake. In addition to this, the pimpleFoam solver, in order to solve the N-S equations spatially for the flow field values (pressure and velocities), starts with a guess for the initial value. Several iterations are carried out within a time step, to reduce the residual errors below the specified tolerance value. At the end of each time step, the solver prints the final residual errors in the calculated flow field values. At the beginning of the simulation, these values are high since the initial guess values are largely different from the expected value at the end of each time step. However, these residual errors reduce as the simulation reaches convergence and fall nearly to a constant mean value. When this happens it can be concluded that the simulation has reached a steady state. It is important that the averaging is done after the steady state has reached, otherwise the results could be erroneous. Section 3.5.2 provides a discussion on the convergence of the simulation.

3.5.1 Wake convergence

In order to evaluate the convergence of the wake at the rotor, the instantaneous power coefficient (C_p) plot is obtained. To observe the convergence trend, the corresponding values (C_p) were averaged over each 360° rotation of the blade along the azimuth. Figure 3.4a shows the instantaneous value of C_p for the baseline case respectively. Figure 3.4b shows the values averaged over each rotation of the blades. From Figure 3.4b it can be clearly seen that the initial values of the $C_{p,avg}$ is very high, but reach a near-constant value (within a difference of $\pm 0.4\%$ of the average $C_{p,avg}$ value of the previous rotation), which corresponds to 10 full rotations of the turbine. However, this alone does not guarantee the convergence of wake over the entire domain. The convergence of the wake occurs latest at the farthest point in the domain *i.e.*, at $x = 10D$. Hence the instantaneous velocity of the wake at $x = 10D$ and $y, z = 0$ is plotted across the simulation time in Figure 3.5. It can be clearly seen from this plot that the wake velocities at $x = 10D$ converge approximately after a time of $t = 1.5s$. This provides the basis for averaging time for all further results shown here on, in this study. The averaging time for the velocity field values are taken from time $t = 1.5833s$ to $t = 2.7143s$ corresponding 15 complete rotations of the turbine.

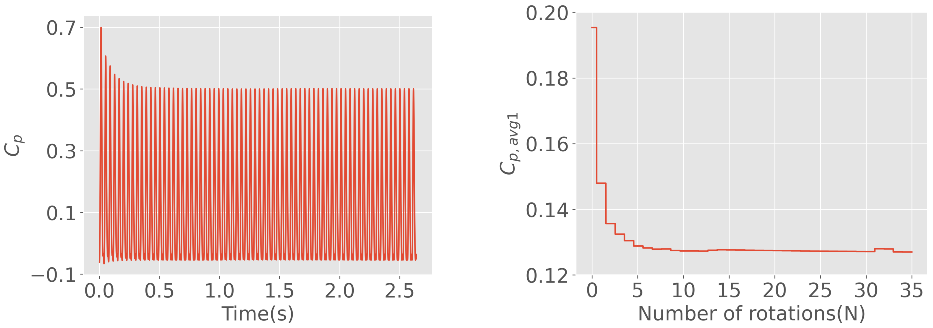

(a) Instantaneous power coefficient (C_p) of the turbine.

(b) The power coefficient averaged over each rotation ($C_{p,avg1}$).

Figure 3.4: The instantaneous and averaged power coefficient of the turbine as a function of time. The values are obtained from the simulation carried out for the baseline case.

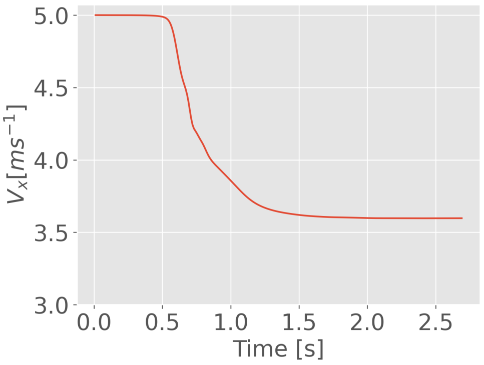

Figure 3.5: The streamwise wake velocity values at $x = 10D$ and $y, z = 0$ as a function of simulation time.

3.5.2 Simulation convergence

To evaluate the convergence trend of the simulation, the maximum of the initial residuals obtained for velocities (V_x, V_y and V_z) over the entire domain, at the end of each time step is plotted against the simulation time in X-axis. From Figure 3.6a, it can be clearly seen that the initial residuals of velocities are well below 0.01. The low initial residuals are an indication of convergence of the coupled system (pressure and velocities). However, the value final residuals determine the convergence of velocities in the simulation. Figure 3.6b shows the maximum of final residual values of the velocities over the entire domain. It can be seen that these values are well below 10^{-6} which indicates an acceptable level of convergence for the velocity values obtained from the simulation. Furthermore, the plots show that the simulation has reached a steady-state after $t = 1.5s$, which reinforces the choice of the averaging time mentioned in Section 3.5.1.

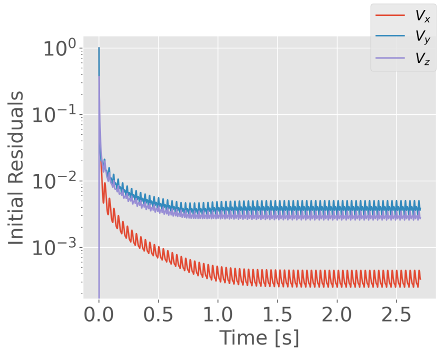

(a) The maximum of the initial residuals of velocities (V_x, V_y and V_z) obtained at the end of each time step.

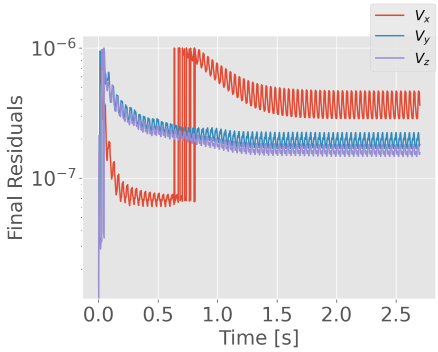

(b) The maximum of the final residuals of velocities (V_x, V_y and V_z) obtained at the end of each time step.

3.6 SENSITIVITY STUDY

In order to identify the optimal mesh size and time step to run the simulation, the spatial and temporal sensitivity analysis was conducted. While a very fine mesh gives more accurate results, it also increases the computational expenditure. A similar effect is observed when the simulation time step (Δt) value is reduced. Thus there is a need to find an optimal grid size and time step value to run the simulations. The sensitivity of the results to spatial discretization is discussed in Section 3.6.1 and the temporal sensitivity study is presented in Section 3.6.2.

3.6.1 Spatial sensitivity

To study the effect of spatial discretization the entire domain was discretized into coarse grids with a varying number of cells. The cases and the respective number of cells (N_{cells}) corresponding to each case is shown in Table 3.4. The refinement was also varied across the domain to observe the effect of refinement on the flow field values. The results of the refinement study (not shown in the report), show that the averaged turbine power coefficient ($C_{p,avg}$), is sensitive to the level of refinement. The total number of cells after the respective refinements is mentioned in Table 3.3 against each case, corresponds to the total cell count after all the refinements were carried out. The values of power coefficient (C_p) of the turbine averaged ($C_{p,avg_{10}}$) over the last 10 rotations was observed for each case and the plot of these values are shown in Figure 3.7a. It can be seen that the curve flattens out with the increase in the number of cells, meaning that the difference in $C_{p,avg_{10}}$ of the subsequent cases decrease with the increase in the cell count. In other words, the sensitivity to spatial discretization decreases with the increase in cell count. The final selected coarse grid and the refinement is a compromise between computational expenditure and accuracy of the results.

Cases	N_{cells}	$C_{p,avg_{10}}$
Case 1	$6,241,536$	0.135
Case 2	$9,911,328$	0.130
Case 3	$14,794,752$	0.127
Case 4	$23,591,400$	0.122
Case 5	$40,703,040$	0.119

Table 3.3: The different cases of mesh discretizations along with the total cell count after their respective refinements (N_{cells}) and the coefficients of power averaged over the last 10 rotations ($C_{p,avg_{10}}$) of the turbine.

3.6.2 Temporal sensitivity

To analyse the effect of the time step of the simulation (Δt), several simulations with Courant numbers (Co) varying from 0.2 to 0.8 was carried out. The power coefficient averaged over the last 10 rotations ($C_{p,avg_{10}}$), post simulation convergence, was taken as the evaluating parameter. Table 3.4 provides the Co and total number of time steps per revolution ($N_{timesteps}$) of the respective cases and Figure 3.7b shows the variation of $C_{p,avg_{10}}$ with the total number of time steps per revolution of the turbine. The curve again shows a decreasing sensitivity with the decrease in the Δt width.

Cases	Co	$N_{timesteps}$	Δt (s)	$C_{p,avg_{10}}$
Case 1	0.9	135.2	0.000557	0.131
Case 2	0.8	154.2	0.000488	0.129
Case 3	0.7	175.2	0.000430	0.128
Case 4	0.6	203.5	0.000370	0.127
Case 5	0.5	245.5	0.000307	0.126
Case 6	0.4	306.3	0.000246	0.125
Case 7	0.3	407.8	0.000185	0.124
Case 8	0.2	606.1	0.000124	0.122

Table 3.4: The cases studied for different Courant numbers (Co) along with the total number of time steps per revolution ($N_{timesteps}$), the width of the time step (ΔT) and the power coefficient averaged over the last 10 rotations ($C_{p,avg_{10}}$) of the turbine.

3.6.3 Discussion

The results of spatial and temporal sensitivity analysis show a decreasing trend of sensitivity with an increase in number of cells and a decrease in the width of the time step respectively. The spatial sensitivity is higher than the temporal sensitivity which is in line with the findings of Bachant and Wosnik and Mendoza et al.. Based on this study the coarse grid was chosen with a total number of $105,000$ cells, with $[75,40,35]$ cell divisions along $[X,Y,Z]$ directions respectively. The refinement was chosen as shown in Figure 3.3. A maximum Courant number of $Co_{max} < 0.6$ corresponding to approximately 203 time steps per revolution was chosen as the best fit

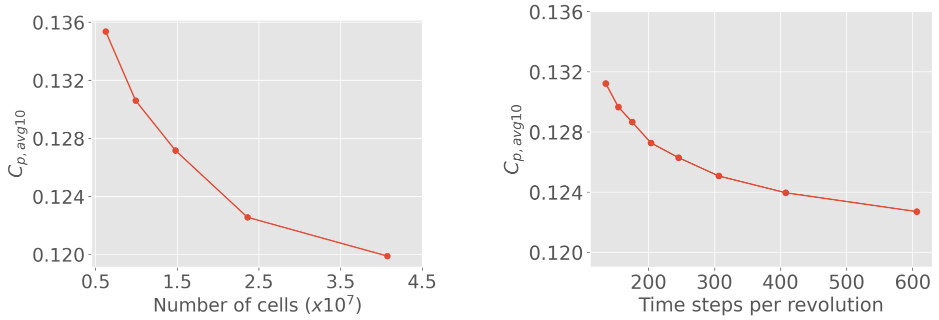

(a) The variation power coefficient averaged over the last 10 rotations of the turbine($C_{p,avg_{10}}$) with increasing cell count (in the order of $\times 10^7$).

(b) The variation power coefficient averaged over the last 10 rotations of the turbine($C_{p,avg_{10}}$) with an increasing number of time steps per revolution.

Figure 3.7: Spatial and temporal sensitivity analysis.

to carry out further study. An overview of the final mesh and time step settings is shown in Table 3.5

Simulation Parameter	Value
Time step (dt)	$0.0004s$
Maximum Courant number (Co)	0.6
Coarse mesh cell count	$105,000$
Coarse cell size	$0.06m$
Refined mesh cell count	$12,769,218$
Refined cell size	$0.0075m$
Wake velocity averaging time	$1.5833s - 2.7143s$

Table 3.5: The final values of the time step and mesh settings.

3.7 EXPERIMENTAL SET-UP

The simulation is validated against the experiment carried out by Huang et al. at the open jet facility (OJF). The experiment is carried out with an inflow velocity of $5ms^{-1}$ at the inlet of the turbine. The turbulence intensity in the OJF at the inlet is less than 2%. A straight-bladed H-rotor VAWT with the same turbine geometry and operational parameters (refer Section 3.3) as that of the simulation is used. The velocity field in the wake is measured using stereoscopic Particle Image Velocimetry (PIV) measurements. The velocity field is sampled at downstream planar surfaces starting from $x = 1D$ to $x = 10D$ with the intervals of $1D$. The sampled velocity field data is used for the validation of the simulation. The experimental set-up in OJF, is shown in Figure 3.8.

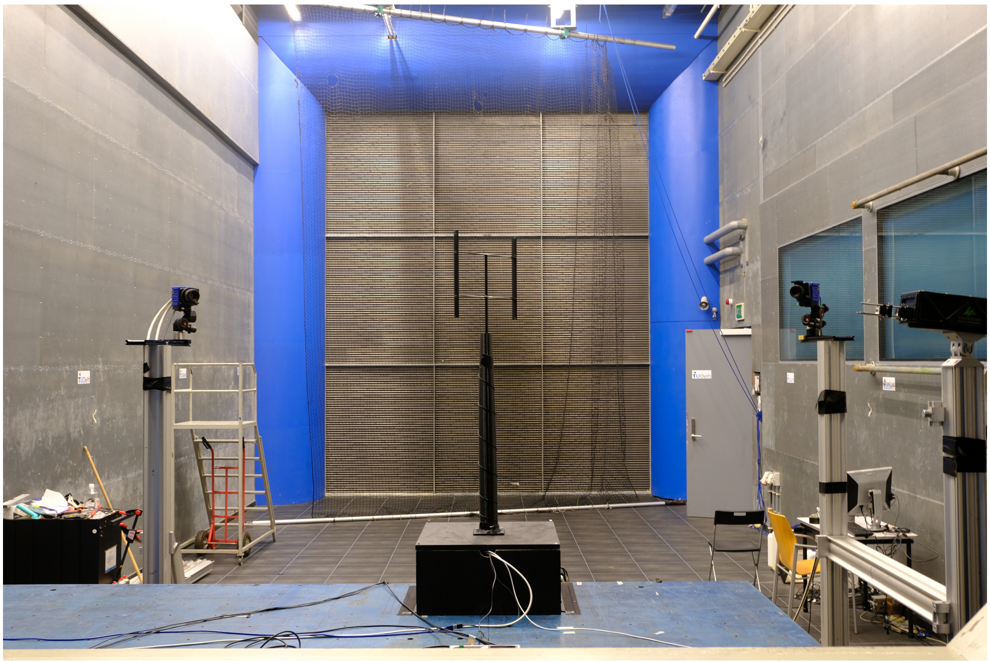

Figure 3.8: A picture of the VAWT used in the experiment (Picture credit: Ming Huang).

4 RESULTS: ISOLATED DOWN-SCALED VAWT

In this chapter, the results of the study are presented along with discussions on different physical phenomena occurring during the operation of a VAWT, from the perspective of its performance and wake characteristics. The study carried out here, specifically addresses the research questions pertaining to :

- The parameters to evaluate the turbine performance and wake properties.
- The effect of the correction models (dynamic stall model, turbulence model settings) on the simulation results.

At the outset, a discussion is presented on the parameters affecting the turbine performance and the wake of an isolated VAWT in Section 4.1 and Section 4.2 respectively. Since the dynamic stall and the turbulence model have a significant effect on the turbine performance and the wake, a sensitivity study is conducted to evaluate their effects. Section 4.3 provides a discussion on the dynamic stall models. Section 4.4 presents a discussion on the performance of the standard KE turbulence model with varying inlet conditions. The evaluation of the results is carried out both qualitatively and quantitatively. The deviation of the simulation results from the experimental results and the possible reasons are discussed.

4.1 TURBINE PERFORMANCE PARAMETERS

The main indicator of a VAWT's performance is its instantaneous (and averaged) power (C_p) and torque (C_T) coefficients of the rotor. However the values of C_p and C_T are directly affected by the tangential force coefficient (C_{tan}) which in turn depend upon AOA (α), relative velocity (V_{rel}), lift (C_l) and drag(C_d) coefficients. All the above parameters are affected by dynamic stall, which results in changes to the blade loading, consequently affecting the C_p and C_T (Laneville and Vittecoq, 1986). The turbulence affects the blade loading by affecting the onset of the dynamic stall (Wang et al., 2014). Thus there is a need to evaluate the effect of each of these models on the turbine performance parameters mentioned above. The variation of each of these parameters, over one rotation of the turbine, are discussed below for the baseline case, with the B-L-SGC dynamic stall model (Sheng et al., 2008), standard KE turbulence model (Launder and Spalding, 1974), Goude flow curvature model (Goude, 2012), added mass model (Strickland et al., 1979) and a tip correction model (Bachant et al., 2016).

4.1.1 Power and torque coefficients

The maximum value of instantaneous power coefficient ($C_{p,max} = 0.50$) and torque coefficient ($C_{T,max} = 0.20$) of the rotor, is reached at an azimuthal angle of $\theta_{max1} = 59.20^\circ$ and at $\theta_{max2} = 239.20^\circ$ as seen in Figure 4.1a and Figure 4.1b respectively. It can be noted that the relation between the power and torque coefficients can be given by $C_p = C_T \times \lambda$, where λ is the TSR. The first peak of the power (C_p) and torque (C_T) coefficient curves is due to the maximum values of C_p and C_T for the first blade, while the second peak is due to the maximum corresponding values of the second blade. This can be seen from the torque coefficient for the individual

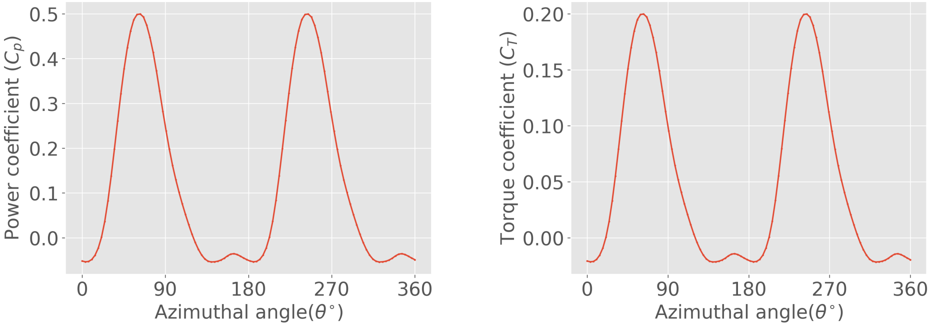

(a) Instantaneous power coefficient(C_p) of the turbine during one complete rotation.

(b) Instantaneous torque coefficient(C_T) of the turbine during one complete rotation.

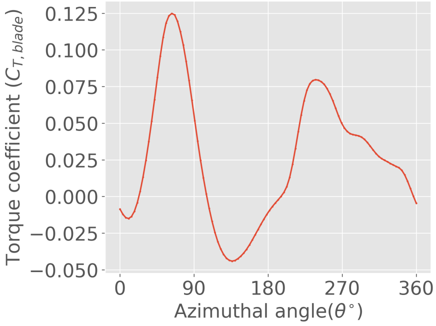

(c) Instantaneous torque coefficient($C_{T,blade}$) of one individual blade during one complete rotation averaged over the span of the blade.

Figure 4.1: The variation of the power and torque coefficients during one rotation of the turbine for the baseline case.

blade, plotted in Figure 4.1c. The local C_p and C_T values are different at the different spanwise locations of the blades due to varying induction. The induction at the tips is largely affected by tip vortices and the induction at the mid-span by bound circulation and tip vortices (for low aspect ratios). Due to the smearing of forces in the ALM, the spanwise forces are not significantly different, however, the tip correction marginally compensates to include this effect in the model.

4.1.2 Blade and turbine loads

The blade loads are mainly, lift and drag forces which are determined by their respective coefficients C_l, C_d and by the relative velocity V_{rel}. The resolution of these forces along normal and tangential directions to the blade path gives the normal (C_n) and tangential (C_{tan}) force coefficients respectively. The resolution of the blade forces along the inflow wind direction (X direction) gives the thrust coefficient (C_t). The thrust coefficient on the blade ($C_{t,blade}$) and the turbine (C_t), according to the sign convention in this study (refer Section 3.3), is positive.

The variation of lift and drag coefficients, over one rotation is shown in Figure 4.2. The maximum value of the drag coefficient ($C_{d,max} = 0.46$) at the mid-span section, occurs at an azimuthal position of $\theta = 121.77°$ for an individual blade, while the maximum lift coefficient ($C_{l,max} = 1.21$) at the mid-span location, occurs at the azimuthal position of $\theta = 66.23°$. The magnitude of the lift and drag coefficients depends on the AOA and chord Reynolds number. The maximum power and torque coefficients occur around the maximum lift coefficient values of the mid-span section. The respective minima of the power and torque coefficients occur around the maximum drag values at the mid-span section. This is because the turbine is driven by lift forces.

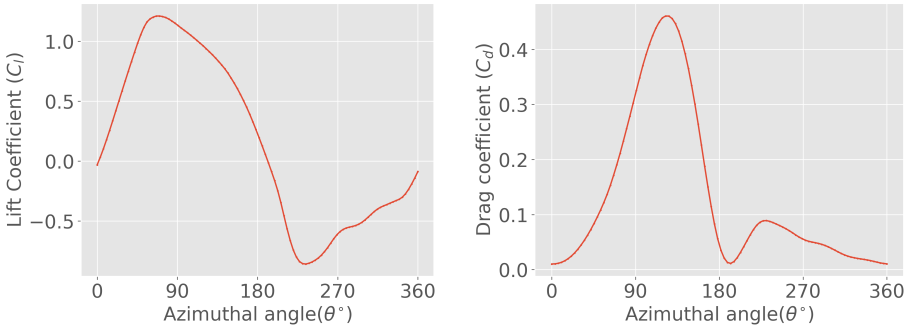

(a) Variation of the lift coefficient(C_l) during one complete rotation of the first blade, at the mid-span section.

(b) Variation of drag coefficient(C_d) during one complete rotation of the first blade, at the mid-span section.

Figure 4.2: Variation of the lift and drag coefficients during one complete rotation of the first blade, at the mid-span section.

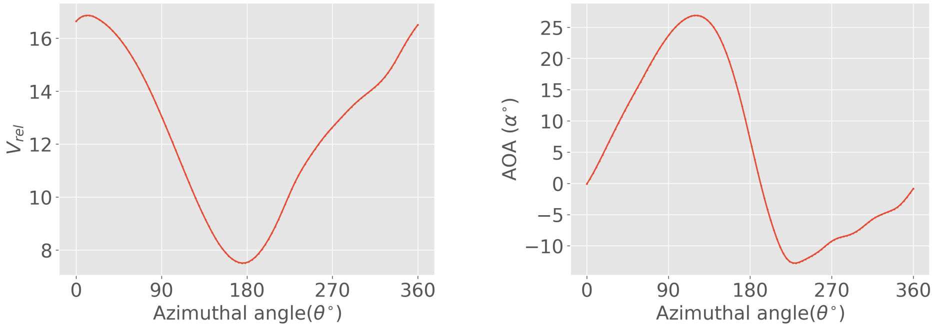

(a) Variation of the magnitude of the relative velocity(V_{rel}) of the first blade at the mid-span section during one complete rotation.

(b) Variation of AOA (α) during one complete rotation of the first blade at the mid-span section.

Figure 4.3: The variation of AOA and relative velocity at the mid-span section of the blade, over one rotation of the turbine for the baseline case.

The variation of AOA at the mid-span section (shown in Figure 4.3b) is large, ranging from $\alpha = 26.90^\circ$ at $\theta = 118.30^\circ$ to $\alpha = -12.80^\circ$ at $\theta = 225.52^\circ$. The maximum value of AOA noted here is much higher than the stall AOA which occurs at $\alpha = 10.6^\circ$ for a chord Reynolds number of $Re_c = 2 \times 10^4$. The magnitude of relative velocity (shown in Figure 4.3a) also varies significantly over one rotation from $V_{rel} = 16.86ms^{-1}$ to $V_{rel} = 7.50ms^{-1}$ causing a large variation in chord Reynolds number from $Re_c = 2.25 \times 10^5$ to $Re_c = 5.05 \times 10^5$. So when the turbinesFoam module interpolates the C_l and C_d values from the static polars at $Re_c = 2 \times 10^4$, some errors are expected.

The peak blade normal coefficient ($C_{n,max} = 1.2$) in one rotation occurs at an azimuthal location of $\theta = 69.6^\circ$. It can be seen that this occurs close to the peak C_l. The variation of the lift (C_l) and normal (C_n) coefficient with the variation of AOA shows the unsteady effect as a consequence of dynamic stall and added mass (refer Figure 4.4). Post the static stall AOA at $\alpha = 18.7^\circ$, the leading edge separation begins and the blade reaches deep stall at the maximum AOA of $\alpha = 22.9^\circ$ that occurs at an azimuthal position of $\theta = 121.5^\circ$, when the vortex passes the trailing edge. Then, as the AOA decreases the C_l and C_n trace the lower section of the curve until the flow reattaches at around $\alpha = 0.55^\circ$, post which the C_l and C_n trace the upper section of the curve.

The magnitude of maximum thrust coefficient of one blade ($C_{t,blade,max} = 1.16$), occurs at an azimuthal angle of $\theta = 90.41^\circ$ whereas the magnitude of maximum thrust coefficient of the turbine ($C_{t,max} = 1.31$), which is the summation of the

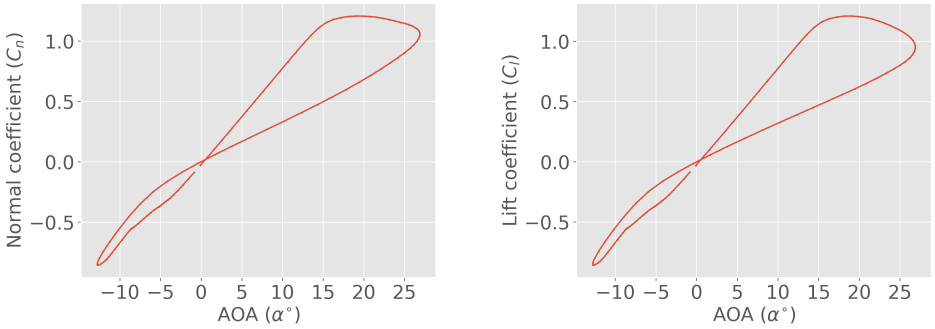

(a) Variation of normal coefficient(C_n) of one blade, with varying AOA (α) during one complete rotation at the mid-span section.

(b) Variation of lift coefficient(C_l) with varying AOA (α) during one complete rotation at the mid-span section.

Figure 4.4: The variation of the lift and normal force coefficients as a function of AOA.

individual blade thrust coefficients, occurs at $\theta_1 = 72.95.52°$ and $\theta_2 = 253°$. This can be seen in Figure 4.5

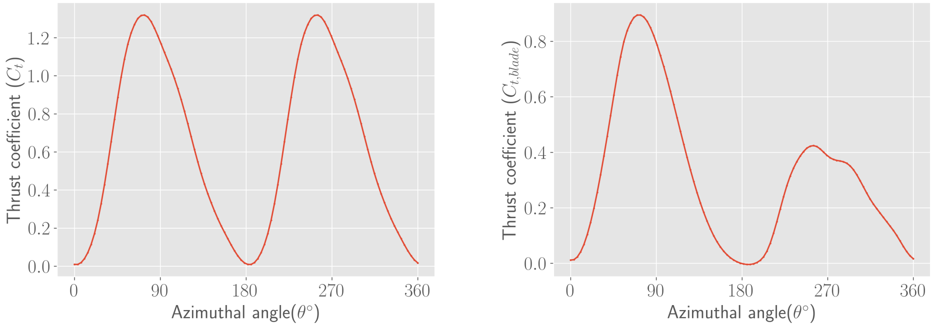

(a) Magnitude of instantaneous thrust coefficient (C_t) of the turbine during one complete rotation.

(b) Magnitude of instantaneous thrust coefficient ($C_{t,blade}$) of an individual blade during one complete rotation.

Figure 4.5: Magnitude of instantaneous thrust coefficient during one complete rotation.

4.2 WAKE VALIDATION PARAMETERS

The wake of a VAWT, on the other hand, can be studied by observing the averaged velocity, vorticity and pressure fields of the wake obtained from the simulations. Since the averaged velocity fields at different downstream locations, is the only data available from the experiments for this study, the validation parameter is inevitably chosen as the averaged wake velocity fields. However, it is necessary to observe the influence of vorticity and pressure fields on wake. This is elaborated in the subsequent sections.

4.2.1 Averaged velocity contour

Qualitative analysis can be made with the velocity contour plots of the wake at various downstream locations to observe the evolution of the wake in the downstream direction. To quantitatively evaluate the wake structure and wake deflection, the mid-span velocity profile of the wake at different downstream locations can be studied in comparison with the experimental data. Further, a comparison of wake deficits obtained from different cases of the simulations can be used to evaluate the

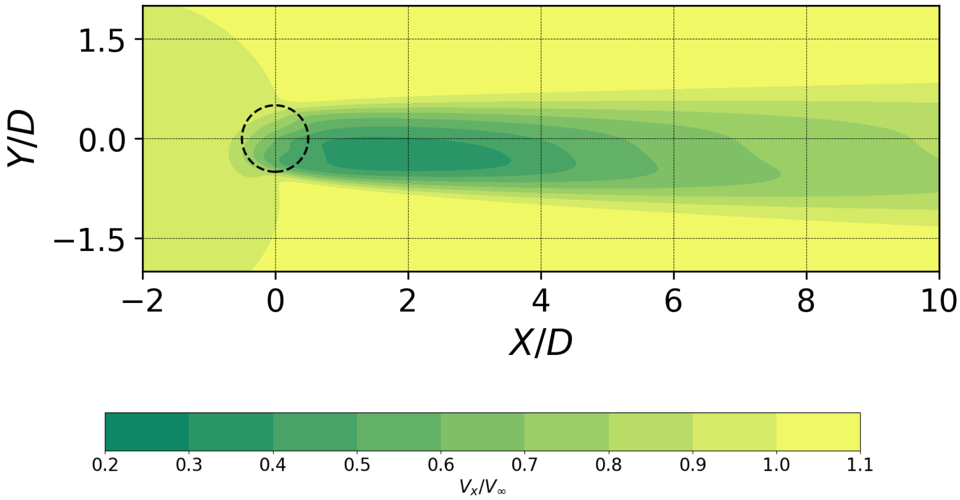

Figure 4.6: The top view of the XY-plane averaged, mid-span, streamwise velocity contour. The X and Y axes are non-dimensionalized with the turbine diameter. Velocity (V_x) is non-dimensionalized with freestream wind speed ($V_\infty = 5ms^{-1}$).

effects of turbulence and dynamic stall on the wake. Thus the averaged streamwise wake velocities (V_x) are taken as the evaluating parameters for the study of the wake.

The thrust and power coefficients of the turbine have a direct influence on the velocity deficits in the wake. This is explained with the thrust force exerted by the turbine on the flow leading to extraction of kinetic energy from the flow, subsequently causing a velocity deficit in the wake. Furthermore, the azimuthal location at which the maximum thrust force occurs has an influence on the location at which the maximum deficits are seen in the wake. The thrust coefficient has a direct relation with the induction from the momentum theory, which explains this influence. A contour plot of the averaged, mid-span, streamwise velocity (V_x) shown in Figure 4.6 gives a clear visualization of the wake velocity deficits.

At the outset it can be seen that the largest deficits in the mid-span, immediately behind the turbine, occur on the windward side ($-Y$ direction) where the blade loading C_t, C_n are the highest. The momentum influx can be seen as occurring from the leeward side, where the wake deficits are lower causing the largest deficits to move towards more towards the windward side, downstream. This momentum influx is enhanced by mid-span vorticity which is explained in Section 4.2.2.

4.2.2 Instantaneous vorticity contour

Physically, the bound circulation around the blade is a consequence of blade loading. A change in the blade loading changes the bound circulation which leads to vortices being shed into the wake, affecting the wake velocities as it convects downstream. Hence, the shed vorticity generated due to the changing bound circulation around the blade, the trailing vorticity dependent on the strength of the bound circulation, the tip vortices arising from the influx of momentum from the pressure side to the suction side of the airfoil, the shed vorticity due to the occurrence of dynamic stall, the shed vorticity from the loading on the struts and the tower wake, all influence the velocity field of the wake. However, the component of vorticity of interest for this study is the mid-span shed vorticity contour and tip vortices. Figure 4.7 shows the mid-span section of the Z-plane vorticity over one entire rotation of the turbine.

The plot shows counter-rotating vortices of different strengths. The clockwise rotating (into-the-plane, negative) vortex seen on the suction side is the shed vorticity due to dynamic stall, the anti-clockwise rotating (out-of-plane, positive) vortex around the blades at the mentioned azimuthal locations (θ and $\theta + 180^\circ$ respectively) represent the bound vorticity and the streak of red (out-of-plane, positive) shows the shed vorticity in the windward side (at $y = -0.5D$ in Figure 4.7). The strength of the shed vorticity depends on the rate of change of bound circulation ($d\Gamma/dt$) around the airfoil, as the blade traverses along the azimuth. This is a consequence of Kelvin's circulation theorem for potential flow which states that the net rate of change of circulation in a closed loop is zero.

The maximum value of the shed vorticity on the windward side appears to occur near $\theta = 0^\circ$ (refer Figure 4.7a and Figure 4.7d). The onset of stall occurs at $\theta = 69^\circ$ at which point, the strength of the clockwise rotating vorticity appears to reach its maximum value (refer Figure 4.7b and Figure 4.7f). As the azimuthal angle increases further, this shed clockwise vorticity decreases in strength. At $\theta = 121.5^\circ$, when the deep stall is reached, the vortex is fully shed into the wake.

While it is difficult to conclude the azimuthal location corresponding to the maximum bound vorticity from the contour plot due to the lack of continuous time intervals, the lifting line theory suggests that the maximum bound vorticity should correspond to the maximum product of $\vec{V}_{rel} \times \vec{L}$. Similarly, since the shed vorticity is dependent upon the rate of change of the force field around the blade (or consequently rate of change of circulation), it is difficult to ascertain the azimuthal location at which the maximum shed vorticity occurs.

The periodically shed vortices can be clearly seen in the wake on the leeward side up to $x = 2D$ beyond which its strength decreases significantly. The vorticity on the windward side, however, is discernible up to downstream distances of $x = 4D$, beyond which its strength wanes. In Figure 4.7c the blade-wake interactions can be observed, where the blade located at $x = 0.4D, y = -0.1D$ is seen moving into the shed vortex generated by the other blade. From the vorticity plots, it can be seen that blade-wake interaction is increased if the dynamic stall onset occurs in the upwind sections. If the dynamic stall onset occurs earlier in the windward side (as a consequence of a positive blade pitch angle) then the blade-wake interactions are expected to be minimal.

There is an influx of momentum from the sides due to the shed vorticity that induces a cross-stream component (V_y) into the wake, subsequently enhancing the wake recovery downstream seen in Figure 4.6. The tip vortices have a significant influence on the mid-span section due to the low aspect ratio of the turbine ($H/D = 1$). While the tip vortices lead to a spanwise induction at the blade, reducing its performance, the influx of momentum into the wake downstream from the sides, is enhanced by the tip vortices. The strength of these vortices depends on the blade forces at the tips. Further, the turbulence in the flow has an impact on the dissipation of the vortices in the wake, in addition to its effects on the dynamic stall and blade loading. So the effect of turbulence needs to be separately evaluated from the perspective of the vorticity dissipation and blade loading.

4.2.3 Instantaneous pressure contour

The static pressure difference (calculated as $\Delta p_{static} = \Delta p_{kinematic}\rho$) field around the turbine visualized in Figure 4.8 clearly show the stagnation points occurring at the airfoil surface at different azimuthal positions during one rotation of the turbine. The largest stagnation pressures correspond to the largest blade loading at the mid-span section as seen in Figure 4.8b and Figure 4.8f. This corresponds to the largest C_n values although a more reliable conclusion can only be drawn with more time intervals. Finally, it can be observed that the tower has little influence on the pressure field.

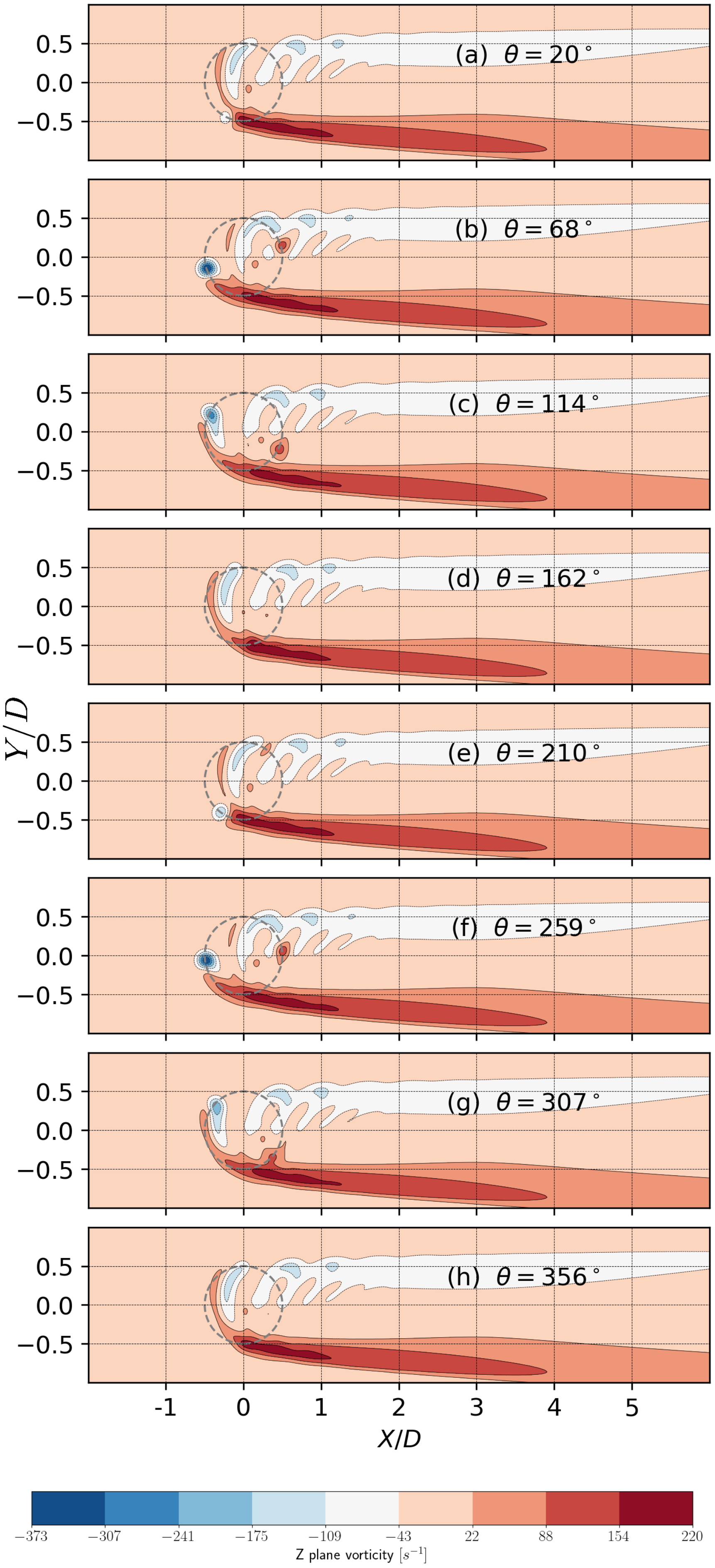

Figure 4.7: The top view of the XY-plane instantaneous vorticity contour. The X and Y axes are non-dimensionalized with the turbine diameter.

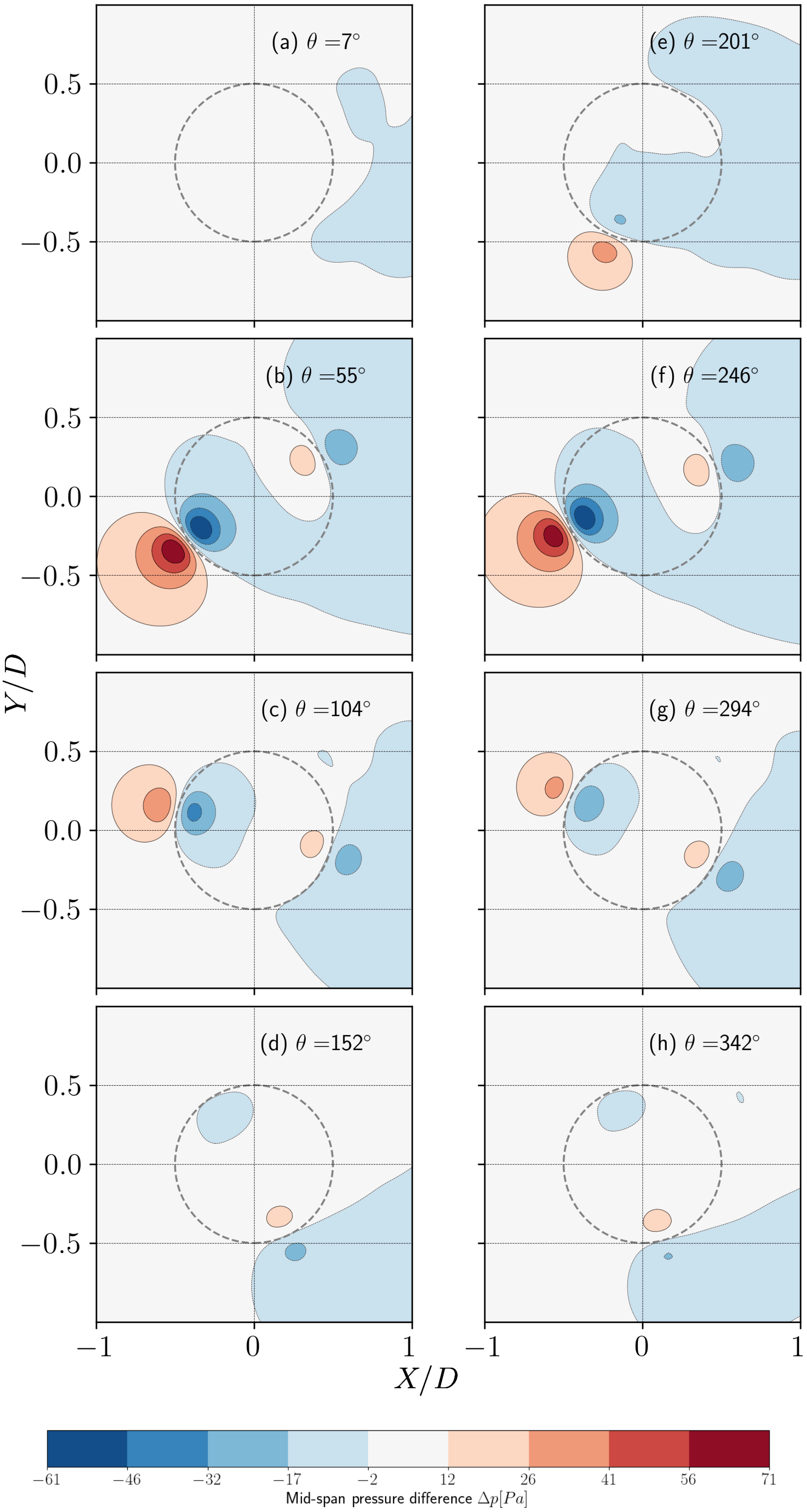

Figure 4.8: The contour plot of the pressure field (Δp_{static}) at the mid-span location over one rotation of the turbine. The X and Y axes are non-dimensionalized with the turbine diameter.

4.3 DYNAMIC STALL MODEL SENSITIVITY

In this section, the results of the simulations carried out to study the effect of the dynamic stall models are presented. The study cases include 3 different models of B-L dynamic stall models and one case without a dynamic stall model. The different dynamic stall models implemented are the standard B-L model (Leishman and Beddoes, 1986), B-L-3G model (Beddoes, 1993) and B-L-SGC model (Sheng et al., 2008). This follows from the literature review presented in Section 2.3.1 where B-L models are stated to perform better than the Gormont model. The dynamic stall models are semi-empirical models and largely depend on the airfoil for which the empirical constants are obtained (Dyachuk et al., 2014). Thus all the parameters chosen for this study correspond to NACA0012 blade geometry.

The parameters associated with B-L-SGC model are mentioned in Table 4.1. The parameters T_p, represents the delay constant to attain the same normal force coefficient C_N in a delayed leading-edge pressure under unsteady conditions; T_f, represents the delay constant for separation point due to dynamic effect; T_α is the delay constant for AOA due to dynamic effect. The critical stall onset AOA is given by α_{ds0}; r_0 is the reduced pitch rate given by $\dot{\alpha}c/2V_\infty$ ($\dot{\alpha}$ is the rate of change of AOA); T_{vl} is the vortex passage time constant; T_v, the time constant for vortex passing over the chord; B_1 is the airfoil dependant constant used to calculate the additional increase in normal force due to dynamic vortex; η is the efficiency factor used to calculate the tangential force coefficient. The default value of η is 0.95 in the SGC module provided by turbinesFoam library. The constant E_0 is used for chordwise force calculation which is a revision to the original B-L model, modified by Sheng et al. (2008). The parameters associated with B-L-3G model are given by Table 4.2. The parameters T_p, T_f, T_v, T_{vl} and η represent the same parameters as the B-L-SGC model. The parameters T_1, T_2, A_1, A_2 and A_3 represent the constants used in the deficiency functions X_n, Y_n and Z_n, which are used in the calculation of the effective AOA. The values of the different parameters associated with the standard B-L model are provided in Table 4.3. The parameters T_p, T_f, T_v, T_{vl} and η represent the same parameters as the B-L-SGC model. The additional parameters A_1, A_2, b_1 and b_2 are the constants in the calculation of deficiency functions X_n and Y_n (Dyachuk and Goude, 2015). Dyachuk and Goude (2015) further note that the parameters T_p and T_f do not depend on the airfoil while other parameters do.

T_p	T_f	T_α	α_{ds0}	r_0	T_{vl}	T_v	B_1	η	E_0
1.7	3.0	3.9	18.73	0.01	8	11	0.75	1	0.25

Table 4.1: The B-L-SGC coefficients used for modelling dynamic stall (Dyachuk and Goude, 2015).

T_p	T_f	T_1	T_2	T_{vl}	T_v	A_1	A_2	A_3	η
1.7	3.0	20	4.5	11.0	6.0	0.3	0.7	0.75	0.95

Table 4.2: The B-L-3G coefficients used for modelling dynamic stall (Beddoes, 1993).

T_p	T_f	A_1	A_2	b_1	b_2	T_{vl}	T_v	η
1.7	3.0	0.3	0.7	0.14	0.53	8.0	11.0	0.95

Table 4.3: The standard B-L coefficients used for modelling dynamic stall (Leishman and Beddoes, 1986)

Cases	Dynamic stall model	$C_{p,avg10}$	$C_{t,avg10}$
Case 1	None	0.210	0.534
Case 2	Standard B-L	−0.026	0.637
Case 3	B-L-3G	0.052	0.599
Case 4	B-L-SGC	0.127	0.626

Table 4.4: The different cases of the dynamic stall evaluated and their corresponding mean values of power (C_p) and thrust (C_t) coefficients. The mean values are calculated by averaging the corresponding instantaneous values over the last 10 rotations of the turbine.

4.3.1 Turbine scale

The effect of the dynamic stall on the blade loading is to increase it beyond that of the stall value, thus significantly increasing the maximum instantaneous thrust and power coefficients of the turbine. In addition to this, the dynamic stall delays the occurrence of the maximum instantaneous thrust and power coefficients of the turbine. Figure 4.9 shows the variation of different turbine performance parameters for the different dynamic stall models. The effect of the dynamic stall model on the C_p and C_t curves of the turbine is very clear on comparison of the same for the cases with and without dynamic stall (refer Figure 4.9a and Figure 4.9b). The results without dynamic stall predict lower peak values of instantaneous C_p and C_t with the exception of the standard B-L model. The reasons for the deviation of the standard B-L model are analysed in the latter half of the section. The mean values of C_p and C_t for each case is shown in Table 4.4. It is not surprising to observe that the mean power coefficient value of the case without a dynamic stall model, are higher than that of the cases with the dynamic stall models. This can be explained with the following reasoning:

- Although the peaks of the instantaneous C_p values are higher for the cases with dynamic stall, they occur only for a brief period of time.
- After reaching the stall angle the C_p values drop steeply, plunging to negative values. Whereas in the case without dynamic stall the C_p curve is flatter, dropping gradually post the static stall angle.
- In the cases with the dynamic stall since variation in the blade loading is higher, the shed vorticity is stronger. This leads to increased blade-wake interactions in the downwind passages of the blade when the second blade is in the wake of the first blade and vice-versa. This leads to a larger loss of power than in the case without dynamic stall (refer C_p curve at azimuthal angles of $90° - 180°$ and $270° - 360°$ in Figure 4.9a).

In the literature, the onset of dynamic stall generally refers to the formation of leading-edge vortex (refer Figure 2.5). However, in this study, since it is not possible to determine the exact AOA at which the leading-edge separation begins, the stall onset is identified with the occurrence of maximum C_l which occurs when the blade is in stall. In SGC model this corresponds to the parameter α_{ds0}.

The effect of the delay on the onset of stall of the blade, due to the dynamic stall models, can be seen in the C_l curve for the mid-span section shown in Figure 4.9c. The case without the dynamic stall predicts stall onset the earliest among all the cases, at an azimuthal position of $\theta = 45.4°$ corresponding to the AOA value of $\alpha = 13.8°$. Note that the value of α here is still greater than its static stall angle because of the added mass model. The B-L-3G model predicts stall onset at an azimuthal position of $\theta = 68.96°$, closely followed by the SGC model where the

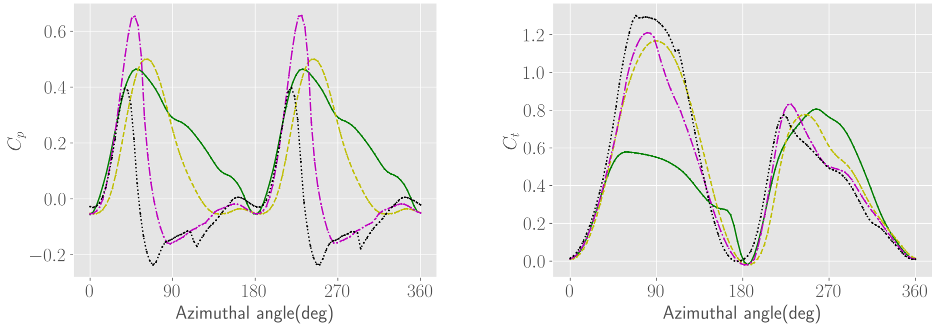

(a) Instantaneous power coefficient(C_p) of the turbine during one complete rotation.

(b) Instantaneous thrust coefficient($C_{t,blade}$) on one blade during one complete rotation.

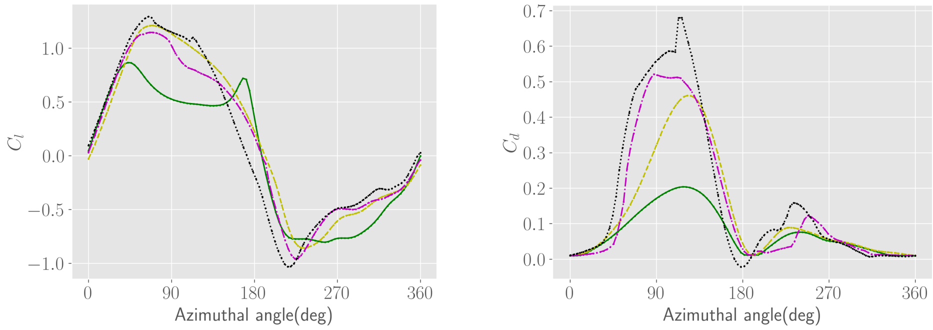

(c) Variation of the lift coefficient(C_l) during one complete rotation of the first blade, at the mid-span section.

(d) Variation of drag coefficient(C_d) during one complete rotation of the first blade, at the mid-span section.

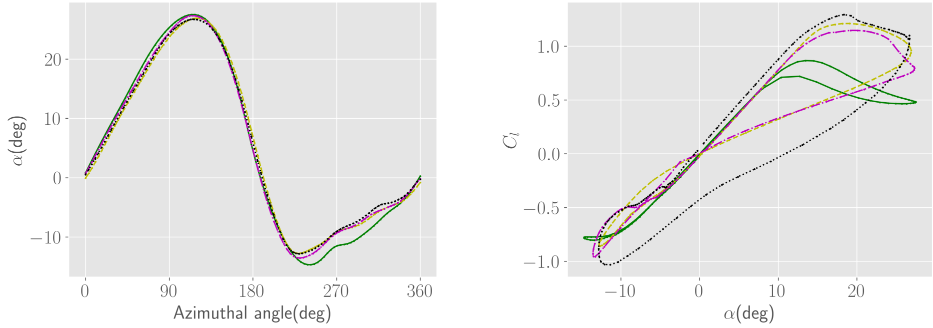

(e) Variation of AOA (α) during one complete rotation of the first blade at the mid-span section.

(f) Variation of lift coefficient(C_l) with varying AOA (α) during one complete rotation at the mid-span section.

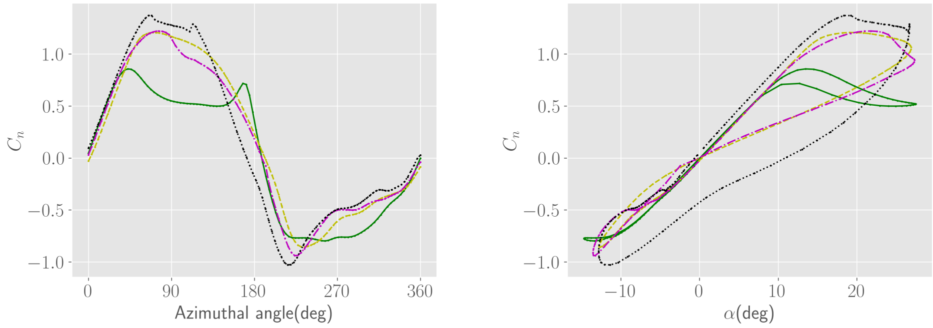

(g) Instantaneous normal force coefficient(C_n) at the mid-span section of the first blade during one complete rotation.

(h) Variation of normal coefficient(C_n) with varying AOA (α) during one complete rotation at the mid-span section.

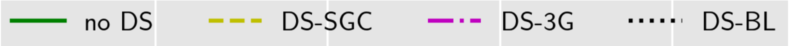

Figure 4.9: The variation of the different turbine performance parameters for the different cases of dynamic stall sensitivity study. All the parameters are ensemble averaged over 10 rotations of the turbine.

same occurs at $\theta = 69.35°$. The SGC model has an additional parameter to correct the onset of dynamic stall (α_{ds0}) which is not available in the other models. This correction leads to the prediction of onset of the dynamic stall at $\alpha = 18.73°$. It is interesting to see that the onset of the stall for the standard B-L model is predicted latest at an azimuthal angle of $\theta = 70.1°$. The peak values of C_l and C_d at the mid-span section for this model, are also higher than the other models (refer Figure 4.9c and Figure 4.9d).

It can be further observed from Figure 4.9e that the AOA does not significantly vary with and without the dynamic stall model except in the downwind passage of the blade. This is due to the increased induction at the blade in the downwind section, due to the increased blade-wake interactions, as a consequence of increased shed vorticity generated by the dynamic stall. Finally, Figure 4.9f shows the variation of the lift coefficient with the AOA. For the case without a dynamic stall model, since there is no deep stall, the lift coefficient follows the same curve with the exception of the region where AOA is greater than the stall angle. This difference is due to the added mass model, where, to increase the AOA the airfoil must exert more force on the flow to accelerate the air mass around it, to facilitate the change increase in the AOA. However to decrease the AOA the flow aids the acceleration of the air mass leading to a lower loading on the blade. While the deep stall for each of the dynamic stall models is predicted approximately at the same AOA the flow reattachment prediction of the standard B-L model deviates significantly from others. It can also be noted that the standard B-L model deviates in its prediction of the lift coefficient from the static polar data which could explain the anomalous behaviour of its C_p and C_t curves. This deviation is not observed for the 3G or SGC models.

4.3.2 Wake scale

The effect of dynamic stall on the wake is mainly the increased blade loading (read as higher C_n and $C_{t,blade}$, shown in Figure 4.9g and Figure 4.9b) leading to higher wake velocity deficits. Increased shed vorticity is observed as a consequence of increased variation in the blade loading. The wake velocity contour plots for the different cases are shown in Figure 4.11. The blade loading in the case without dynamic stall is lower and has two azimuthal locations ($\theta = 45°, 170°$) where the C_n peaks. The velocity contour of the same case at $x = 1D$, shown in Figure 4.11a, clearly shows the 'H' shape corresponding to these peaks in the C_n. It is interesting to note the location of this 'H' shape deficit at the $x = 1D$ downstream location. First maximum loading that occurs at blade location of $x = -0.35D, y = -0.35D$, shows up in the deficit at $x = 1D, y = -0.4D$ whereas the second maximum loading corresponding to blade location of $x = -0.08D, y = 0.49D$, shows in the deficit at $x = 1D, y = -0.1D$. This displacement of the deficits highlights the fact that the deficits corresponding to leeward side loading move more rapidly towards the windward side than the deficits corresponding to windward side loading.

The peak blade loading is the highest for the standard B-L model followed by SGC model and 3G model as noted in Figure 4.9g. Subsequently, their corresponding near-wake deficits seen from the contour plots at $x = 1D$, seen in Figure 4.11b, Figure 4.11c and Figure 4.11d, for each of these models follow the same order. It can be noted that the contour plots in the far-wake ($x = 8D$ and beyond), have similar structures. This is in line with the experimental findings of Tescione et al., that the effect of the dynamic stall is only seen in the near-wake. Another observation that can be drawn from the contour plot is that the standard B-L model predicts larger leeward blade loading than SGC and 3G models. This is concluded from the contour plot Figure 4.11c that shows a larger deficit velocity region ($V \in (0.2V_\infty, 0.31V_\infty)$) compared to other models.

Since a qualitative study of these contour plots does not provide the magnitudes of the differences in the wake velocities between the cases, the wake profiles at the

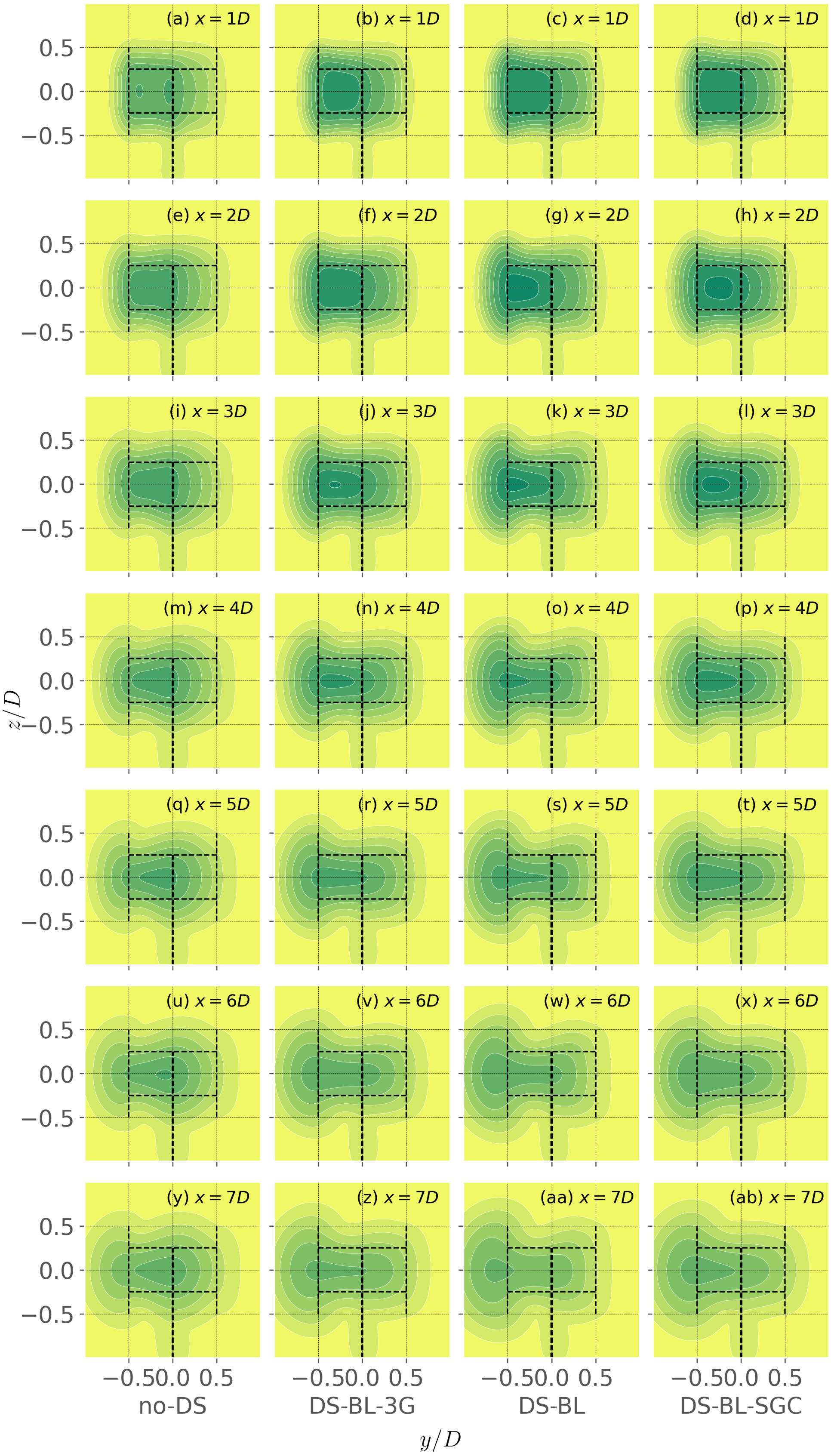
(a) $x = 1D$
(b) $x = 1D$
(c) $x = 1D$
(d) $x = 1D$
(e) $x = 2D$
(f) $x = 2D$
(g) $x = 2D$
(h) $x = 2D$
(i) $x = 3D$
(j) $x = 3D$
(k) $x = 3D$
(l) $x = 3D$
(m) $x = 4D$
(n) $x = 4D$
(o) $x = 4D$
(p) $x = 4D$
(q) $x = 5D$
(r) $x = 5D$
(s) $x = 5D$
(t) $x = 5D$
(u) $x = 6D$
(v) $x = 6D$
(w) $x = 6D$
(x) $x = 6D$
(y) $x = 7D$
(z) $x = 7D$
(aa) $x = 7D$
(ab) $x = 7D$
0.5
0.0
−0.5
z/D
−0.5
0.0
0.5
no-DS
DS-BL-3G
DS-BL
DS-BL-SGC
y/D

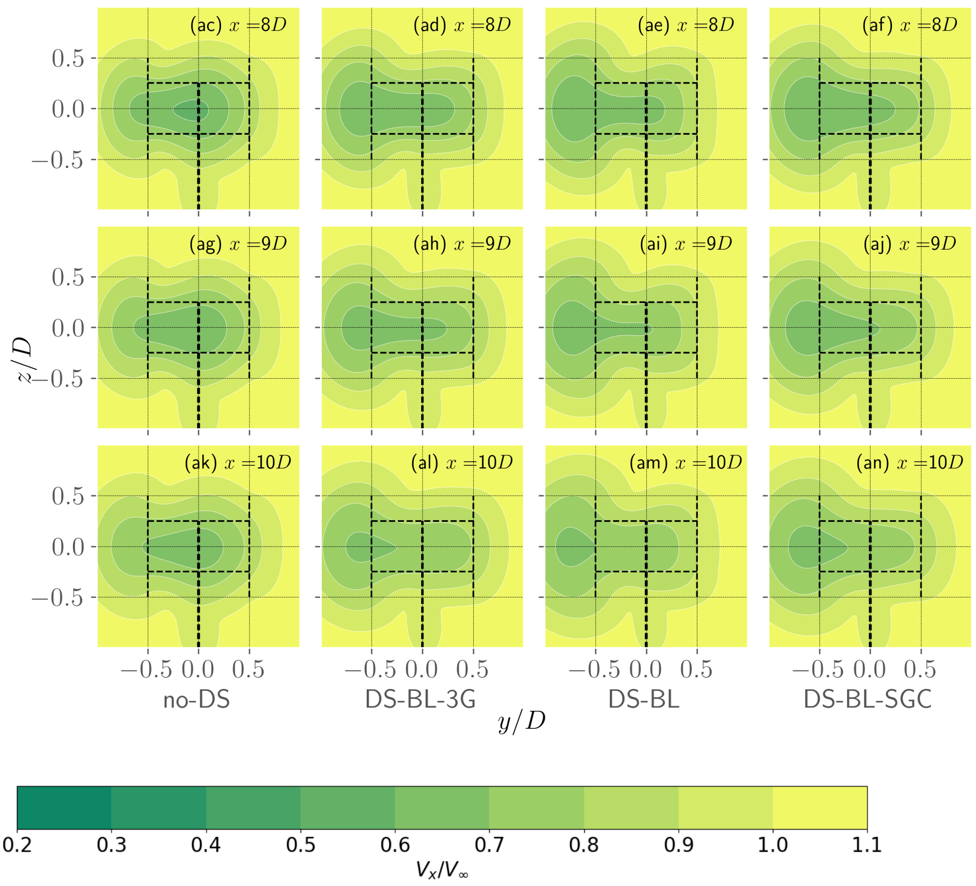

Figure 4.11: The streamwise velocity contour (V_x) at different downstream distances(x), as seen from the downstream location, is predicted by different dynamic stall (DS) models and without a DS model. The Y and Z axes are non-dimensionalized with turbine diameter ($D = 0.3m$) and the velocity is non-dimensionalized with inflow velocity ($V_\infty = 5ms^{-1}$).

mid-span sections for each case up to $x = 10D$ are plotted in Figure 4.12. Further, the experimental measurements of the wake velocity profiles at the mid-span section in the downstream locations are also plotted alongside the cases. This allows an evaluation of the accuracy of each of these models in their ability to predict wake profiles. Further, the extent of deviation can be also compared from one model to another, in comparison with the experimental data.

In Figure 4.12a, we clearly see that the largest wake deficit of the standard B-L model corresponds to $V = 0.35V_\infty$, whereas the SGC and 3G models have the wake velocities of around $V = 0.38V_\infty$. However, the case without a dynamic stall model, which has the lowest blade loading has the velocity of $V = 0.52V_\infty$. It is interesting to note that the windward side asymmetry in the wake leads to a marginal increase in the peak velocity deficit at the mid-span section at a downstream distance of $x = 2D$ for the simulation results (compare Figure 4.12a and Figure 4.12b at $y = 0.25D$). However, the experimental results do not show the same behaviour. It can further be noted that this asymmetry in the simulation results is more pronounced in the near-wake than in the experimental results. At $x = 1D$ plane the simulation predicts that the peak deficit is at $y = 0.25D$ whereas the experiment shows the peak deficit at $y = 0.1D$. This implies that the simulation predicts a larger blade loading at a smaller azimuthal angle than the experiment, hinting that the onset of dynamic stall could be predicted too early in all the implemented B-L models. The peak deficit of the experimental found at $y = 0.1D$ at $x = 1D$ is also larger and sharper than that of the simulation implying that the severity of the dynamic loading could be under-predicted in the simulations.

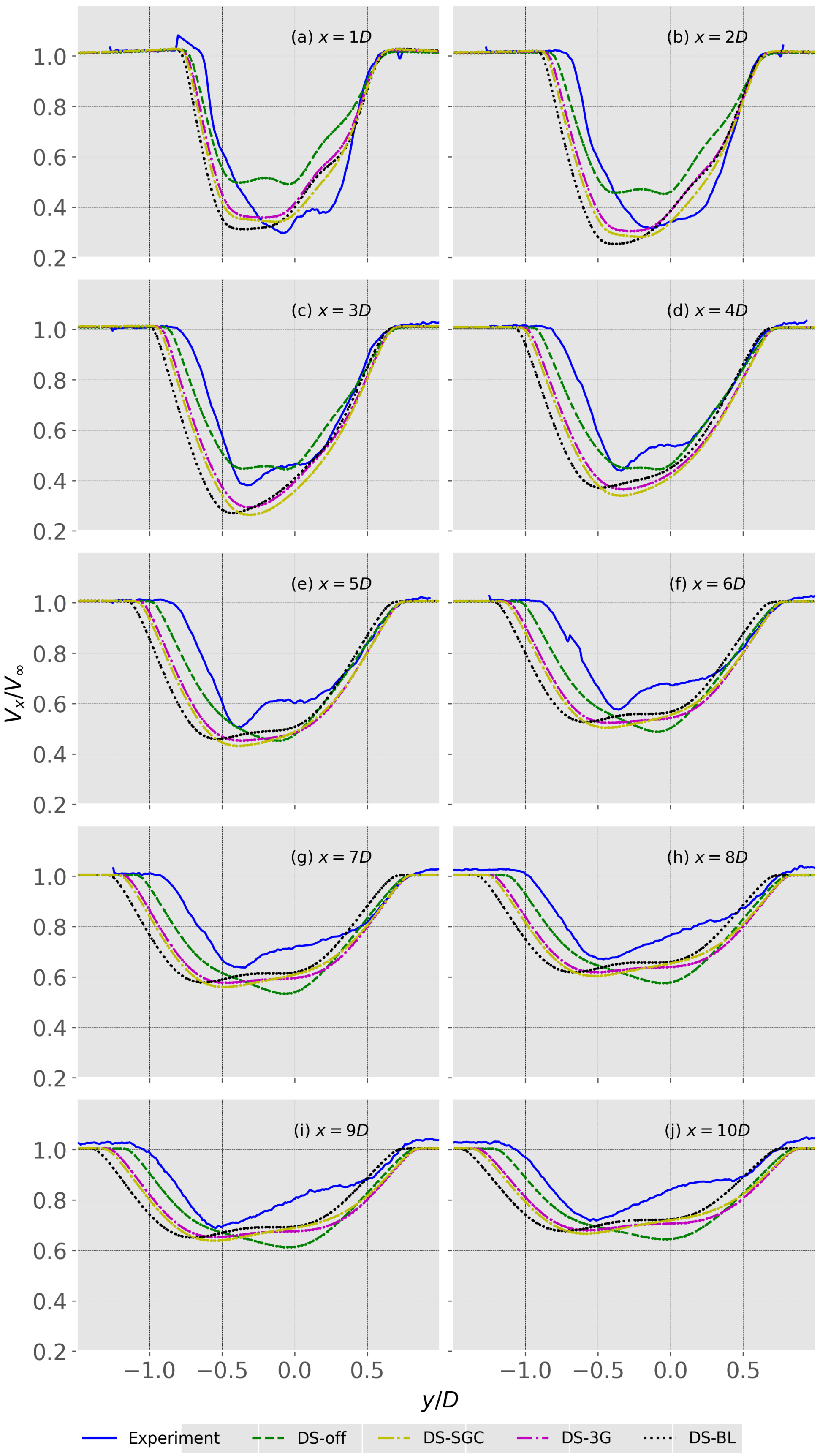

Figure 4.12: A comparison of the wake profiles at the mid-span sections for different cases of the dynamic stall models and the experimental data. The axis is non-dimensionalized with rotor diameter ($D = 0.3m$) and velocity with freestream wind speed ($V_\infty = 5ms^{-1}$)

All the models significantly under-predict the leeward side blade loading leading to much higher wake velocities ($0.6V_\infty$) at $y = 0.25D$, compared to the experimental values which shows a second dip in wake velocity (of the order $0.4V_\infty$ (refer Figure 4.12a). From downstream distances of $x = 3D$ the leeward side deficits match closely to the experimental results.

Further downstream the wake expansion in the far-wake is the largest for the standard B-L model followed by SGC, 3G and case without dynamic stall. Compared to the experiment the expansion of the wake is over-predicted. The experimental peak velocity deficit found at $x = 1D$, recovers slower than the peak deficit of the simulation results and is deflected from $y = 0.1D$ at $x = 1D$, to $y = 0.5D$ at the downstream distance of $x = 8D$. The simulation peak deficit in on the other hand deflects from $x = 1D, y = -0.35D$ to $x = 8D, y = -0.7D$. It is also noted that while the deflections in the wake for the three models are close to each other, the order of deflection follows the order of blade loading (*i.e.* standard B-L>SGC>3G), implying that the wake asymmetry and hence the deflection is enhanced by the blade loading. Despite the larger wake deficit in the near-wake, the far-wake of all the models show that the wake recovers to the same velocity of $0.72V_\infty$. This also implies that the larger deficits of the standard B-L model recover faster than the lower deficits of the case without a dynamic stall, suggesting that the recovery of the wake far downstream is enhanced by higher instantaneous blade loading.

Finally, since the performance of each of the dynamic stall models depends significantly on the coefficients (mentioned in Table 4.1, Table 4.2 and Table 4.3), a definitive performance comparison would need a fine-tuning of these parameters. However, from this study, the following points can be inferred:

- The dynamic blade loading has a significant impact on the wake deficits and hence the wake asymmetry.
- The standard B-L model deviates significantly from other models indicating that its coefficients need further fine-tuning.
- All the models need to be corrected for the prediction of onset of the dynamic stall and for azimuthal location at which the deep stall occurs.
- In order to evaluate the performance of each of the models a deeper study with fine-tuned parameters for each model is indispensable.

4.4 TURBULENCE MODEL SENSITIVITY

To evaluate the impact of the turbulence model the simulation was carried out without a turbulence model and compared with the simulation results with the standard $k-\epsilon$ model (KE) turbulence model. The standard KE model uses the Boussinesq hypothesis (refer Equation 2.46) to model the Reynolds stress tensor ($\tau_{ij} = -\overline{u'_i u'_j}$) in the Reynolds averaged Navier-Stokes (RANS) (refer Equation 2.39 and Equation 2.45) description of the flow field. In this model, the eddy viscosity(ν_T) is taken a function of the turbulent kinetic energy ($k = 0.5\overline{u'_i u'_i}$) and turbulent dissipation ($\epsilon = \nu\overline{u_{i,k}u_{j,k}}$), given by Equation 4.1. Additionally the closure to the problem is obtained by transport equations for turbulent kinetic energy as given by Equation 4.2 and turbulent dissipation, given by Equation 4.3. The values of empirical constants are taken from Launder and Spalding (1974), are given by, $C_\mu = 0.09$, $\sigma_k = 1.0$, $\sigma_\epsilon = 1.3$, $C_{\epsilon 1} = 1.44$ and $C_{\epsilon 2} = 1.92$.

$$\nu_T = C_\mu \frac{k^2}{\epsilon} \tag{4.1}$$

$$\frac{\partial k}{\partial t} + \overline{u_j}\frac{\partial k}{\partial x_j} = \tau_{ij}\frac{\partial \overline{u_i}}{\partial x_j} - \epsilon + \frac{\partial}{\partial x_j}\left[(\nu + \frac{\nu_T}{\sigma_k})\frac{\partial k}{\partial x_j}\right] \tag{4.2}$$

$$\frac{\partial \epsilon}{\partial t} + \overline{u_j}\frac{\partial \epsilon}{\partial x_j} = C_{\epsilon 1}\frac{\epsilon}{k}\tau_{ij}\frac{\partial \overline{u_i}}{\partial x_j} - C_{\epsilon 2}\frac{\epsilon^2}{k} + \frac{\partial}{\partial x_j}\left[(\nu + \frac{\nu_T}{\sigma_\epsilon})\frac{\partial \epsilon}{\partial x_j}\right] \tag{4.3}$$

The presence of turbulence mainly allows for the recovery of the wake through turbulent transport of the mean kinetic energy and turbulent dissipation of the kinetic energy of shed vortices. In addition to this, the effect of higher turbulence intensities is also observed on the onset of the dynamic stall and hence the instantaneous blade loading. The standard KE model is robust in the freestream conditions and in the absence of adverse pressure gradients which is usually found within the boundary layers. Since ALM uses the blade-element method with a dynamic stall model to calculate the blade loading, the boundary layers at the airfoil are not resolved. So for the current study, the standard KE model is deemed fit as the wake is predicted best by this model. However, since this model is not validated, it is necessary to study the sensitivity of the model to inlet turbulence intensities and their corresponding k and ϵ values. The value of ϵ for a given value of k, depends on the length scale. The choice of the length scale of (l), for the ϵ calculations, follows the reasoning that the turbulent dissipation is mainly affected by larger eddies (Katopodes, 2019) and largest eddies at the inlet of the low turbulence wind tunnel are of the order of mesh wire diameter (Roach, 1987). Since the experiment was carried out in the OJF at low turbulence conditions, the equivalent mesh wire diameter is expected to be a small value. However, a range of length scale values ($l \in [0.002, 0.2]$) were chosen for the study in combination with different inlet turbulence intensities. While the study included a corresponding range of ν_T values from 0.00015 to 0.637, the cases presented here are chosen to show the behaviour of the standard KE model. The different cases included in the study are shown in Table 4.5. All the cases are run with the B-L-SGC model of dynamic stall.

Cases	Inlet Condition	I	k	ϵ	ν_T	$C_{p,avg10}$	$C_{t,avg10}$
Case 1	No turbulence	-	-	-	-	0.125	0.622
Case 2	Low turbulence	0.51%	10^{-3}	3×10^{-4}	3×10^{-4}	0.129	0.630
Case 3	Medium turbulence	0.7%	0.0018	2.4×10^{-5}	0.0128	0.155	0.674
Case 4	High turbulence	2%	0.015	5.5×10^{-4}	0.0367	0.160	0.681

Table 4.5: The turbulent kinetic energy (k) and turbulent dissipation (ϵ) values at the inlet for different cases of the simulations carried out. The mean C_p and C_t are calculated by averaging the corresponding instantaneous values over the last 10 rotations of the turbine.

4.4.1 Turbine scale

The effect of the inlet turbulence is evident on both, the instantaneous and the averaged values of C_p. With increasing turbulence intensity the C_p values increase substantially as seen in Figure 4.13a and Figure 4.13b respectively. The increase in the average C_p values are substantially higher between the low turbulence and high turbulence cases, showing an increase of 19.3%. However the C_t values for the same only increase by 8.1%. It is to be noted that, while the boundary layers are not resolved, the pressure differences arising from the force exerted by the blades on the flow could still cause high pressure gradients, leading to the overestimation of turbulent diffusion within these regions. It is interesting to see that the peak C_l and C_d values decrease with increasing inlet turbulence intensities (refer Figure 4.13c and Figure 4.13d). The decrease in C_l values is however smaller than the decrease in C_d values leading to higher power outputs at higher turbulence intensities. The downwind C_l curves, however, show higher values for lower turbulence intensities. The

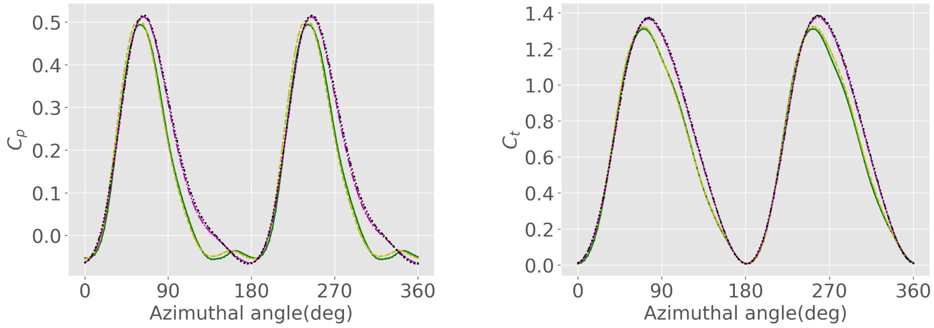

(a) Instantaneous power coefficient(C_p) of the turbine during one complete rotation.

(b) Instantaneous thrust coefficient($C_{t,blade}$) of the one blade during one complete rotation.

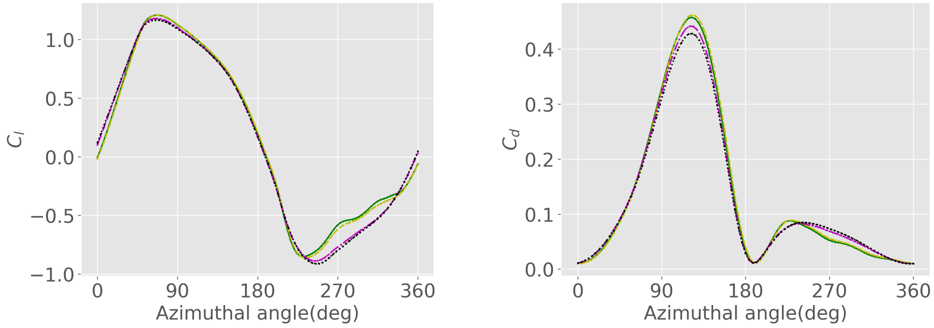

(c) Variation of the lift coefficient(C_l) during one complete rotation of the first blade, at the mid-span section.

(d) Variation of drag coefficient(C_d) during one complete rotation of the first blade, at the mid-span section.

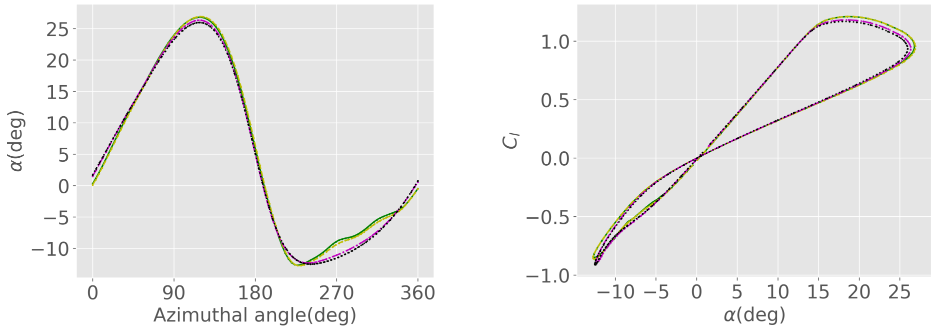

(e) Variation of AOA (α) during one complete rotation of the first blade at the mid-span section.

(f) Variation of lift coefficient(C_l) with varying AOA (α) during one complete rotation at the mid-span section.

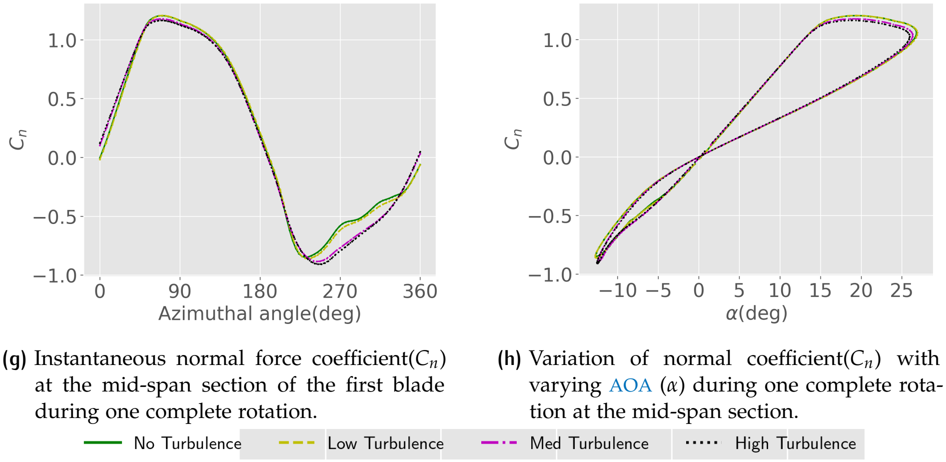

(g) Instantaneous normal force coefficient(C_n) at the mid-span section of the first blade during one complete rotation.

(h) Variation of normal coefficient(C_n) with varying AOA (α) during one complete rotation at the mid-span section.

Figure 4.13: The variation of the different turbine performance parameters for the different cases of dynamic stall sensitivity study. All the parameters are ensemble averaged over 10 rotations of the turbine.

drag coefficient increases in the downwind half with increasing turbulence intensities. This behaviour can be explained with the following analogy. In the upwind half where the dynamic stall occurs, the higher turbulence intensities, reduce the impact of the deep stall as a consequence of turbulent reattachment of the flow. This effect can be clearly seen in Figure 4.13f and Figure 4.13h, where the values of C_l and C_n at deep stall are lower for higher turbulence intensities. In the downwind passage of the blade, the AOA is less affected by the shed vorticity, as the values of ϵ is significantly higher at higher turbulence intensities, leading to faster dissipation of the vortices. This effect can be seen in the curves of AOA, in downwind sections, shown in Figure 4.13e. Also, the higher turbulence implies higher turbulent drag, which leads to higher C_d values for higher turbulence intensities, in the downwind sections (refer to downwind sections in Figure 4.13d). While the onset of dynamic stall does not seem to be affected by the turbulence intensities, the deep stall AOA decreases marginally with increasing turbulence intensities. Consequently, the azimuthal location at which the deep stall occurs is marginally advanced.

4.4.2 Wake scale

The effect of inlet turbulence intensity (I) is drastic on the wake velocities. The values of turbulent dissipation (ϵ) is directly proportional to $k^{1.5}$ (and to I^3). Further, the eddy viscosity (ν_T) values are directly proportional to I and l, which means that the ν_T values increase with the inlet turbulent intensities and inlet length scales of the eddies.

Larger ν_T values lead to higher wake recoveries. Figure 4.14 shows the contour plots of the wake velocities at different downstream locations from $x = 1D$ to $x = 10D$. It is evident that the case without turbulence predicts very high velocity deficits (refer Figure 4.14a) despite the relatively lower values of C_p and C_t (refer Figure 4.13a and Figure 4.13b). Comparing the plots for the case without turbulence at different the wake recovery is severely affected in the absence of turbulence with the lowest velocities in the range of $0.2V_\infty - 0.3V_\infty$ at downstream distances of $x = 10D$. Whereas even with a low turbulence intensity of $I = 0.5\%$, the wake shows a much faster recovery (refer to the low turbulence case in Figure 4.14).

The standard KE model seems to be highly sensitive to the inlet turbulence intensity values. This can be seen in the contour plots for medium and high turbulence cases, where the shape of the velocity contour does not resemble the turbine structure even at the downstream distance of $x = 1D$, despite having very high C_p and C_t values of the turbine. Further, it can be noted that by the downstream distances of $x = 6D$ the medium and high turbulence cases show up to 95% recovery in the wake velocities whereas, with low turbulence case ($I = 0.5\%$), the wake recovers only by 60%.

The effect of the inlet ν_T values on the wake expansion can be observed by comparing the different mid-span velocity profiles shown in Figure 4.15. The wake of the no turbulence case marginally expands by 20% from $x = 1D$ to $x = 5D$ whereas the low turbulence case has a 30% expansion for the same downstream distance. The cases with higher ν_T values show even higher expansion of the wake. Thus it can be concluded that the wake expansion is enhanced by increasing inlet ν_T values.

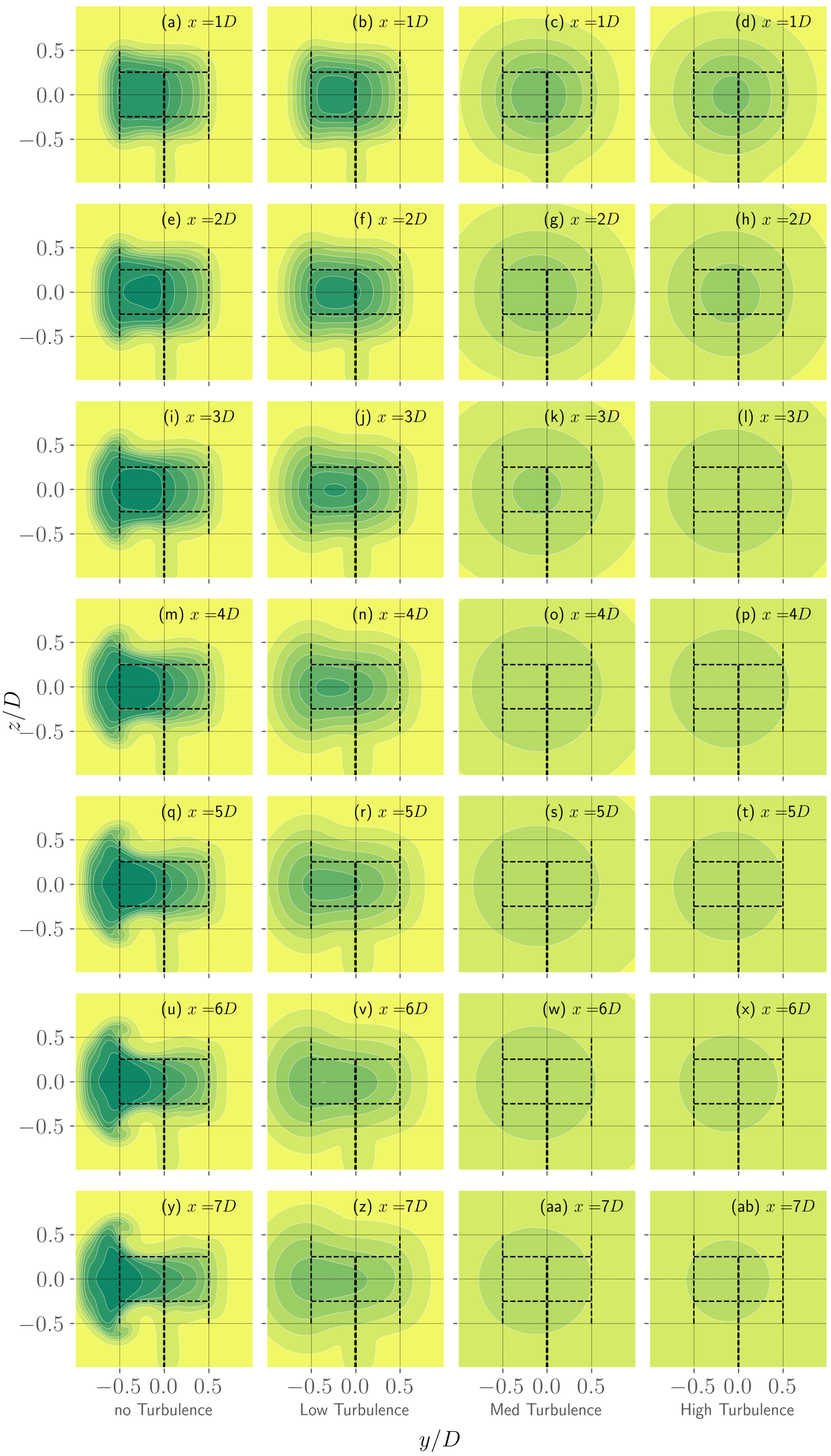
(a) $x=1D$
(b) $x=1D$
(c) $x=1D$
(d) $x=1D$
(e) $x=2D$
(f) $x=2D$
(g) $x=2D$
(h) $x=2D$
(i) $x=3D$
(j) $x=3D$
(k) $x=3D$
(l) $x=3D$
(m) $x=4D$
(n) $x=4D$
(o) $x=4D$
(p) $x=4D$
(q) $x=5D$
(r) $x=5D$
(s) $x=5D$
(t) $x=5D$
(u) $x=6D$
(v) $x=6D$
(w) $x=6D$
(x) $x=6D$
(y) $x=7D$
(z) $x=7D$
(aa) $x=7D$
(ab) $x=7D$
z/D
0.5
0.0
−0.5
−0.5 0.0 0.5
no Turbulence
Low Turbulence
Med Turbulence
High Turbulence
y/D

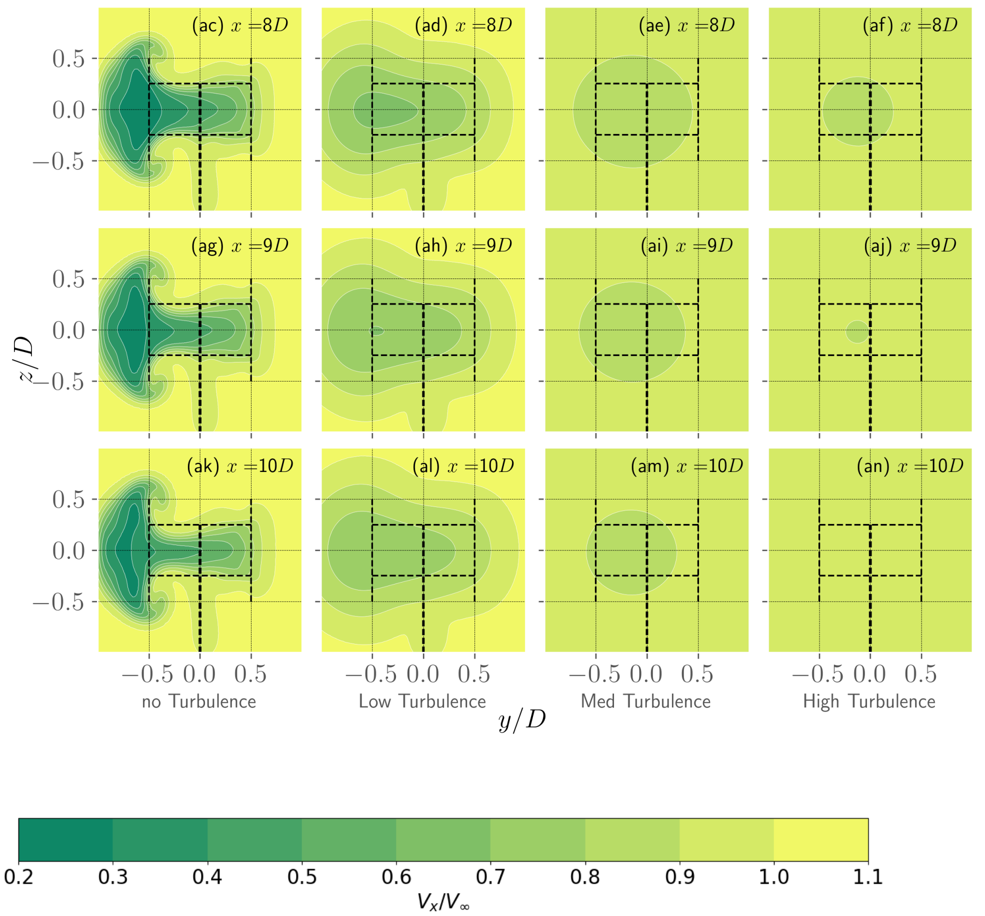

Figure 4.14: The streamwise velocity contour (V_x) at different downstream distances(x), as seen from the downstream location, predicted by different cases of eddy viscosity values (refer Table 4.5). The Y and Z axes are non-dimensionalized with turbine diameter ($D = 0.3m$) and the velocity is non-dimensionalized with inflow velocity ($V_\infty = 5ms^{-1}$).

Thus the main conclusions that can be drawn from this study are:

- The deep stall AOA and hence the duration of the blades in stall decreases marginally with an increase in inlet turbulence intensities.
- The power and thrust coefficients of the turbine increase with an increase in inlet turbulence intensity and length scale values (*i.e.*with an increase in eddy viscosity values).
- Despite the higher $C_{t,avg}$ values at higher eddy viscosity values (ν_T), the observed wake deficits are significantly lower, which is explained by higher recovery rates of the wake velocities.
- The wake recovery and expansion is significantly enhanced by increasing inlet eddy viscosity (ν_T) values.
- The standard-KE model is very sensitive to inlet eddy viscosity (ν_T) values and hence to inlet turbulence intensities and length scale values.
- The parameters of the Case 2 (refer Table 4.5), (with parameters $\nu_T = 3 \times 10^{-4}, k = 10^{-3} \& \epsilon = 3 \times 10^{-4}$) is chosen as the best fit for the validation.

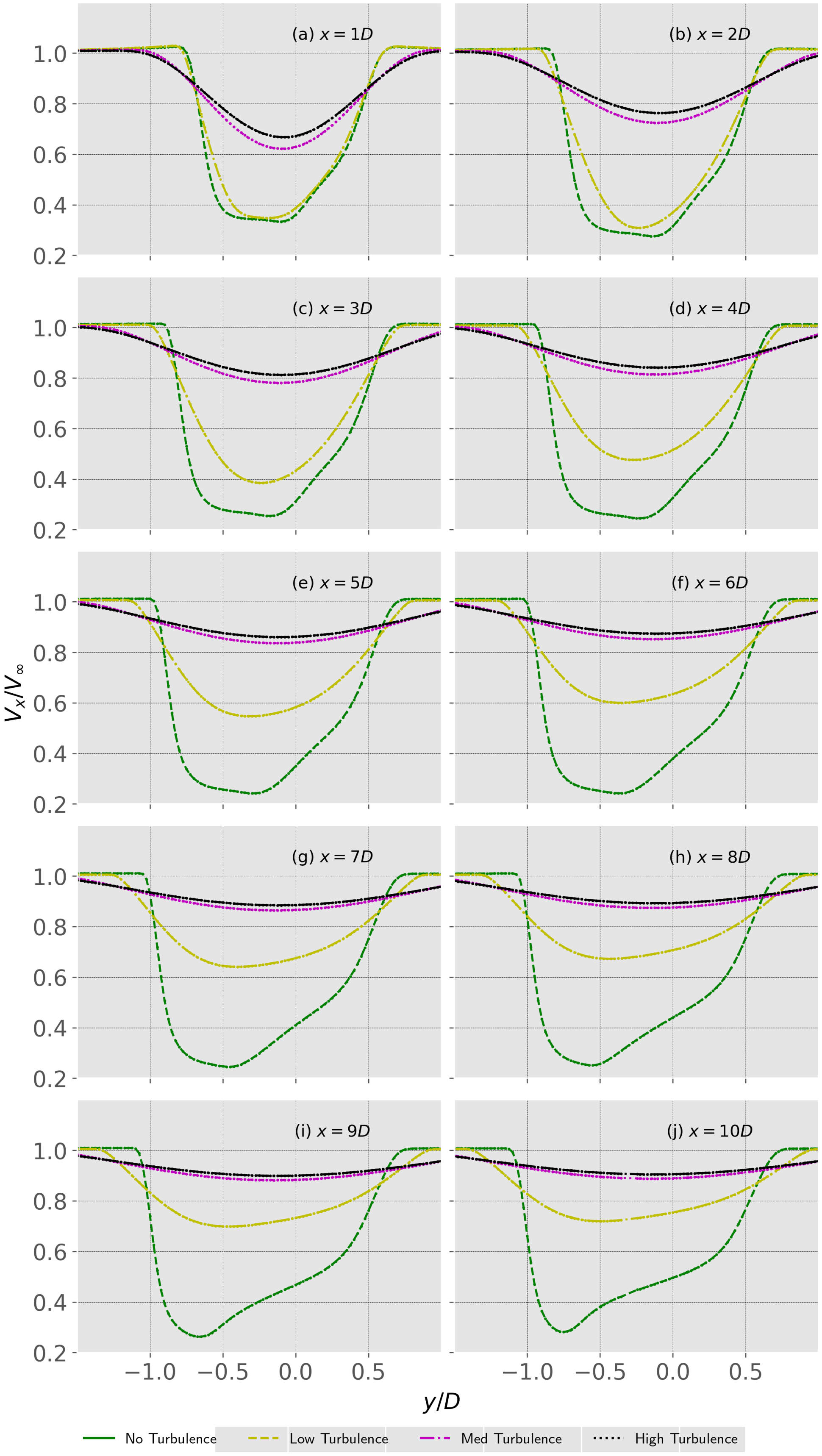

Figure 4.15: A comparison of the wake profiles at the mid-span sections for different cases of the dynamic stall models and the experimental data. The axis is non-dimensionalized with rotor diameter ($D = 0.3m$) and velocity with freestream wind speed ($V_\infty = 5ms^{-1}$)

5 VALIDATION

This chapter addresses the two final research questions, which are:

- The effect of blade pitching on the turbine performance and wake.
- Comparison of the wake velocity field with experimental data.

The three cases of the blade pitch angles (β), along with their corresponding mean power ($C_{p,avg10}$) and thrust ($C_{t,avg10}$) coefficient values averaged over the last 10 rotations of the turbine, are shown in Table 5.1. At the outset, the turbine performance is evaluated for these cases in Section 5.1. The baseline case results and subsequent validation with the experimental results are presented in Section 5.2. The wake deflection case results are validated in Section 5.3 and Section 5.4.

Cases	Blade pitch angle (β)	$C_{p,avg10}$	$C_{t,avg10}$
Baseline case	0°	0.129	0.630
Pitched case 1	$+10^\circ$	-0.543	0.498
Pitched case 2	-10°	0.088	0.519

Table 5.1: The simulation cases of wake deflection with varying blade pitch angles (β) are validated against the experimental results. All the cases are simulated with B-L-SGC dynamic stall model and standard-KE turbulence model. The mean values of power ($C_{p,avg10}$) and thrust ($C_{t,avg10}$) coefficients are calculated by averaging the corresponding instantaneous values over the last 10 rotations of the turbine.

5.1 TURBINE PERFORMANCE

The blade pitch angle (β) is the angle the chord line of the blade makes with the tangent to its path. Physically, when the blade is pitched with a positive pitch angle ('nose-up' movement), it has an effect of advancing the AOA, whereas a negative pitch angle ('nose-down' movement), has a receding effect on the AOA. This can be clearly observed in Figure 5.1e. In the positive pitch case, the blade experiences the AOA in the range of -3.6° to $+33^\circ$, whereas the negative pitch case experiences an AOA variation in the range -22.3° to 22.2°. The baseline case with 0° pitch angle reaches a maximum AOA of 26.9° and a minimum of -12.7° in one rotation of the blade. Thus the blade pitch angle has a significant impact on the turbine performance as seen in the mean $C_{p,avg10}$ and $C_{t,avg10}$ values shown in Table 5.1. The instantaneous values of C_p seen in Figure 5.1a for the case of $\beta = +10^\circ$, show that these values stay negative throughout the rotation of the blade. This indicates that the energy is in fact, imparted on the flow rather than being extracted. In the case of $\beta = -10^\circ$ the occurrence of peak instantaneous power and thrust coefficients are delayed and smaller in magnitude than the baseline case. The peak values of instantaneous power and thrust for the negative blade pitch angle case are noted to be $C_{p,max} = 0.37$ and $C_{t,max} = 1.06$ which represents a 26% reduction in maximum power and 20% decrease in maximum thrust compared to baseline case. This reduction in power coefficient for the pitched cases can be explained by considering the fact that, the blade no longer aligns with the maximum relative velocity vector at the optimal angle of attack with the change in β.

The azimuthal angle at which these peak power and thrust are also different, with the positive pitch case reaching a peak power earlier and with the negative pitch case reaching the peak power later, in comparison with the baseline case. A look at the instantaneous C_l and C_d graphs of a single blade over one rotation give a very clear picture of the physical scenario. The positive pitch case has a higher AOA at $\theta = 0°$ and hence it reaches the stall condition earlier, with peak C_l values occurring at $\theta = 32.2°$ as shown in Figure 5.1c. The C_d values for this case are the highest as seen in Figure 5.1d. In the negative pitch case, the stall occurs much later at around $\theta = 100.5°$. The peak drag is the lowest in this case. Unsurprisingly the baseline case is in between these two scenarios with the peak C_l values occurring at $\theta = 69.3°$. It is interesting to note the behaviour of the drag curves in the downwind passage of the blade. The negative pitched case exhibits the highest drag followed by the baseline case and then the positive pitch case, which shows a near-zero value for the drag in the downwind passage. This clearly shows the effect of the blade pitch on the wake. In the positive pitch case, the occurrence of early stall means that the largest vortices occurring due to dynamic stall are shed early in the windward side and never encounter the blades in the downwind passage. In the negative pitch case, the largest vortices are shed in the upwind passage of the blade, causing higher blade-wake interactions in the downwind half, causing higher drag coefficients and larger variations in lift coefficient in the downwind passage of the blade.

To compare the onsets of stall and deep stall, Figure 5.1f and Figure 5.1h can be referred. The onset of stall occurs at the marginally different AOAs for all the cases. However, the extent of the deep stall of the different cases is largely different as the variation in AOA is significantly different for each of the cases. The stall onset occurs at $\alpha = 18.7°$ in the positive pitch case and the blade is in stall until $\alpha = 33°$, where the deep stall occurs. This clearly explains the large negative power curves of the positive pitch case. The baseline case, as expected, has the blade in stall for a longer duration than the negative pitch case. The stall onset for baseline case occurs at $\alpha = 18.4°$ and deep stall occurs at $\alpha = 26.9°$. The onset of the stall for the negative pitch case occurs at a higher AOA at $\alpha = 19.4°$ and the blade is in stall for a shorter duration until the deep stall occurs at $\alpha = 22.3°$. It can be further noted that the flow reattachment occurs at the same AOA approximately for all the cases but the azimuthal locations at which they occur are different. The flow re-attaches at a larger azimuthal angle for the positive pitch case and the opposite is true for the negative pitch case. Finally, it can be noted that the azimuthal location at which the onset of stall occurs and the duration of the blade in stall, have a significant effect on the wake and hence the wake deflection, making it important to fine-tune the dynamic stall parameters.

5.2 BASELINE CASE

In this section, the contour plots and the mid-span wake profiles obtained from the simulations for the baseline case with $\beta = 0°$, are compared with the experimental data with an aim to validate the model and discuss improvements. The contour plot and the wake profile comparisons are shown in Figure 5.2.

At the outset, with the comparison of the velocity contour plots and the wake profiles of the mid-span sections obtained from the simulations with that of the experiment the following inferences can be drawn;

1. The mid-span section blade loading is over-predicted, with a simulation showing a rounded shape in the center at $x = 1D, y = 0.5D$ as opposed to the flatter

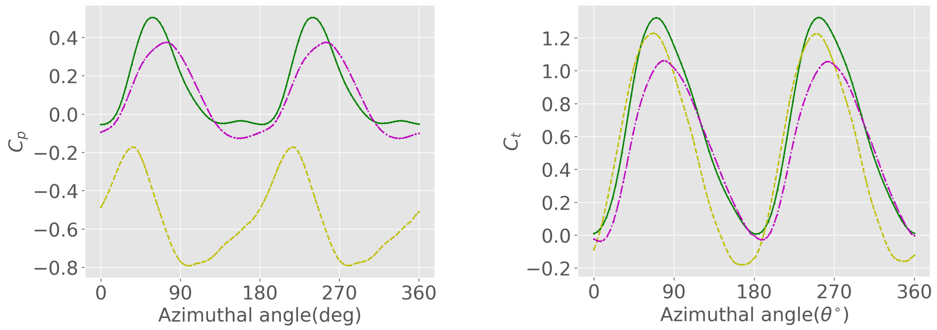

(a) Instantaneous power coefficient(C_p) of the turbine during one complete rotation.

(b) Instantaneous thrust coefficient(C_t) of the turbine during one complete rotation.

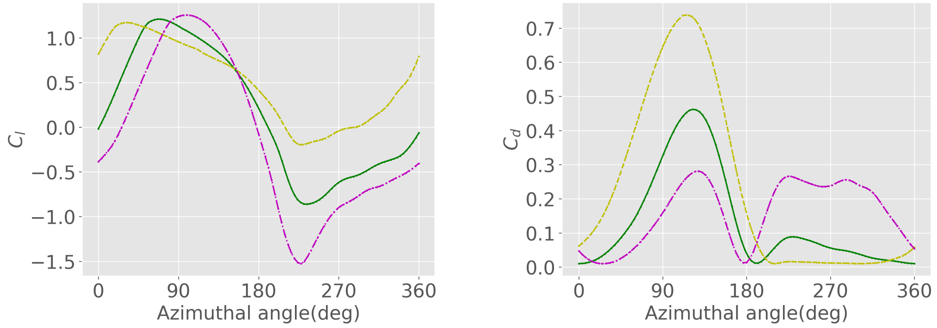

(c) Variation of the lift coefficient(C_l) during one complete rotation of the first blade, at the mid-span section.

(d) Variation of drag coefficient(C_d) during one complete rotation of the first blade, at the mid-span section.

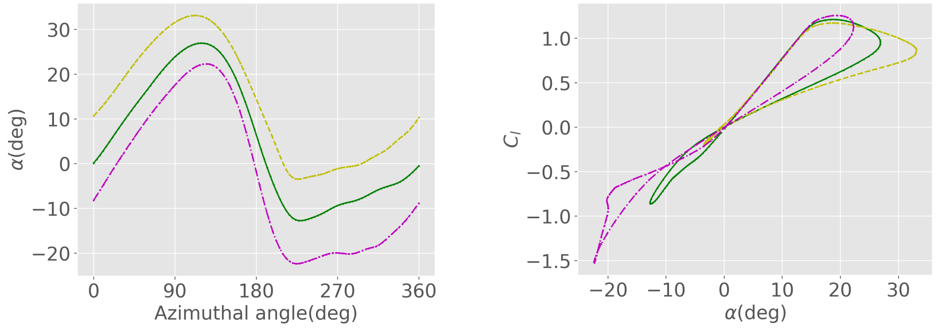

(e) Variation of AOA (α) during one complete rotation of the first blade at the mid-span section.

(f) Variation of lift coefficient(C_l) with varying AOA (α) during one complete rotation at the mid-span section.

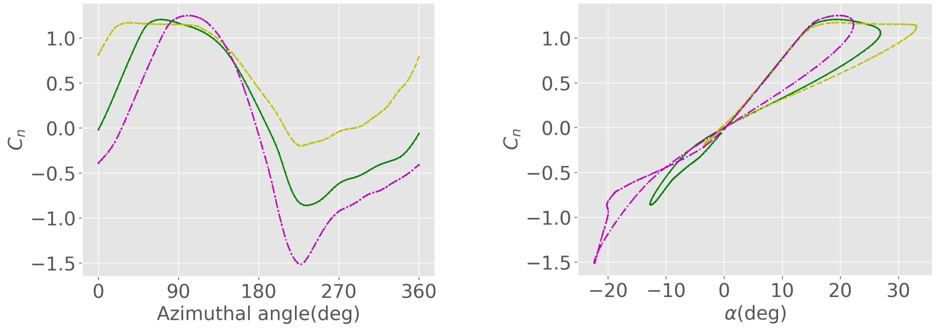

(g) Instantaneous normal force coefficient(C_n) at the mid-span section of the first blade during one complete rotation.

(h) Variation of normal coefficient(C_n) of the first blade with varying AOA (α) during one complete rotation at the mid-span section.

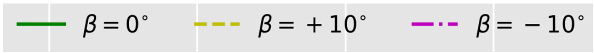

Figure 5.1: The variation of the different turbine performance parameters for the different cases of dynamic stall sensitivity study. All the parameters are ensemble-averaged over 10 rotations of the turbine.

near-wake contour seen from the experimental data (refer Figure 5.2a and Figure 5.2b).

2. The wake asymmetry is under-predicted by the simulations (comparing the symmetry of the wake profiles about $y = 0$).
3. The tip vortices are under-predicted by the simulations (refer to the sections $Z = 0.5D, -0.5D$ in Figure 5.2a and Figure 5.2b).
4. The movement of the largest wake deficits in the downward direction is under-predicted by the simulations(refer Figure 5.2e, Figure 5.2f, Figure 5.2g and Figure 5.2h).
5. The leeward side wake profile in the mid-span section matches the experimental results closely from $x = 3D$, only marginally deviating in the far wake.
6. The mean wake velocity in near-wake ($x = 1D$ to $x = 4D$), at the mid-span section, is under-predicted by 4.4% for the simulations (refer Table 5.2).
7. The mean wake recovery in the far-wake ($x = 8D$ to $x = 10D$), at the mid-span section is under-predicted by 6.4% in comparison with the experiments (refer Table 5.2).
8. The overall mean error in the prediction of the wake velocities at the mid-span section, sampled from $x = 1D$ to $x = 10D$, is 5.3%.

The larger mid-span section loading is a consequence of the azimuthal location at which the largest blade loading occurs due to dynamic stall. The largest deficits in the wake occur due to the largest blade loading. The maximum blade loading in the baseline case is predicted at $\theta = 70°$ (refer Figure 5.1g). The deficit created by the upwind blade loading can add up to the deficit created by the tower and the downwind blade loading creating a larger deficit. This can be seen in the experimental wake profile plot for $x = 1D$ where the largest deficit is seen at $y = 0.1D$ (refer Figure 5.2u). The blade loading also has a significant effect on the wake asymmetry. When the blade loading is large on the windward side and low on the leeward side, as seen for the baseline case in Figure 5.1g, the wake has larger deficits on the windward side than on the leeward side. This leads to an influx of momentum from the freestream wind on the leeward side to the deficit region on the windward side pushing the deficit further to the windward side in the downstream locations. This is clearly seen in the wake profiles of the simulation which exhibits a larger deflection towards the windward side than the experimental case. From these observations it can be concluded that the azimuthal location at which the largest blade loading is predicted for the simulations is incorrect when compared to the experiment, leading to the rounded shape of the wake deficit seen in Figure 5.2b. Further, since the largest loading on the blade occurs at the stall, it can safely be concluded that the onset of stall is predicted earlier in the simulation compared to the experiment.

The conclusion that the tip vortices are under-predicted is arrived at by comparing the shapes of the highest deficit regions (shown in dark green in Figure 5.2a and Figure 5.2b) of the simulations and experiments. This difference can either be due to the over-prediction of blade loading in the mid-span section, leading to an under-expression of the deficits arising from tip loading in the wake, or this could be a consequence of the end correction model applied that leads to under-prediction of tip loads. A definitive conclusion can only be arrived at after modifications to the simulations to correct the mid-span section loading.

The downward movement of the wake deficit is seen in the experimental data from $x = 3D$ to $x = 8D$, however, the simulations predict a wake that is symmetric about $z = 0$ axis. This is because, in the simulation the boundary condition at the bottom surface of the domain is set to be a zero gradient surface, meaning that,

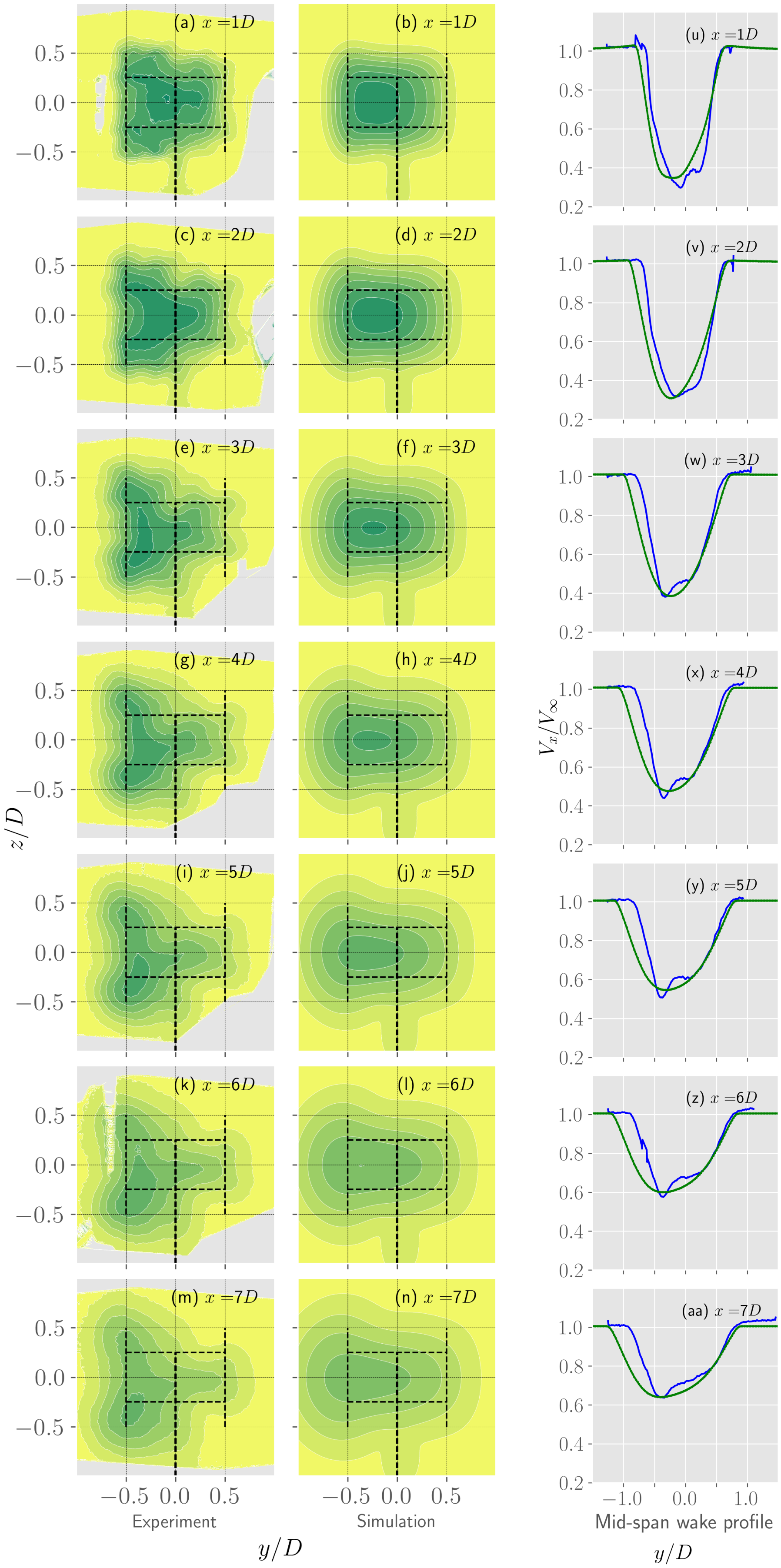
(a) $x = 1D$
(b) $x = 1D$
(u) $x = 1D$
(c) $x = 2D$
(d) $x = 2D$
(v) $x = 2D$
(e) $x = 3D$
(f) $x = 3D$
(w) $x = 3D$
(g) $x = 4D$
(h) $x = 4D$
(x) $x = 4D$
(i) $x = 5D$
(j) $x = 5D$
(y) $x = 5D$
(k) $x = 6D$
(l) $x = 6D$
(z) $x = 6D$
(m) $x = 7D$
(n) $x = 7D$
(aa) $x = 7D$
z/D
0.5
0.0
−0.5
V_x/V_∞
1.0
0.8
0.6
0.4
0.2
−0.5 0.0 0.5
Experiment
Simulation
y/D
−1.0 0.0 1.0
Mid-span wake profile
y/D

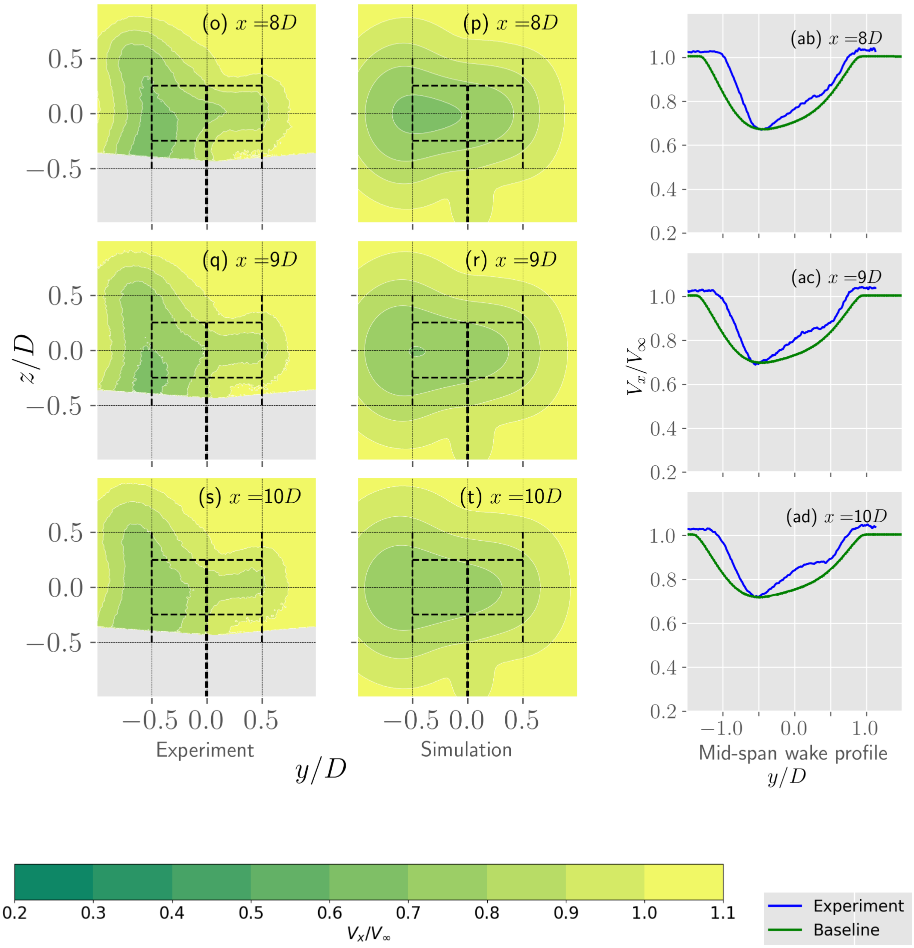

Figure 5.2: The streamwise velocity(V_x) contour at different downstream distances(x) from the turbine, from $x = 1D$ to $x = 10D$, comparing experimental results (left column), simulation results with B-L-SGC dynamic stall model and standard KE turbulence model (middle column) and the comparison of the velocities at the mid-span section (right column). The Y and Z axes are non-dimensionalized with turbine diameter ($D = 0.3m$) and the velocity is non-dimensionalized with inflow velocity ($V_\infty = 5ms^{-1}$).

there is no velocity gradient in the direction normal to the surface. However, this is not true in the real case scenario where the friction at the floor surface creates a velocity gradient normal to the floor. The downward movement of the wake deficit is caused by an uneven influx of momentum from the top and bottom surfaces.

The largest wake deficit in the experimental data, corresponding to wake velocity of $V = 0.3V_\infty$, is observed at $x = 1D, y = 0.1D$. This velocity deficit recovers to $V = 0.72V_\infty$ at $x = 10D$, while moving in the windward direction to $y = 0.55D$. The largest wake deficit in the simulation results corresponding to wake velocities of $V = 0.33V_\infty$ is seen at $x = 2D, y = 0.25D$. This deficit recovers to $V = 0.7V_\infty$ at $x = 10D$ while deflecting to $y = 0.7D$.

The mean values of the mid-span section wake velocities are calculated by averaging the total data points available from the experimental data. To compare the simulation averages on an equal basis, the simulation values are first trimmed to the Y-axis limits of the experimental data and then the mean values are calculated. These mean values are shown in Table 5.2. The least deviation in mean values of simulation from the experiment is found at $x = 1D$, with a deviation of -0.2%, meaning that the simulation marginally over-predicts the mean wake at $x = 1D$. It is interesting to note that the simulation predicts an increase in peak and mean values of wake deficits from $x = 1D$ to $x = 2D$ (comparing Figure 5.2u and Figure 5.2v;

also refer, Table 5.2). While this is not observed in the experimental results, it can be seen that the mean wake velocities remain almost constant from $x = 1D$ to $x = 2D$ for the experimental results. Further, the largest deviation from the experimental mean values occurs in the near-wake zone at $x = 6D$ with an error of 7%. The mean far-wake deviation (6.3%) is larger than the mean near-wake deviations (4.4%). The overall mean deviation is calculated by averaging the mean deviation from the experimental results at each downstream location and is found to be 5.6%.

These comparisons from the baseline case, provide a clear ground to make further comparisons for the blade pitch cases. A similar approach is followed to validate the blade pitch cases, with mean mid-span location velocities and the overall deflection of the peak velocity deficit, chosen as the validating parameters.

Case	$1D$	$2D$	$3D$	$4D$	$5D$	$6D$	$7D$	$8D$	$9D$	$10D$
Experiment	0.71	0.71	0.77	0.78	0.80	0.83	0.87	0.88	0.89	0.90
Simulation	0.71	0.67	0.72	0.73	0.75	0.77	0.82	0.83	0.84	0.85

Table 5.2: The mean non-dimensionalized velocity (V/V_∞) at the mid-span sections for each downstream location, for the baseline case of $\beta = 0°$. The values of the simulation data are averaged over Y-axis limits of the available experimental data. The experimental values are averaged after filtering outliers in the data.

5.3 PITCHED CASE 1

In this section, the results from the blade pitch angle case of $\beta = +10°$ are presented and discussed. The contour plots and mid-span section wake profile comparisons at each downstream location from $x = 1D$ to $x = 10$ are shown in Figure 5.3. The mean wake velocities for each downstream location is shown in Table 5.3 The following inferences can be made for this case:

1. The peak wake deficits in the near-wake ($x = 1D$ and $x = 2D$) are largely under-predicted (refer Figure 5.3a, Figure 5.3b, Figure 5.3c and Figure 5.3d).
2. The deflection of the peak velocity deficits are marginally over-predicted in the simulation in comparison with the experiments (refer Figure 5.3u and Figure 5.3ad).
3. The largest deviations of the mean velocity profile, in the mid-span section, is seen in the near-wake ($x = 1D$ to $x = 4D$) with a deviation of -4.8%.
4. The far-wake ($x = 8D$ to $x = 10D$) mean velocities match very well with the experiments, with a marginal deviation of 1.3%.
5. Abnormal decrease is seen in the mean mid-span velocities in the transient zone from $x = 5D$ to $x = 6D$ in the experimental results due to lack of data points (refer Table 5.3).
6. The leeward side wake velocities of the simulations, in the mid-span section, match closely to that of the experiments from $x = 5D$.
7. The mean velocities predicted at the mid-span section from the simulations, compare very well with the experiments, with a mean deviation of -1.8% and the largest error occurring at $x = 1D$, with a deviation of -10.7%.

At the outset, it is important to note that pitching the blade changes the location and magnitude of the largest wake deficits since the azimuthal location of the occurrence of the largest blade loading changes significantly as noted in Section 5.1.

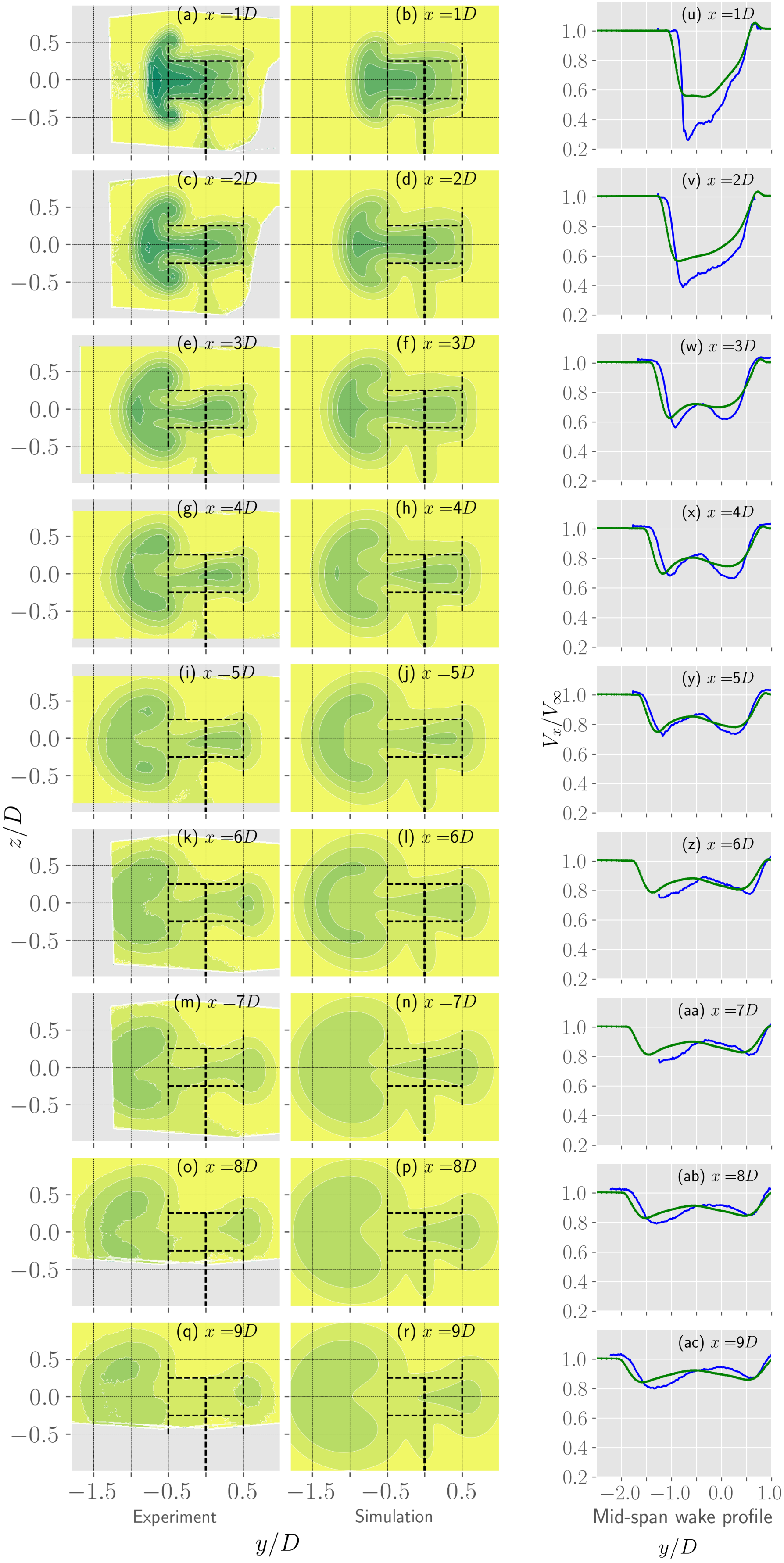
(a) $x = 1D$
(b) $x = 1D$
(u) $x = 1D$
(c) $x = 2D$
(d) $x = 2D$
(v) $x = 2D$
(e) $x = 3D$
(f) $x = 3D$
(w) $x = 3D$
(g) $x = 4D$
(h) $x = 4D$
(x) $x = 4D$
(i) $x = 5D$
(j) $x = 5D$
(y) $x = 5D$
(k) $x = 6D$
(l) $x = 6D$
(z) $x = 6D$
(m) $x = 7D$
(n) $x = 7D$
(aa) $x = 7D$
(o) $x = 8D$
(p) $x = 8D$
(ab) $x = 8D$
(q) $x = 9D$
(r) $x = 9D$
(ac) $x = 9D$
0.5
0.0
−0.5
z/D
−1.5
−0.5
0.5
Experiment
Simulation
y/D
1.0
0.8
0.6
0.4
0.2
V_x/V_∞
−2.0
−1.0
0.0
1.0
Mid-span wake profile
y/D

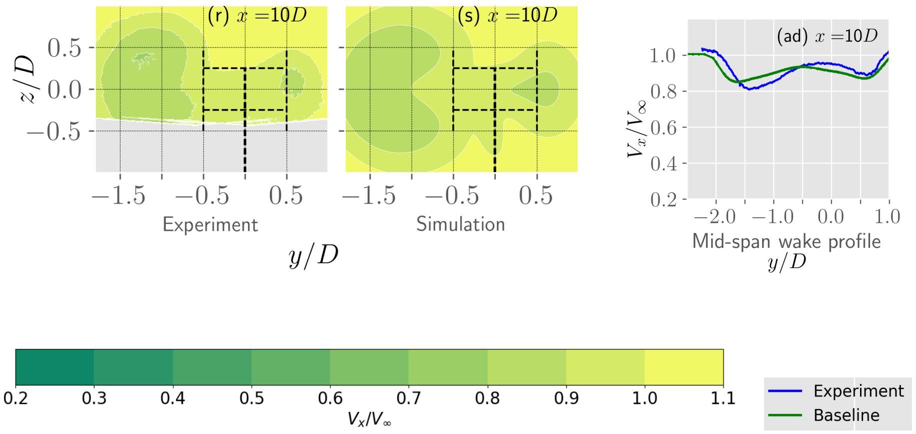

Figure 5.3: The streamwise velocity(V_x) contour at different downstream distances(x) from the turbine, from $x = 1D$ to $x = 10D$, for a blade pitch angle (β) of $+10°$. The experimental results are in the left column, simulation results with B-L-SGC dynamic stall model and standard KE turbulence model in the middle column and the comparison of the velocities at the mid-span section in the right column. The turbine is seen from downstream location. The Y and Z axes are non-dimensionalized with turbine diameter ($D = 0.3m$) and the velocity is non-dimensionalized with inflow velocity ($V_\infty = 5ms^{-1}$).

The effect of a positive pitch angle on the blade advances the occurrence of this largest blade loading. While in the baseline case the largest blade loading occurs at $\theta = 70°$, in this case, it occurs in the windward side at $\theta = 32.2°$. However, the effect of onset dynamic stall being predicted earlier by the SGC model is still seen here in the magnitude and location of the largest wake deficit. Although the dynamic stall onset is advanced, both in the experiment and the simulations, the simulation still predicts the early onset of the dynamic stall in comparison with the experiments. This conclusion can be drawn by observing the $x = 1D$ mid-span wake profile seen in Figure 5.3u. The wake profile of the simulation shows a 'U' shaped profile with a flat trough. This velocity deficit trough, seen from $y = -0.75D$ to $y = -0.25D$ in Figure 5.3u, corresponds to the rather flat C_n curve occurring after stall onset seen in Figure 5.1h. It can be further noted that the blade is in stall from $\theta = 32.2°$ to $\theta = 115°$. The wake profile of the experiments predicts this stall onset later and also more severely as reflected in its wake. It has a nearly asymmetric 'V' shaped profile seen in Figure 5.3u, and also a deeper trough with the lowest velocity reaching $V = 0.26V_\infty$. The effect of this difference in the prediction of the azimuthal location and magnitude of the largest blade loading is seen all the way in the downstream locations, right into the far-wake. The peak deficit occurring at $x = 1D, y = -0.7D$ in the experiments deflects to $y = -1.4D$ at $x = 10D$. Whereas, the peak deficit in the simulation at $x = 1D, y = -0.25D$ deflects to to $y = -1.75D$ at $x = 10D$. While the mean velocities in the far-wake at $x = 10D$ match closely with a deviation of 1.3% (refer Table 5.3), the larger peak deficit of the experiment recovers faster compared to the more smeared out deficit seen in the simulations. This reasoning explains the inferences 1, 2, 3 and 4 mentioned above.

The experimental data at $x = 6D, 7D$ are only available from $y = -1.25D$. This affects the mean values of the wake at the mid-span section as seen in Table 5.3. The mid-span wake profile of the experiment which takes an asymmetric 'V' shape at $x = 1D$ transforms into a 'W' shape by $x = 3D$. Similar behaviour is seen in the simulation wake profile. This can be explained with the following analogy. The larger deficits on the windward side are replenished by the wind, with the momentum imparted from the leeward side, which is enhanced by the tip vortices (seen as circular patches at $z = +0.5D, -0.5D$ and $y = -0.5D$ in Figure 5.3a and Figure 5.3b). While the tip vortices enhance the momentum imparted to windward side deficits, they aggravate the leeward side deficits causing a 'W' shaped wake profile.

Finally, the far-wake is well predicted except at the points of the large wake deficits. The larger wake deficits of the experiments in the near-wake take longer to recover than the smaller wake deficits of the simulations. It can be further noted that the peak deficits of the simulation and experiments recover at different rates. The lowest mid-span velocity of the wake in the experiment ($V = 0.26V_\infty$) recovers to $V = 0.81V_\infty$ at $x = 10D$, whereas the lowest mid-span velocity in the simulation ($V = 0.56V_\infty$) recovers to $V = 0.87V_\infty$ by $x = 10D$. This is in line with the literature, where the larger wake deficits are observed to recover faster, although seen in a different context (Hezaveh et al., 2017; Zou et al., 2020).

Case	$1D$	$2D$	$3D$	$4D$	$5D$	$6D$	$7D$	$8D$	$9D$	$10D$
Experiment	0.68	0.63	0.84	0.87	0.88	0.87	0.89	0.91	0.91	0.92
Simulation	0.75	0.70	0.83	0.86	0.87	0.89	0.90	0.90	0.90	0.91

Table 5.3: The mean non-dimensionalized velocity (V/V_∞) at the mid-span sections for each downstream location. The values of the simulation data are averaged over Y-axis limits of the available experimental data. The experimental values are averaged after filtering outliers in the data.

5.4 PITCHED CASE 2

This section presents the results from the blade pitch angle case of $\beta = -10°$ in comparison with the experiments. The contour plots and mid-span wake profile comparisons at each downstream location from $x = 1D$ to $x = 10$ are shown in Figure 5.4. The mean wake velocities for each downstream location is shown in Table 5.4. The following inferences can be made for this case:

1. The wake deflection predicted by the simulation is contrary to the experimental data (refer $x = 1D$ to $x = 10D$), with the experiment showing a windward side deflection and simulation showing a deflection towards the leeward side.
2. The peak mid-span wake deficits predicted by the simulation at $x = 1D$ is larger and more localized(refer Figure 5.4u) whereas the mean mid-span wake deficit predicted by the simulation is lower by 2.1% (refer Table 5.4).
3. The mid-span section wake profile does not match on both, windward and leeward sides.
4. The windward side wake deficits are under-predicted by the simulation.
5. The mean near-wake ($x = 1D$ to $x = 4D$) deficits are under-predicted by the simulation by 2%.
6. The mean far-wake ($x = 8D$ to $x = 10D$) deficits are over-predicted by the simulation by 2.6%.
7. The overall mean error in predicting the wake profile at the mid-span section is -0.9% with a maximum mean error of 5.3% occurring at $x = 2D$.

In the case of the negative pitch angle, the maximum blade loading occurs in the upwind section. The effect of a negative pitch angle has a receding effect on the onset of stall, with the simulation predicting the largest blade loading to occur at around $\theta = 100.4°$. The blade is in stall for a very short duration compared to both the baseline case and the positive pitched case. The deep 'V' shaped trough seen in

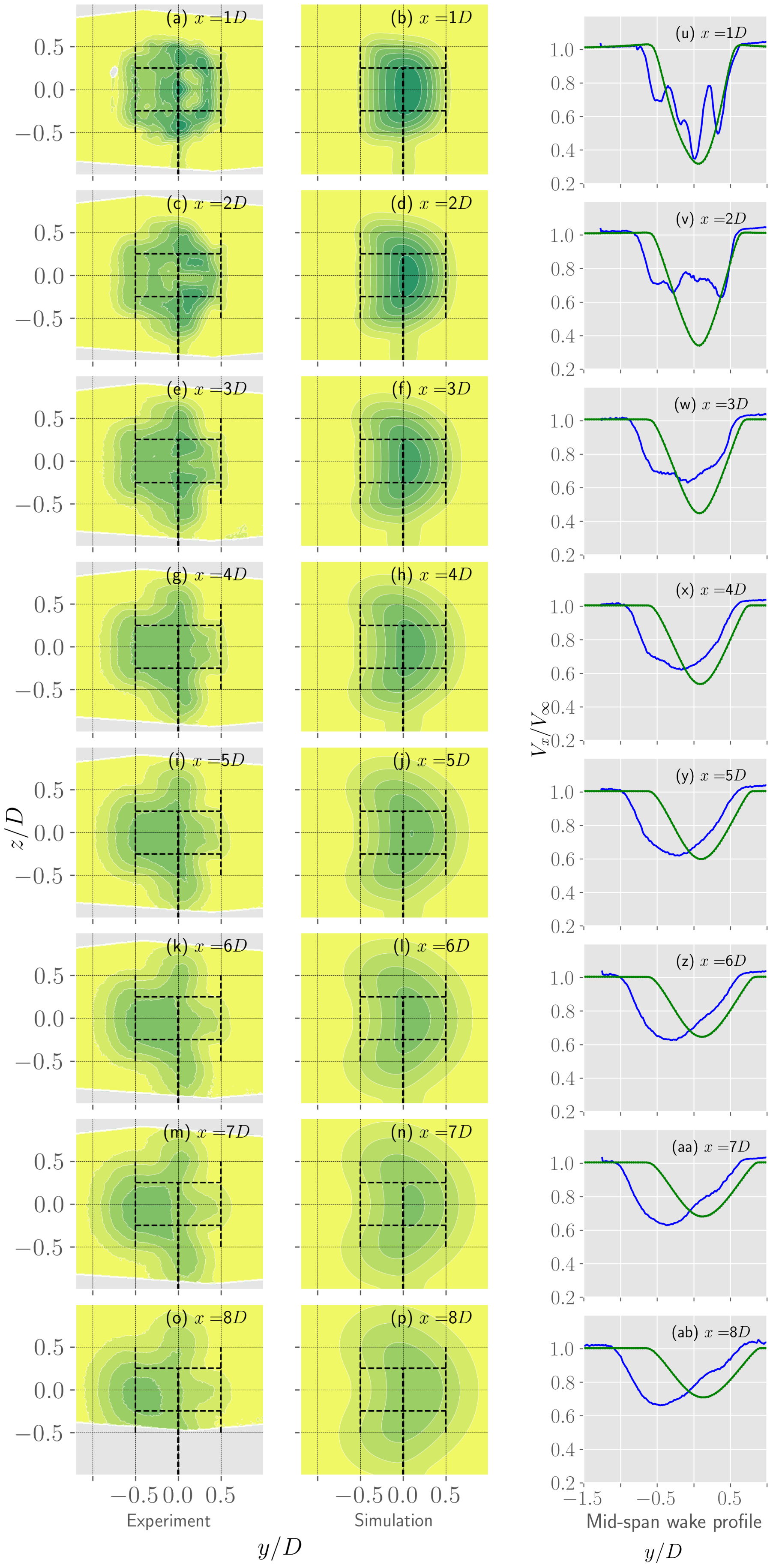
(a) $x = 1D$
(b) $x = 1D$
(u) $x = 1D$
(c) $x = 2D$
(d) $x = 2D$
(v) $x = 2D$
(e) $x = 3D$
(f) $x = 3D$
(w) $x = 3D$
(g) $x = 4D$
(h) $x = 4D$
(x) $x = 4D$
(i) $x = 5D$
(j) $x = 5D$
(y) $x = 5D$
(k) $x = 6D$
(l) $x = 6D$
(z) $x = 6D$
(m) $x = 7D$
(n) $x = 7D$
(aa) $x = 7D$
(o) $x = 8D$
(p) $x = 8D$
(ab) $x = 8D$
0.5
0.0
−0.5
z/D
1.0
0.8
0.6
0.4
0.2
V_x/V_∞
−0.5 0.0 0.5
Experiment
Simulation
y/D
−1.5
−0.5
0.5
Mid-span wake profile
y/D

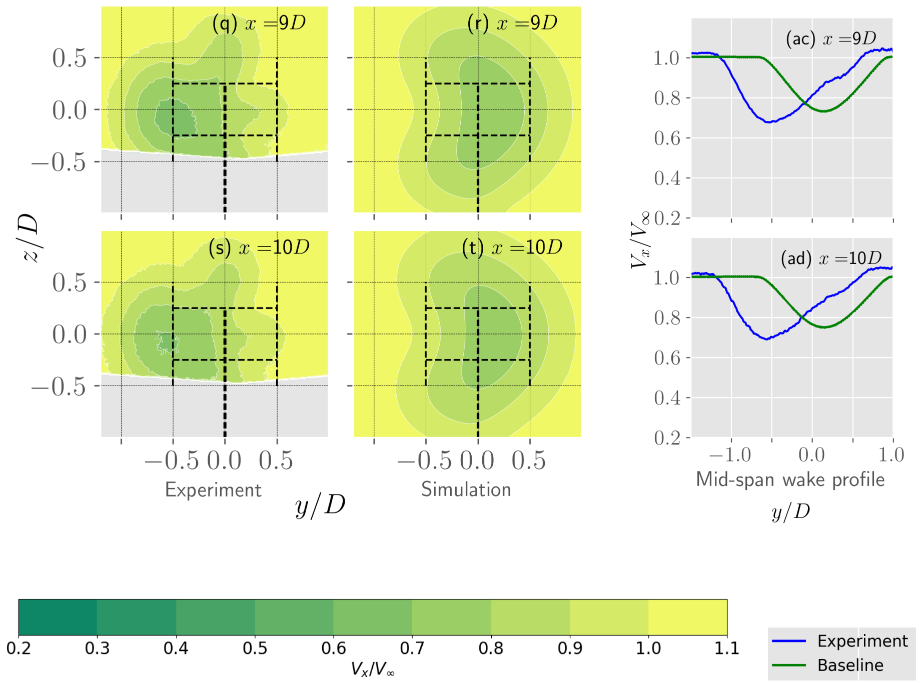

Figure 5.4: The streamwise velocity(V_x) contour at different downstream distances(x) from the turbine, from $x = 1D$ to $x = 10D$, for a blade pitch angle (β) of $-10°$. The experimental results are in the left column, simulation results with B-L-SGC dynamic stall model and standard KE turbulence model in the middle column and the comparison of the velocities at the mid-span section in the right column. The turbine is seen from $-X$ direction. The Y and Z axes are non-dimensionalized with turbine diameter ($D = 0.3m$) and the velocity is non-dimensionalized with inflow velocity ($V_\infty = 5ms^{-1}$).

the wake at $x = 1D$ (shown in Figure 5.4u) corresponds to the large blade loading occurring at stall. A comparison of the contour plots of the simulation (Figure 5.4a) and experiment (Figure 5.4b) at $x = 1D$ shows an interesting difference. The wake deficit predicted by the simulation appears to be concentrated at $y = 0$ whereas the experimental data shows a rather smeared distribution of the wake deficits from $y = 0$ to $y = 0.25D$. To explain this, several factors must be taken into consideration. Firstly the occurrence of the largest blade loading and the duration of the blade in stall has an effect on where the largest deficit is seen in the wake. In the case of the simulation, the stall occurs in the upwind location, whereas, in the experiment, it seems to have occurred earlier, contrary to the observation in the previous cases. Secondly, the duration for which the blade is in stall appears to have an effect on the peak deficits seen in the wake. To confirm this, a comparison of the wake deficits and α versus C_n curves for the three, blade pitch angle cases ($\beta = -10°, 0°, +10°$) can be used. In the positive pitch angle case, the blade is in stall for the longest duration among the three cases and the C_n values are nearly a constant during stall (Figure 5.1g). This results in a 'U' shaped wake profile with a nearly flat long trough from $y = -0.75D$ to $y = -0.25D$ seen in Figure 5.3u. In the baseline case, the blade is in stall for a shorter duration with the C_n curve having a low negative slope in stall. This leads to a 'U' shaped profile but now with a shorter trough from $y = -0.45D$ to $y = -0.05D$ seen in Figure 5.2u. The negative pitch case is in stall for a much shorter duration and has a rounded C_n curve leading to a sharper 'V' shaped curve. Thirdly, the shed wake in the negative pitch case has higher blade-wake interactions and a higher chance of the deficits getting added to the tower wake which could explain the smeared out troughs with a large wake deficit seen in Figure 5.4u at $y = 0$. Finally, the crests seen in Figure 5.4u, can be explained by the Magnus effect of the tower which is absent in the simulation as the tower is modelled as a cylinder with zero lift and non-zero drag coefficient. While all the effects contribute to the deviation from the experimental results stated in point 1, the major influencing parameter is still the azimuthal location at which the largest blade loading occurs and the duration of the blade in stall.

The inferences drawn in points 2, 3, 4 and 5 can all be explained as the consequence of the above-mentioned phenomena. The over-prediction of recovery in the far wake by the simulation can be explained with the larger deficit leading to faster recovery as seen in the positive pitch case for the experimental results.

In conclusion, it can be said that the results of the negative pitch case do not entirely match the experimental data although the mean velocity at the mid-span section matches closely. The prediction of wake deflection of the peak deficit predicted by the simulation deviates from the experimental results by $0.75D$.

Case	$1D$	$2D$	$3D$	$4D$	$5D$	$6D$	$7D$	$8D$	$9D$	$10D$
Experiment	0.86	0.89	0.87	0.87	0.87	0.87	0.87	0.88	0.89	0.90
Simulation	0.85	0.85	0.86	0.88	0.89	0.90	0.90	0.91	0.91	0.92

Table 5.4: The mean non-dimensionalized velocity (V/V_∞) at the mid-span sections for each downstream location. The values of the simulation data are averaged over Y-axis limits of the available experimental data. The experimental values are averaged after filtering outliers in the data.

6 CONCLUSIONS

The main results of the study, along with a brief description of the simulation details are summarized in this chapter. At the outset, the actuator line model (ALM) of the rotor with URANS flow model, standard KE turbulence model (Launder and Spalding, 1974), B-L-SGC dynamic stall model (Sheng et al., 2008), Goude flow curvature model (Goude, 2012), added mass model (Strickland et al., 1979) and a tip correction model (Bachant et al., 2016), was chosen to model the VAWT wake and its deflection. The baseline case of $\beta = 0°$ was used to study the effects of dynamic stall and turbulence. The wake deflection using a VAWT with two cases of blade pitch angles ($\beta = +10°$ and $-10°$) were simulated and validated against experimental data. Below are the conclusions of the study:

1. Simulation parameters
    - The mesh topology, the time step settings and the ensemble averaging period are detrimental to the accuracy of the URANS simulation results.
    - The spatial and temporal sensitivity decrease with decreased mesh size and time step values respectively. This is in line with the observations of Bachant and Wosnik (2016); Mendoza et al. (2019).
2. Dynamic stall sensitivity
    - The dynamic stall model and hence its parameters have a significant impact on instantaneous blade loading.
    - The magnitude and the azimuthal location of the largest blade loading has a significant impact on the wake velocity deficits, asymmetry and wake recovery rates.
    - Hence the parameters of the dynamic stall model have a considerable impact on the wake properties.
    - The empirical constants used to model the dynamic stall in this study, predict an early onset compared to the experiments.
3. KE turbulence model sensitivity
    - The standard KE model is highly sensitive to initialized turbulent kinetic energy (k) and turbulent dissipation (ϵ) values and hence, the initialized eddy viscosity (ν_T) values.
    - The deep stall AOA and the duration of the blades in stall marginally decrease with an increase in ν_T values.
    - The wake recovery rates and wake expansion are significantly enhanced by increasing the inlet turbulence intensities and length scales.
    - The power and thrust coefficients increase with an increase in ν_T values while the wake velocity deficits in the near-wake significantly decrease with an increase in ν_T values.
4. Wake deflection
    - Wake deflection due to blade pitching is a consequence of asymmetry in the wake. This asymmetry is caused due to the large, localized velocity deficits and a momentum transfer from the freestream wind to the deficit region.

  - The direction of deflection of the wake depends on the location of the largest velocity deficits in the wake and hence, the azimuthal location at which maximum blade loads occur.
  - Larger near-wake velocity deficits recover faster for a given inlet turbulence intensity and length scale.

5. Effect of blade pitching on turbine performance
    - The positive pitch case with $\beta = +10^\circ$, predicts a mean negative power coefficient which is 518.6% lower than the baseline case.
    - The negative pitch case with $\beta = -10^\circ$, predicts a 31.7% lower mean power coefficient than the baseline case.
6. Validation results
    - The overall mean error in prediction of the wake velocities in the mid-span section, for the baseline case is 5.6% in comparison with the experiments.
    - The dynamic stall in the case of positive pitch is advanced creating larger loading and larger deficits on the windward side. Whereas, for the negative pitch case the dynamic stall is delayed leading to the wake deflecting to the leeward side.
    - The positive blade pitch angle case shows good agreement with the experimental results with a mean absolute error of less than 2%. The prediction of wake deflection is in line with the experimental data with marginal deviation.
    - The case with negative blade pitch angle significantly deviates from the experimental data in predicting the direction of wake deflection (by 85%), although the mid-span mean velocities in the wake have a marginal deviation.
    - The incorrect prediction of wake deflection in $\beta = -10^\circ$ case can be attributed to the azimuthal location of the onset of dynamic stall, the duration of the blade in stall and the Magnus effect of the tower (which is neglected in the simulations).
7. Improvements to the model
    - For better accuracy, the onset and the duration of the blade in dynamic stall need to be corrected.
    - The inlet turbulence intensity and the length scale value needs to be further tuned.
    - Magnus effect of the tower can be included by including a lift coefficient to the tower parameters.

In conclusion, the simulation of wake deflection with URANS ALM agrees well with the experiments except in the negative blade pitch angle case. The KE turbulence model can predict wake velocity profile with marginal deviation when the inlet parameters are chosen well. The SGC-B-L DS model can be improved to match the experimental results better.

BIBLIOGRAPHY

Araya, D. B., Colonius, T., and Dabiri, J. O. (2017). Transition to bluff-body dynamics in the wake of vertical-axis wind turbines. *Journal of Fluid Mechanics*, 813:346–381.

Bachant, P., Goude, A., daa mec, and Wosnik, M. (2019). turbinesfoam/turbinesfoam: v0.1.1.

Bachant, P., Goude, A., and Wosnik, M. (2016). Actuator line modeling of vertical-axis turbines. *arXiv preprint arXiv:1605.01449*.

Bachant, P., Goude, A., and Wosnik, M. (2018). Actuator line modeling of vertical-axis turbines.

Bachant, P. and Wosnik, M. (2015). Characterising the near-wake of a cross-flow turbine. *Journal of Turbulence*, 16(4):392–410.

Bachant, P. and Wosnik, M. (2016). Modeling the near-wake of a vertical-axis cross-flow turbine with 2-d and 3-d rans. *Journal of Renewable and Sustainable Energy*, 8(5):053311.

Baerwald, E. F., D'Amours, G. H., Klug, B. J., and Barclay, R. M. (2008). Barotrauma is a significant cause of bat fatalities at wind turbines. *Current biology*, 18(16):R695–R696.

Balduzzi, F., Bianchini, A., Maleci, R., Ferrara, G., and Ferrari, L. (2016). Critical issues in the cfd simulation of darrieus wind turbines. *Renewable Energy*, 85:419–435.

Barnes, A., Marshall-Cross, D., and Hughes, B. R. (2021). Validation and comparison of turbulence models for predicting wakes of vertical axis wind turbines. *Journal of Ocean Engineering and Marine Energy*, pages 1–24.

Batchelor, G. K. (2000). *An Introduction to Fluid Dynamics*. Cambridge Mathematical Library. Cambridge University Press.

Beddoes, T. (1993). A third generation model for unsteady aerodynamics and dynamic stall. *Westland Helicopter Limited, RP-908*.

Berg, D. E. (1983). Improved double-multiple streamtube model for the darrieus-type vertical axis wind turbine. In *Presented at the Am. Solar Energy Soc. Meeting*.

Beri, H., Yao, Y., et al. (2011). Double multiple streamtube model and numerical analysis of vertical axis wind turbine. *Energy and Power Engineering*, 3(03):262.

Borg, M., Shires, A., and Collu, M. (2014). Offshore floating vertical axis wind turbines, dynamics modelling state of the art. part i: Aerodynamics. *Renewable and Sustainable Energy Reviews*, 39:1214–1225.

Carbó Molina, A., Bartoli, G., and De Troyer, T. (2018). Generation of uniform turbulence profiles in the wind tunnel for urban vawt testing. In Battisti, L. and Ricci, M., editors, *Wind Energy Exploitation in Urban Environment*, pages 27–43, Cham. Springer International Publishing.

Chowdhury, A. M., Akimoto, H., and Hara, Y. (2016). Comparative cfd analysis of vertical axis wind turbine in upright and tilted configuration. *Renewable Energy*, 85:327–337.

Courant, R., Friedrichs, K., and Lewy, H. (1967). On the partial difference equations of mathematical physics. *IBM journal of Research and Development*, 11(2):215–234.

Dabiri, J. (2010). Potential order-of-magnitude enhancement of wind farm power density via counter-rotating vertical-axis wind turbine arrays. *Journal of Renewable and Sustainable Energy*, 3.

Dacles-Mariani, J., Zilliac, G. G., Chow, J. S., and Bradshaw, P. (1995). Numerical/experimental study of a wingtip vortex in the near field. *AIAA Journal*, 33(9):1561–1568.

De Tavernier, D. (2021). *Aerodynamic advances in vertical-axis wind turbines*. Phd thesis, Delft University of Techology, Delft,Netherlands.

De Tavernier, D., Sakib, M., Griffith, T., Pirrung, G., Paulsen, U., Madsen, H., Keijer, W., and Ferreira, C. (2020). Comparison of 3d aerodynamic models for vertical-axis wind turbines: H-rotor and ϕ-rotor. In *Journal of Physics: Conference Series*, volume 1618, page 052041. IOP Publishing.

Douak, M., Aouachria, Z., Rabehi, R., and Allam, N. (2018). Wind energy systems: Analysis of the self-starting physics of vertical axis wind turbine. *Renewable and Sustainable Energy Reviews*, 81:1602–1610.

Dyachuk, E. and Goude, A. (2015). Simulating dynamic stall effects for vertical axis wind turbines applying a double multiple streamtube model. *Energies*, 8(2):1353–1372.

Dyachuk, E., Goude, A., and Bernhoff, H. (2014). Dynamic stall modeling for the conditions of vertical axis wind turbines. *AIAA journal*, 52(1):72–81.

Erfort, G., von Backström, T. W., and Venter, G. (2020). Reduction in the torque ripple of a vertical axis wind turbine through foil pitching optimization. *Wind Engineering*, 44(2):115–124.

Fadil, J., Soedibyo, and Ashari, M. (2017). Performance comparison of vertical axis and horizontal axis wind turbines to get optimum power output. In *2017 15th International Conference on Quality in Research (QiR) : International Symposium on Electrical and Computer Engineering*, pages 429–433.

Ferreira, C., Bijl, H., van Bussel, G., and Kuik, G. (2007). Simulating dynamic stall in a 2d vawt: Modeling strategy, verification and validation with particle image velocimetry data. *Journal of Physics: Conference Series, 75 (1)*, 75.

Ferreira, C., Hofemann, C., Dixon, K., Kuik, G., and van Bussel, G. (2010). 3-d wake dynamics of the vawt: Experimental and numerical investigation.

Ferreira, C. S. (2009). *The near wake of the VAWT 2D and 3D views of the VAWT aerodynamics*. Phd thesis, Delft University of Techology, Delft,Netherlands.

Ferreira, C. S., Madsen, H. A., Barone, M., Roscher, B., Deglaire, P., and Arduin, I. (2014). Comparison of aerodynamic models for vertical axis wind turbines. In *Journal of Physics: Conference Series*, volume 524, page 012125. IOP Publishing.

Ferreira, C. S. and Scheurich, F. (2011). Proving that power and instantaneous loads and decoupled on a 2d vertical axis wind turbine. In *Wake conference*, pages 139–144. Gotland university.

Glauert, H. (1935). *Airplane Propellers*, pages 169–360. Springer Berlin Heidelberg, Berlin, Heidelberg.

Gormont, R. E. (1973). A mathematical model of unsteady aerodynamics and radial flow for application to helicopter rotors. Technical report, Boeing Vertol Co Philadelphia Pa.

Goude, A. (2012). *Fluid mechanics of vertical axis turbines: Simulations and model development*. PhD thesis, Acta Universitatis Upsaliensis.

Griffith, D., Paquette, J., Barone, M., Goupee, A., Fowler, M., Bull, D., and Owens, B. (2016). A study of rotor and platform design trade-offs for large-scale floating vertical axis wind turbines. *Journal of Physics: Conference Series*, 753.

Hand, B., Cashman, A., and Kelly, G. (2015). An aerodynamic modelling methodology for an offshore floating vertical axis wind turbine. In *2015 International Conference on Renewable Energy Research and Applications (ICRERA)*, pages 273–277.

Hau, E. (2006). *Wind Turbines - Fundamentals,Technologies,Application,Economics*. Springer.

Hau, N. R., Ma, L., Ingham, D., and Pourkashanian, M. (2020). A critical analysis of the stall onset in vertical axis wind turbines. *Journal of Wind Engineering and Industrial Aerodynamics*, 204:104264.

He, J., Jin, X., Xie, S., Cao, L., Wang, Y., Lin, Y., and Wang, N. (2020). Cfd modeling of varying complexity for aerodynamic analysis of h-vertical axis wind turbines. *Renewable Energy*, 145:2658–2670.

Hezaveh, S. H., Bou-Zeid, E., Dabiri, J., Kinzel, M., Cortina, G., and Martinelli, L. (2018). Increasing the power production of vertical-axis wind-turbine farms using synergistic clustering. *Boundary-Layer Meteorology*, 169.

Hezaveh, S. H., Bou-Zeid, E., Lohry, M. W., and Martinelli, L. (2017). Simulation and wake analysis of a single vertical axis wind turbine. *Wind Energy*, 20(4):713–730.

Howland, M. F., Lele, S. K., and Dabiri, J. O. (2019). Wind farm power optimization through wake steering. *Proceedings of the National Academy of Sciences*, 116(29):14495–14500.

Huang, M., Ferreira, C., Sciacchitano, A., and Scarano, F. (2020). Experimental comparison of the wake of a vertical axis wind turbine and planar actuator surfaces. *Journal of Physics: Conference Series*, 1618(5). Science of Making Torque from Wind 2020, TORQUE 2020 ; Conference date: 28-09-2020 Through 02-10-2020.

IRENA (2019). Future of wind: Deployment, investment, technology, grid integration and socio-economic aspects (a global energy transformation paper).

Kaldellis, J. K. and Zafirakis, D. (2011). The wind energy (r)evolution: A short review of a long history. *Renewable Energy*, 36(7):1887–1901.

Katopodes, N. D. (2019). Chapter 8 - turbulent flow. In Katopodes, N. D., editor, *Free-Surface Flow*, pages 566–650. Butterworth-Heinemann.

Katz, J. and Plotkin, A. (2001). *Low-Speed Aerodynamics*. Cambridge Aerospace Series. Cambridge University Press, 2 edition.

Keisar, D., De Troyer, T., and Greenblatt, D. (2020). Concept and operation of a wind turbine driven by dynamic stall. *AIAA Journal*, 58(6):2370–2376.

Kinzel, M., Mulligan, Q., and Dabiri, J. O. (2012). Energy exchange in an array of vertical-axis wind turbines. *Journal of Turbulence*, 13(1):N38.

Kumar, R., Raahemifar, K., and Fung, A. S. (2018). A critical review of vertical axis wind turbines for urban applications. *Renewable and Sustainable Energy Reviews*, 89:281–291.

Lam, H. and Peng, H. (2016). Study of wake characteristics of a vertical axis wind turbine by two- and three-dimensional computational fluid dynamics simulations. *Renewable Energy*, 90:386–398.

Laneville, A. and Vittecoq, P. (1986). Dynamic stall: The case of the vertical axis wind turbine.

Launder, B. and Sharma, B. (1974). Application of the energy-dissipation model of turbulence to the calculation of flow near a spinning disc. *Letters in Heat and Mass Transfer*, 1(2):131–137.

Launder, B. and Spalding, D. (1974). The numerical computation of turbulent flows. *Computer Methods in Applied Mechanics and Engineering*, 3(2):269–289.

Leishman, J. and Beddoes, T. (1986). A generalised model for airfoil unsteady aerodynamic behaviour and dynamic stall using the indicial method. In *Proceedings of the 42nd Annual forum of the American Helicopter Society*, pages 243–265. Washington DC.

Madsen, H. (1982). *The Actuator Cylinder - A Flow Model for Vertical Axis Wind Turbines*. PhD thesis.

Madsen, H., Larsen, T., Vita, L., and Paulsen, U. (2013). Implementation of the actuator cylinder flow model in the hawc2 code for aeroelastic simulations on vertical axis wind turbines.

Massé, B. (1981). *Description de deux programmes d'ordinateur pour le calcul des performances et des charges aerodynamiques pour les eoliennes a axe vertical*. Institut de recherche de l'Hydro-Québec.

Masson, C., Leclerc, C., and Paraschivoiu, I. (1998). Appropriate dynamic-stall models for performance predictions of vawts with nlf blades. *International Journal of Rotating Machinery*, 4(2):129–139.

McIntosh, S. C., Babinsky, H., and Bertényi, T. (2009). Convergence Failure and Stall Hysteresis in Actuator-Disk Momentum Models Applied to Vertical Axis Wind Turbines. *Journal of Solar Energy Engineering*, 131(3). 034502.

Mendoza, V., Bachant, P., Ferreira, C., and Goude, A. (2019). Near-wake flow simulation of a vertical axis turbine using an actuator line model. *Wind Energy*, 22(2):171–188.

Mendoza, V. and Goude, A. (2019). Improving farm efficiency of interacting vertical-axis wind turbines through wake deflection using pitched struts. *Wind Energy*, 22(4):538–546.

Menter, F., Esch, T., and Kubacki, S. (2002). Transition modelling based on local variables. In RODI, W. and FUEYO, N., editors, *Engineering Turbulence Modelling and Experiments 5*, pages 555–564. Elsevier Science Ltd, Oxford.

Menter, F. R. (1994). Two-equation eddy-viscosity turbulence models for engineering applications. *AIAA Journal*, 32(8):1598–1605.

Menter, F. R., Langtry, R. B., Likki, S. R., Suzen, Y. B., Huang, P. G., and Völker, S. (2004). A Correlation-Based Transition Model Using Local Variables—Part I: Model Formulation. *Journal of Turbomachinery*, 128(3):413–422.

Mertens, S., Kuik, G., and van Bussel, G. (2003). Performance of an h-darrieus in the skewed flow on a roof. *Journal of Solar Energy Engineering-transactions of The Asme - J SOL ENERGY ENG*, 125.

Micallef, D. and Sant, T. (2016). *A Review of Wind Turbine Yaw Aerodynamics*, pages 27–53.

Migliore, P., Wolfe, W., and Fanucci, J. (1980). Flow curvature effects on darrieus turbine blade aerodynamics. *Journal of Energy*, 4(2):49–55.

Muraca, R. J., Stephens, M. V., and Dagenhart, J. R. (1975). Theoretical performance of cross-wind axis turbines with results for a catenary vertical axis configuration.

Murray, J. and Barone, M. (2011). The development of cactus, a wind and marine turbine performance simulation code. In *49th AIAA Aerospace Sciences Meeting including the New Horizons Forum and Aerospace Exposition*, page 147.

Paraschivoiu, I. (1988). Double-multiple streamtube model for studying vertical-axis wind turbines. *Journal of Propulsion and Power*, 4(4):370–377.

Paraschivoiu, I. (2002). *Wind Turbine Design: With Emphasis on Darrieus Concept*. Polytechnic International Press.

Paraschivoiu, I. and Allet, A. (1988). Aerodynamic analysis of the darrieus wind turbines including dynamic-stall effects. *Journal of Propulsion and Power*, 4(5):472–477.

Paraschivoiu, I., Desy, P., and Masson, C. (1988). Blade tip, finite aspect ratio, and dynamic stall effects on the darrieus rotor. *Journal of propulsion and power*, 4(1):73–80.

Peng, H., Liu, H., and Yang, J. (2021). A review on the wake aerodynamics of h-rotor vertical axis wind turbines. *Energy*, 232:121003.

Pope, S. B. (2000). *Turbulent Flows*. Cambridge University Press.

Posa, A. (2020). Influence of tip speed ratio on wake features of a vertical axis wind turbine. *Journal of Wind Engineering and Industrial Aerodynamics*, 197:104076.

Proulx, G. and Paraschivoiu, I. (1989). *Méthode indicielle pour le calcul du décrochage dynamique*. École polytechnique de Montréal.

Puig, J. C. and Gamez, P. (2014). Openfoam guide for beginners. *Modelação computacional do escoamento em torno de um cilindro*.

Read, S. and Sharpe, D. J. (1980). An extended multiple streamtube theory for vertical axis wind turbines. In *Wind Energy Workshop*, pages 65–72.

Reynolds, O. (1895). Iv. on the dynamical theory of incompressible viscous fluids and the determination of the criterion. *Philosophical Transactions of the Royal Society of London. (A.)*, 186:123–164.

Rezaeiha, A., Montazeri, H., and Blocken, B. (2018). Characterization of aerodynamic performance of vertical axis wind turbines: impact of operational parameters. *Energy Conversion and Management*, 169:45–77.

Rezaeiha, A., Montazeri, H., and Blocken, B. (2019). On the accuracy of turbulence models for cfd simulations of vertical axis wind turbines. *Energy*, 180:838–857.

Roach, P. E. (1987). The generation of nearly isotropic turbulence by means of grids. *International Journal of Heat and Fluid Flow*, 8(2):82–92.

Rolin, V. F.-C. and Porté-Agel, F. (2018). Experimental investigation of vertical-axis wind-turbine wakes in boundary layer flow. *Renewable Energy*, 118:1–13.

Sanderse, B., van der Pijl, S., and Koren, B. (2011). Review of computational fluid dynamics for wind turbine wake aerodynamics. *Wind Energy*, 14(7):799–819.

Sangwan, J., Sengupta, T. K., and Suchandra, P. (2017). Investigation of compressibility effects on dynamic stall of pitching airfoil. *Physics of Fluids*, 29(7):076104.

Scheurich, F., Fletcher, T., and Brown, R. (2012). *The Influence of Blade Curvature and Helical Blade Twist on the Performance of a Vertical-Axis Wind Turbine*.

Scheurich, F., Fletcher, T. M., and Brown, R. E. (2011). Simulating the aerodynamic performance and wake dynamics of a vertical-axis wind turbine. *Wind Energy*, 14(2):159–177.

Schmitt, F. G. (2007). About boussinesq's turbulent viscosity hypothesis: historical remarks and a direct evaluation of its validity. *Comptes Rendus Mécanique*, 335(9):617–627. Joseph Boussinesq, a Scientist of bygone days and present times.

Shamsoddin, S. and Porté-Agel, F. (2014). Large eddy simulation of vertical axis wind turbine wakes. *Energies*, 7(2):890–912.

Sheldahl, R. E. and Klimas, P. C. (1981). Aerodynamic characteristics of seven symmetrical airfoil sections through 180-degree angle of attack for use in aerodynamic analysis of vertical axis wind turbines. Technical report, Sandia National Labs., Albuquerque, NM (USA).

Sheng, W., Galbraith, R., and Coton, F. (2008). A modified dynamic stall model for low mach numbers. *Journal of Solar Energy Engineering*, 130(3).

Shih, T.-H., Liou, W. W., Shabbir, A., Yang, Z., and Zhu, J. (1995). A new $k - \epsilon$ eddy viscosity model for high reynolds number turbulent flows. *Computers & Fluids*, 24(3):227–238.

Simao Ferreira, C., Van Bussel, G., Van Kuik, G., and Scarano, F. (2007). 2d piv visualization of dynamic stall on a vertical axis wind turbine. In *45th AIAA Aerospace Sciences Meeting and Exhibit*, page 1366.

Smagorinsky, J. (1963). General circulation experiments with the primitive equations: I. the basic experiment. *Monthly Weather Review*, 91(3):99 – 164.

Sørensen, J. and Shen, W. (2002). Numerical modeling of wind turbine wakes. *Journal of Fluids Engineering-transactions of The Asme*, 124:393–399.

Sørensen, J. N., Mikkelsen, R. F., Henningson, D. S., Ivanell, S., Sarmast, S., and Andersen, S. J. (2015). Simulation of wind turbine wakes using the actuator line technique. *Philosophical Transactions of the Royal Society A: Mathematical, Physical and Engineering Sciences*, 373(2035):20140071.

Spalart, P. and Allmaras, S. (1992). *A one-equation turbulence model for aerodynamic flows*.

Strickland, J. H. (1975). Darrieus turbine: A performance prediction model using multiple streamtubes. Technical Report SAND-75-0431.

Strickland, J. H., Webster, B. T., and Nguyen, T. (1979). A vortex model of the darrieus turbine: An analytical and experimental study. *Journal of Fluids Engineering*, pages 500–505.

Sutherland, H. J., Berg, D. E., and Ashwill, T. D. (2012). A retrospective of VAWT technology. *Sandia National Laboratories*, pages 1–64.

Sørensen, J. (2012). 2.08 - aerodynamic analysis of wind turbines. In Sayigh, A., editor, *Comprehensive Renewable Energy*, pages 225–241. Elsevier, Oxford.

Tavernier, D. D., Ferreira, C., Paulsen, U., and Madsen, H. (2020). The 3d effects of a vertical-axis wind turbine: rotor and wake induction. *Journal of Physics: Conference Series*, 1618:052040.

Templin, R. J. (1974). Aerodynamic performance theory for the nrc vertical-axis wind turbine. Technical Report N-76-16618; LTR-LA-160.

Tescione, G., Ragni, D., He, C., Simão Ferreira, C., and van Bussel, G. (2014). Near wake flow analysis of a vertical axis wind turbine by stereoscopic particle image velocimetry. *Renewable Energy*, 70:47–61. Special issue on aerodynamics of offshore wind energy systems and wakes.

Thönnißen, F., Marnett, M., Roidl, B., and Schröder, W. (2016). A numerical analysis to evaluate Betz's Law for vertical axis wind turbines. *Journal of Physics: Conference Series*, 753.

van Kuik, G. A. (2007). The Lanchester – Betz – Joukowsky limit. *Wind Energy*, 10(3):289–291.

Vergaerde, A., De Troyer, T., Muggiasca, S., Bayati, I., Belloli, M., Kluczewska-Bordier, J., Parneix, N., Silvert, F., and Runacres, M. C. (2020a). Experimental characterisation of the wake behind paired vertical-axis wind turbines. *Journal of Wind Engineering and Industrial Aerodynamics*, 206:104353.

Vergaerde, A., De Troyer, T., Muggiasca, S., Bayati, I., Belloli, M., and Runacres, M. C. (2020b). Influence of the direction of rotation on the wake characteristics of closely spaced counter-rotating vertical-axis wind turbines. In *Journal of Physics: Conference Series*, volume 1618, page 062017. IOP Publishing.

Wang, S., Zhou, Y., Alam, M. M., and Yang, H. (2014). Turbulent intensity and reynolds number effects on an airfoil at low reynolds numbers. *Physics of Fluids*, 26(11):115107.

Wernert, P., Geissler, W., Raffel, M., and Kompenhans, J. (1996). Experimental and numerical investigations of dynamic stall on a pitching airfoil. *AIAA journal*, 34(5):982–989.

Wilcox, D. (2006). *Turbulence Modeling for CFD (Third Edition) (Hardcover)*.

Wilson, R. E. and Lissaman, P. B. S. (1974). Applied aerodynamics of wind power machines. Technical Report PB-238595.

Yakhot, V. and Orszag, S. A. (1986). Renormalization-group analysis of turbulence. *Journal of Scientific Computing*, 57(14):1722–1724.

Yuan, Z., Sheng, Q., Sun, K., Zang, J., Zhang, X., Jing, F., and Ji, R. (2021). The array optimization of vertical axis wind turbine based on a new asymmetric wake model. *Journal of Marine Science and Engineering*, 9(8):820.

Zou, L., Wang, K., Jiang, Y., Wang, A., and Sun, T. (2020). Wind tunnel test on the effect of solidity on near wake instability of vertical-axis wind turbine. *Journal of Marine Science and Engineering*, 8(5).

COLOPHON

This document was typeset using LaTeX. The document layout was generated using the `arsclassica` package by Lorenzo Pantieri, which is an adaption of the original `classicthesis` package from André Miede.